TRANSMISSION OF INFRARED BEAMS THROUGH THE TURBULENT ATMOSPHERE

Dimitri Petrov

A Thesis in the Faculty of Engineering

Presented in partial fulfillment of the requirements for the degree of Master of Engineering at Concordia University, Montreal, Quebec, Canada.

January 1979

ABSTRACT

TRANSMISSION OF INFRARED BEAMS THROUGH THE TURBULENT ATMOSPHERE

Dimitri Petrov

The theory of infrared propagation through the atmosphere is reviewed and applied to the design of two opto-electronic communication links. One of these consists of a gallium-arsenide laser transmitter with a narrow divergence angle in the horizontal plane while the other employs an omnidirectional xenon arc transmitter. Both transmitters have a vertical divergence of 300 mrad. In both communication links a receiver equipped with a spherical lens and a silicon photodiode is used. Emphasis is placed on the study of air refractive index variations due to temperature gradients which cause a random amplitude modulation or "scintillation" in the receiver output signal. Experimental results are used to show that scintillation is not only a function of temperature, as hitherto assumed, but also a function of solar irradiance. Scintillation is quantitatively described by the modulation index which is found to be an increasing function of solar irradiance. It is also established that the transmission error rate of the laser and xenon channels is an increasing function of the modulation index. Based on experimental results obtained during field trials the maximum distance for error-free data transmission is calculated.

ACKNOWLEDGEMENTS

I wish to thank:

Professor Otto Schwelb for his guidance and advice which helped greatly to clarify my ideas,

My colleague, Carl Cusson, for numerous fruitful discussions,

Mr. A. E. Maine, Director of Engineering, Aviation Electric Ltd. for his encouragement and support,

My wife, Jane, and my children Katya, Julia, Tanya and Christine for their patience.

TABLE OF CONTENTS

LIST OF ILLUSTRATIONS

LIST OF TABLES

GLOSSARY OF RADIOMETRIC QUANTITIES AND UNITS

Symbol	Quantity	Description	Commonly used unit(s)
P	Radiant power	Rate of transfer of radiant energy	watt (W)
E	Radiant emittance	Radiant power per unit area emitted from a surface	$W.m^{-2}$
H	Irradiance	Radiant power per unit area incident upon a surface	$W.m^{-2}$
I	Radiant intensity	Radiant power per unit solid angle from a source	$W.sr^{-1}$
N	Radiance	Radiant power per unit solid angle per unit area emitted from a source	$W.sr^{-1}\ m^{-2}$
H_λ	Spectral irradiance	Irradiance per unit wavelength interval	$W.m^{-2}\ \mu m^{-1}$
N_λ	Spectral radiance	Radiance per unit wavelength interval	$W.sr^{-1}\ m^{-2}\ \mu m^{-1}$
ρ	Radiant reflectance	Ratio of reflected radiant power to incident radiant power	
λ	Wavelength		μm, nm

LIST OF SYMBOLS

Fundamental Constants

ε_o	$8.8548782 \times 10^{-12}$	$F.m^{-1}$	permittivity of free space
μ_o	$4\pi \times 10^{-7}$	$H.m^{-1}$	permeability of free space
c	2.99792458×10^{8}	$m.s^{-1}$	velocity of light in free space
k	1.380622×10^{-23}	$J.K^{-1}$	Boltzmann's Constant
h	6.626176×10^{-34}	J.s	Planck's constant
e	$1.6021892 \times 10^{-19}$ C		electron charge
m	9.109534×10^{-31} kg		electron mass
R_o	8.31441×10^{3}	$J.kmole^{-1}.K^{-1}$	gas constant

Abbreviations of Units

A	ampere	Hz	hertz
C	coulomb	J	joule
cm	centimetre	K	kelvin
dB	decibel	kg	kilogram
F	farad	km	kilometre
g	gram	m	metre
H	henry	mb	millibar

Abbreviations of Units (cont'd)

mm	millimetre	Ω	ohm
mrad	milliradian	rad	radian
μm	micrometre	s	second
N	newton	sr	steradian
nm	nanometre	V	volt
Np	neper	W	watt

Latin Letter Symbols

A_g	area of ground within the receiver field of view
A_L	cross-sectional area of laser beam
A_R	area of receiver lens
b	width of photodiode active area
c	velocity of light
C_d	junction capacitance of silicon photodiode
C_n	structure coefficient of refractive index
c_p	specific heat of air at constant pressure
C_T	structure coefficient of ambient temperature
d	diameter of infrared beam
D	diameter of receiver lens

Latin Letter Symbols (cont'd)

$D(\tau)$	structure of function corresponding to a time delay τ
$\vec{D}(t)$	electric displacement
e	electron charge
E_i	atomic energy level
E_g	ground emittance
$\vec{E}(t)$	electric field
h	height of receiver above ground
H_g	irradiance at the receiver lens due to the ground radiance
H_L	irradiance within the laser beam
H_s	spectral irradiance on the ground due to solar radiation
H_X	irradiance within the xenon beam
$\overline{i_s^2}$	mean square value of shot noise current
$\overline{i_j^2}$	mean square value of Johnson noise current
$k=2\pi/\lambda$	wave number
k_a	atmospheric absorption coefficient
k_M	Mie scattering coefficient

Latin Letter Symbols (cont'd)

k_R	Rayleigh scattering coefficient
ℓ	dimension of an eddy
ℓ_o	minimum dimension of an eddy
L_o	maximum dimension of an eddy
m	electron mass
M	molecular mass of a gas
n	refractive index
N_e	electron density
$N_1 = (n-1)10^6$	refractivity
N_{bg}	background radiance
p	pressure
p[y(t)]	probability density function of random variable y(t)
P	radiant power
P*[α]	cumulative distribution function with probability upper limit α<1
$\vec{p}(t)$	electron dipole moment
$\vec{P}(t)$	electric polarization
P_g	radiant power due to ground irradiance focussed on the photodetector

Latin Letter Symbols (cont'd)

P_{sky}	radiant power due to sky radiance focussed on the photodetector
R	Reynolds number
R_{cr}	critical Reynolds number
R_o	gas constant
R_L	load resistor on laser channel
R_X	load resistor on xenon channel
s^2	variance
(S/N)	signal to noise ratio
t	time
T	absolute temperature
t_L	transmittance of atmosphere to laser radiation
t_X	transmittance of atmosphere to xenon radiation
v	velocity
V	volume
x	distance between transmitter and receiver
y(t)	continuous random variable
$\overline{y^2(t)}$	mean square value of y(t)
h	height of thin-wire temperature probe above the ground.

Greek Letter Symbols

α	horizontal acceptance angle of infrared receiver
β	vertical acceptance angle of infrared receiver
β_r	responsivity of photodetector
γ	radiative damping coefficient
δ	normalized frequency detuning
ε_o	permittivity of free space
ε_r	relative permittivity
ζ	horizontal divergence angle of laser transmitter
η	vertical divergence angle of laser transmitter
θ	incidence angle
$\kappa = 2\pi/\ell$	spatial frequency where ℓ is the dimension of an eddy
λ	wavelength
μ_o	permeability of free space
μ_r	relative permeability
ν	kinematic viscosity
ρ_n	depolarization factor
ρ	radiant reflectance
σ	normalized variance of irradiance or modulation index

Greek Letter Symbols

σ_T	variance of the logarithm of irradiance
τ	time delay
$\Phi(\omega)$	power density spectrum
$\phi(\tau)$	autocorrelation function
χ	electric susceptibility
Ω_R	solid acceptance angle of receiver
ω	angular frequency

CHAPTER I

INTRODUCTION

Opto-electronic communication links have become increasingly important in data transmission over the past few years, especially where high isolation between channels in close proximity is required. A typical application where the advantage of this characteristic becomes apparent is the transmission of meteorological data at airports. At most large airports there are three meteorological stations which transmit to the control tower information regarding wind speed and direction, atmospheric temperature and pressure, and visibility. This information is transmitted over buried cables. It was found recently that in order to detect localized wind shears which present a serious danger to landing aircraft the number of locations at airports where pressure is monitored must be increased substantially. The transmission of this additional information to the control tower requires either a costly installation of new buried cables or the provision of additional radio communication links in the already crowded frequency spectrum prevalent at airports. Opto-electronic communication channels offer an economical alternative to these traditional methods of data transmission.

The aim of this dissertion is to investigate both analytically as well as experimentally the transmission properties of opto-electronic communication links which utilize a common receiver equipped with a spherical lens and a silicon photodiode, and either a gallium-arsenide laser transmitter with a horizontal divergence of 0.4 mrad and a

vertical divergence of 300 mrad, or a xenon arc transmitter which is omnidirectional in the horizontal phane and also has a 300 mrad vertical divergence.

The reason for adopting this beam geometry was dictated by the operational requirements of the opto-electronic communication systems. When collimated beams are used for data tranmission, the transmitter and the receiver require time consuming adjustments in the horizontal and vertical planes. However, if the transmitted beam diverges in the vertical plane and the receiver has a wide vertical acceptance angle, the transmitter and the receiver can be aligned by rotation in the horizontal plane, only. This configuration is therefore particularly suitable in mobile systems.

Chapter II describes the basic theory of infrared radiation propagation through the atmosphere. It is shown that the attenuation of signal amplitude due to molecular absorption and scattering by molecules as well as aerosol particles is a deterministic function of distance. Scattering caused by air turbulence, on the other hand, produces a random path attenuation resulting in scintillation. The latter is treated quantitatively by statistical methods and can be defined by the modulation index parameter. In the literature scintillation is shown to be a function of distance, radiation wavelength and ambient temperature. However, experimental results indicate that scintillation is also a function of solar irradiance. Furthermore, it has been found that although random signal amplitude modulation can be caused by random variations of beam direction and by high levels of ambient radiance, the effect of both phenomena on the opto-electronic systems used in the experimental investigation is negligible.

Chapter III deals with the opto-electronic design of the two communication links. Methods of concentrating the radiant power of the gallium arsenide laser and the xenon arc within specified horizontal and vertical divergence angles are described. Expressions are derived which define the laser and xenon radiant power density as a function of distance. The receiver output signals and signal-to-noise ratios are calculated from the receiver lens area and the infrared detector responsivity, for an assumed maximum range of 500 m.

Chapter IV contains a summary of experimental results which have been obtained in two stages. During Stage 1, the 500 m maximum operating distance has been simulated over 50 m by means of calibrated attenuation filters. Receiver output signals on the laser and xenon communication channels have been recorded and found in close agreement with theoretical results calculated in Chapter III, which take into account the deterministic attenuation due to molecular absorption as well as scattering caused by molecules and aerosol particles. In Stage 2, the transmitters and the receiver have been positioned 500 m apart over a grassy terrain and the random amplitude modulation caused by air turbulence has been observed on both communication channels under different meteorological conditions. Sudden changes of the average scintillation level have been discovered under conditions of variable cloudiness. Recorded data have been used to compute the modulation index before and after the emergence of the sun from a cloud. Based on these results the dependence of scintillation on solar irradiance in addition to the conventional dependence on air turbulence caused by temperature gradients has been established. The study of infrared beam propagation through the turbulent atmosphere suggests that the background

radiance, i.e. sun light scattered by molecules and aerosol particles should also be subjected to amplitude variations. The design of a radiometer which has been used to investigate this hypothesis is described. Experimental results obtained with this instrument proves the existence of a high-frequency (up to 1 kHz) random variable component superimposed on a slowly varying component of background radiance.

Quantitative values of both components are determined taking into account the area of the radiometer lens and the responsivity of the infrared detector.

Chapter V interprets the experimental results. Based on recordings of the laser and xenon signals it is shown that the modulation index is an increasing function of solar irradiance. Transmission error is defined as failure to detect a transmitted pulse and it is shown that the error rate is an increasing function of modulation on both communication channels. In order to invesigate the relationship between scintillation and solar irradiance further laboratory and field experiments are proposed.

In concluding, criteria for the design of opto-electronic communication links which utilize coherent and incoherent beams are established and the maximum distance for reliable data transmission is determined. It is emphasized that although divergent beams offer operational advantages because they require only an alignment in the horizontal plane, collimated beams offer much higher transmission reliability at the expense of a complex alignment procedure in both the horizontal and vertical planes.

CHAPTER II

BASIC THEORY OF INFRARED RADIATION PROPAGATION THROUGH THE ATMOSPHERE

2.1 Introduction

The aim of this chapter is to study the influence of the atmosphere on the operation of an opto-electronic communication link in the infrared spectrum. The radiant flux emanating from the transmitter is partially absorbed and partially scattered by molecules as well as aerosol particles and this leads to a decrease in power density which is a deterministic function of distance and is independent of time. The radiant flux is also scattered by turbulences which cause random refractive index fluctuations along the propagation path and induce variations in power density, in phase as well as in the direction of the transmitted beam. The random fluctuations of the beam are observed as noise in the receiver and the relative importance of this interference depends to a large extent on the receiver design. Furthermore, it was discovered during field tests of opto-electronic communication links described in Chapter IV that the amplitude of the received signal also depends on solar radiance. The effects of these phenomena are reviewed in the light of the existing theory of infrared transmission through the atmosphere. The results of this study are then applied to the design of two opto-electronic communication links

illustrated in Figure 2.1, one using a narrow beam gallium-arsenide laser transmitter and the other an omnidirectional xenon arc transmitter.

2.2 Absorption and Particle Scattering

a) Absorption

The absorption of infrared radiation by air is an atomic or molecular resonance phenomenon. The frequency ω_i of the monchromatic absorption line is given by

$$\omega_i = (E_i - E_j)/\hbar \qquad (2.1)$$

where $\hbar = 1.50545 \times 10^{-34}$ joule.s is Planck's constant divided by 2π, and E_i, E_j are two discrete energy levels of the molecule. The absorption of electromagnetic energy by a molecule causes electron transitions from level E_i to level E_j. The dynamics of a gas molecule subjected to a sinusoidally varying electric field can be described by the second order differential equation of a damped mechanical oscillator. Its solution in phasor form, assuming x polarization of the applied field and using the convention $\vec{A}(t) = \mathrm{Re}[\tilde{A}(\omega)\exp(j\omega t)]$ for all time dependent variables is according to Siegman [1]:

$$\tilde{X}(\omega) = j(e/m)\tilde{E}_x/[\gamma\omega + j(\omega^2 - \omega_a^2)] \qquad (2.2)$$

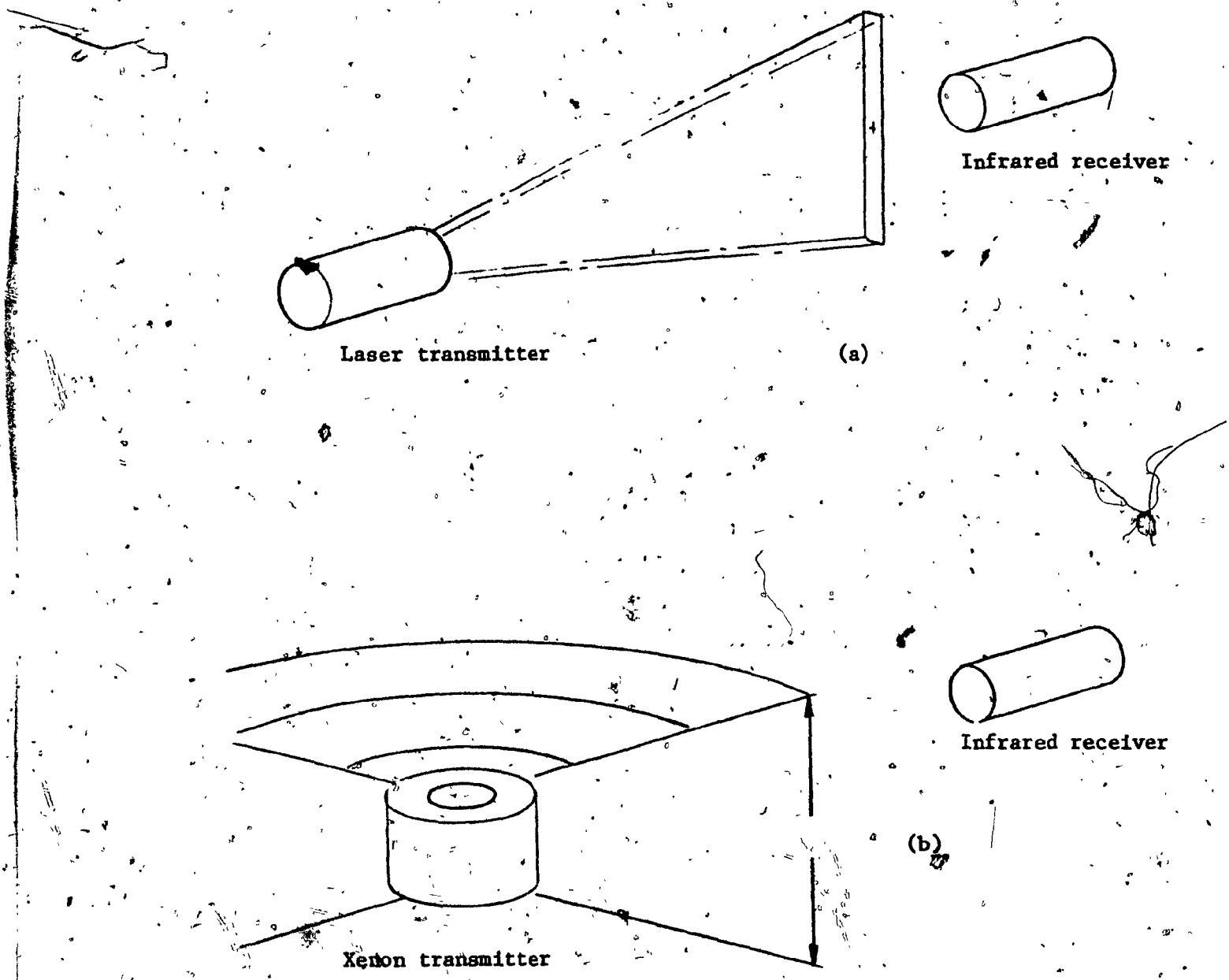

Figure 2.1 Diagram of opto-electronic communication links

where $\tilde{X}(\omega)$ is the displacement of the electron with respect to the nucleus

e is the absolute value of the electronic charge

m is the electron mass

ω is the frequency of the electric field

ω_a is the atomic resonance frequency

γ is the damping coefficient

$\tilde{E}_x$ is the x component of the applied electric field

For values of ω in the vicinity of ω_a

$$\omega^2-\omega_a^2 \simeq 2\omega_a(\omega-\omega_a) \tag{2.3}$$

as a result

$$\tilde{X}(\omega) \simeq j(e/m\gamma\omega_a)\tilde{E}_x/[1+2j(\omega-\omega_a)/\gamma]. \tag{2.4}$$

When the negatively charged electron is displaced by a distance $x(t)$ with respect to the positively charged nucleus the oscillator becomes a dipole whose moment is

$$\vec{p}(t) = -e\vec{x}(t) \tag{2.5}$$

In eletromagnetic theory the electric field $\vec{E}(t)$ and the electric displacement $\vec{D}(t)$ at any point in space are related by

$$\vec{D}(t) = \varepsilon_0\vec{E}(t) + \vec{P}(t) = \varepsilon\vec{E}(t) \tag{2.6}$$

where $\vec{P}(t)$ is the electric polarization at that point. This quantity is the electric dipole moment per unit volume and can be expressed as the sum of atomic or molecular dipoles

$$\vec{P}(t) = N_e\vec{p}(t) \tag{2.7}$$

where N_e is the electron density. Equations (2.5), (2.6) and (2.7)

establish a relationship between the macroscopic polarization $\vec{P}(t)$ and the molecular displacement vector $\vec{x}(t)$. Since $\tilde{P}(\omega) = \chi(\omega)\varepsilon_o\tilde{E}$ where $\chi(\omega)$ is the electric susceptibility, a generally complex quantity:

$$\chi(\omega) = \chi'(\omega) - j\chi''(\omega) \qquad (2.8)$$

the real and imaginary parts of the displacement phasor $\tilde{X}(\omega)$ give rise to real and imaginary electrical susceptibility. Poynting's theorem shows that the real part of the susceptibility describes the the phase shift due to the medium, whereas its imaginary part is directly proportional to the attenuation caused by absorption. The amplitude response as a function of frequency of the forced sinusoidal motion is described by the factor

$$1/[1+j2(\omega-\omega_a)/\gamma] = 1/(1+j\delta) \qquad (2.9)$$

where δ is the normalized frequency detuning, whereas the power response is described by the squared magnitude of (2.9)

$$1/\{1+[2(\omega-\omega_a)/\gamma]^2\} = 1/(1+\delta^2) \qquad (2.10)$$

This expression is the well known lorentzian lineshape. The bandwidth $\Delta\omega_a$ of the oscillator model is obtained by setting $\delta=1$ in (2.9) which yields $\omega-\omega_a = \pm\gamma/2$ and therefore $\Delta\omega_a = \gamma$. The oscillating electron radiates electromagnetic energy at a rate characterized by the radiative lifetime $\tau_r = 1/\gamma$; this energy conversion mechanism causes a damping of the particle motion. The radiative lifetime in the optical frequency range ($\sim 10^{14}$Hz) is of the order of 10^{-8}s [1], the corresponding half-power bandwidth $\Delta f_a = \Delta\omega_a/2\pi$ is of the order of 10MHz. The same considerations apply to an aggregate of molecules providing the proper damping coefficient, which takes into account the effects of collision broadening and doppler broadening, is used in (2.10).

In an aggregate of atoms random collisions occur. A collision disturbs the continuity of the sinusoidal electron motion and changes the amplitude and phase of the displacement phasor. The cumulative effect of these disturbances is a widening of the bandwidth as described by the expression

$$\Delta\omega_a = \gamma + 2/T \tag{2.11}$$

where γ and is the radiative damping coefficient, T is the average time between collisions and 2/T is the collision broadening of the lorentzian lineshape.

Doppler broadening is associated with the brownian motion of gas atoms. Doppler shifts in resonant frequencies occur whenever radiating atoms move with respect to the coordinate system of the travelling electromagnetic wave. Since this motion is random, the changes in the absorption line are also random and the overall frequency response of the collection of atoms is broadened. The doppler-broadened bandwidth is described [1] by the expression

$$\Delta\omega_d = 2\pi\left[8(\ln 2)kT/M\lambda_a^2\right]^{1/2} \tag{2.12}$$

where k is Boltzmann's constant, T is the absolute gas temperature, M is the molecular mass of the gas and λ_a is the resonant wavelength. According to Zuyev [2] radiative damping and doppler broadening is negligible in atmospheric gases at low altitudes so that the bandwidth of the lorentzian lineshape depends mainly on collision broadening and is close to 2/T. In order to evaluate the decrease in the irradiance (radiant power density) H due to transmission loss all the absorption lines have to be taken into account. Their cumulative effect is defined by the atmospheric absorption coefficient and the resulting attenuation of irradiance is described by the Bouguer-Lambert law. It states that radiant power density decreases at a rate proportional to

the thickness of the medium dx

$$dH/H = -k_a\, dx. \tag{2.13}$$

By integration

$$H = H_o \exp(-k_a x) \tag{2.14}$$

where k_a, the atmospheric absorption coefficient, is based on attenuation measurements in the laboratory and H_o is the irradiance at $x = 0$.

As a numerical example this law will be applied to determine the irradiance attenuation in two opto-electronic communication links. The laser transmitter operates at 904 nm and the xenon transmitter emits radiation between 900 nm and 1100 nm (see Section 3.1) both signals are attenuated by the H_2O absorption line. The approximate value of k_a [8, page 252] is 0.33 Np/km^{-1} thus for $x = 0.5$ km, the maximum anticipated operating distance of both opto-electronic communication links, the transmittance H/H_o calculated from (2.10) is 0.84, i.e. the attenuation is 0.71 dB.

b) Particle Scattering

An optical beam is scattered when its direction of propagation changes as a result of an interaction with an atom, a molecule or an aerosol particle, as shown in Figure 2.2. Since the scattered beam has a larger cross-sectional area than the incident beam, this phenomenon causes a decrease in irradiance. Rayleigh scattering occurs when the wavelength of the incident radiation is much larger than the particle diameter, while Mie scattering takes place when the wavelength of the incident radiation is of the same order as the particle diameter. Both phenomena are discussed.

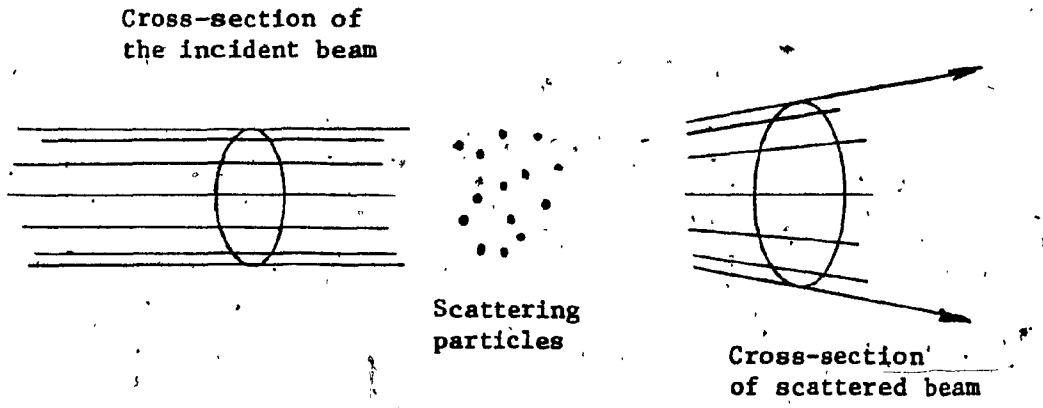

Figure 2.2 Scattering of an optical beam by particles.

Rayleigh scattering occurs at the atomic and molecular scale. Its description is therefore in the domain of physical optics and its characteristics can be derived from the mass-spring model of an electronic oscillator. The dynamics of a gas atom subjected to a harmonic field is described by (2.2). In the frequency range outside the lorentzian bandwidth the dipole consisting of an electron and a molecule oscillates at the frequency of the incident electric field. The moving electron radiates an electric field which is uniformly distributed over a toroidal volume as shown in Figure 2.3 reproduced from [3]. The irradiance emitted by the dipole derived by Hecht and Zajac [3] is

$$H = \pi^2 p^2 c \sin^2\theta / 2\varepsilon_o \lambda^4 x^2 \qquad (2.15)$$

where p is the dipole moment, θ is the scattering angle, λ is the wavelength of the incident radiation and x is the distance from the center of the dipole. From this description it becomes apparent that the oscillating dipole absorbs power from a collimated beam and reradiates it over a larger area. Rayleigh [4] showed that scattering by molecules can be described by the volume scattering coefficient k_R given by the expression

$$k_R = 32\pi^3 (n-1)^2 (6+3\rho_n)/3\lambda^4 N(6-7\rho_n) \qquad (2.16)$$

where ρ_n is the depolarization factor, n is the air refractive index at normal temperature and pressure and N is the molecular density. The attenuation of irradiance as a function of distance caused by Rayleigh scattering is described by an expression similar to (2.14)

$$H = H_o \exp(-k_R x) \qquad (2.17)$$

Penndorf [5] computed k_R as a function of λ and used $N = 2.54743 \times 10^{19}$ cm^{-3} at normal temperature and pressure, and $\rho_n = 0.035$. The value of

Figure 2.3 Toroidal radiation pattern of a vibrating dipole [3, page 49].

k_R at 904 nm is 1.67×10^{-3} Np/km. As a numerical example the attenuation was determined from (2.17) for a distance of 500 m and found to be 0.004 dB.

Mie scattering occurs when infrared radiation interacts with aerosol particles such as water vapour, smoke, dust or water droplets in fog and clouds. Particles which attenuate infrared radiation have diameters larger than the propagated wavelength, hence this type of scattering can be described by methods of geometrical optics. Attenuation due to scattering by dielectric particles was treated by Mie [6] by applying Maxwell's equations to a monochromatic plane wave incident on a homogeneous, isotropic sphere. He evaluated the scattered irradiance as function of the scattering angle at distances large compared to the particle radius. Mie found that when an electromagnetic wave propagates through a medium characterized by an aerosol particle density N, the irradiance decreases by

$$dH = -H\pi r^2 KNdx \tag{2.18}$$

while traversing a distance dx. In this expression πr^2 is the particle cross-sectional area and K is a dimensionless quantity defined as the ratio of total radiant flux scattered by one particle in all directions to the flux incident on the cross-sectional area of the spherical particle. By integrating (2.18) an expression similar to (2.14) is obtained

$$H = H_o \exp(-k_M x) \tag{2.19}$$

where k_M is the Mie scattering coefficient given by

$$k_M = \pi r^2 KN. \tag{2.20}$$

Based on Mie's theoretical work [6] Penndorf [7] computed and tabulated K as a function of the normalized parameter $2\pi r/\lambda$, the bulk refractive

index n of the scatterer material and the amplitude of the incident electric field. However, it is difficult to apply these results in the evaluation of irradiance because they do not take into account the occurrence of multiple scattering. Furthermore, it is difficult to establish a practical value of N since the number of aerosol particles per unit volume may vary several orders of magnitude. For this reason measured rather than calculated results of k_M are used to determine the attenuation due to scattering. These measured results include the effect of molecular absorption, however if the latter is known, the effect of scattering can be isolated. By using this method a typical value of k_M [8, page 210] is 0.037 Np/km; it was measured at ground level over a distance of 1.2 km. As a numerical example the attenuation due to Mie scattering was determined from (2.19) and found to be 0.079 dB.

In summary, infrared radiation propagating through the atmosphere is attenuated by absorption as well as by Rayleigh and Mie scattering. The irradiance is an exponentially decreasing function of distance and the effect of all three types of attenuation can be expressed in one equation by combining (2.14), (2.17) and (2.19).

$$H = H_o \exp[-(k_a+k_s)x] \qquad (2.21)$$

where $k_s = k_R+k_M$ takes into account Rayleigh and Mie scattering. The total attenuation due to absorption and scattering for an anticipated operating distance of 500 m is 0.74 dB and the corresponding atmospheric transmittance H/H_o is 0.85.

2.3 Background Radiance and "Spot Dancing"

The attenuation mechanisms studied so far depend uniquely on the medium. This section discusses background radiance and "spot dancing", phenomena which are observed as fluctuations of the received signal and depend both on the medium and the receiver characteristics.

2.3.1 a) Background Radiance

The receiver in an opto-electronic link consists of a lens or a mirror which focusses the beam carrying the signal onto a detector. However, the receiver also detects the solar radiance scattered by air molecules, aerosol particles and the ground into the acceptance angle of the receiver. Both sources of energy constitute what is known as background radiance which varies slowly in time compared to the signal modulated irradiance. The amount of background radiance focussed onto the photodetector depends on the area of the receiver lens, the solid angle subtended by the photodetector (see Figure 2.4) and the zenith angle of the receiver. If the total radiant power due to the background radiance concentrated on the photodiode is large, it can drive the photodetector into saturation. The mechanism of this saturation is best understood by referring to Figure 2.5 which shows a set of characteristic curves of the photodiode and the load line defined by resistor R. Figure 2.5a shows the pulse train of peak radiant power P_1, and the corresponding voltage $e_1(t)$ in the linear operating region of the photodiode. Figure 2.5b shows the same pulse train superimposed on constant radiant flux P_2. The photodiode in this case is saturated and the corresponding output voltage $e_2(t)$ is smaller than $e_1(t)$. An investigation will be undertaken in order to determine the level of

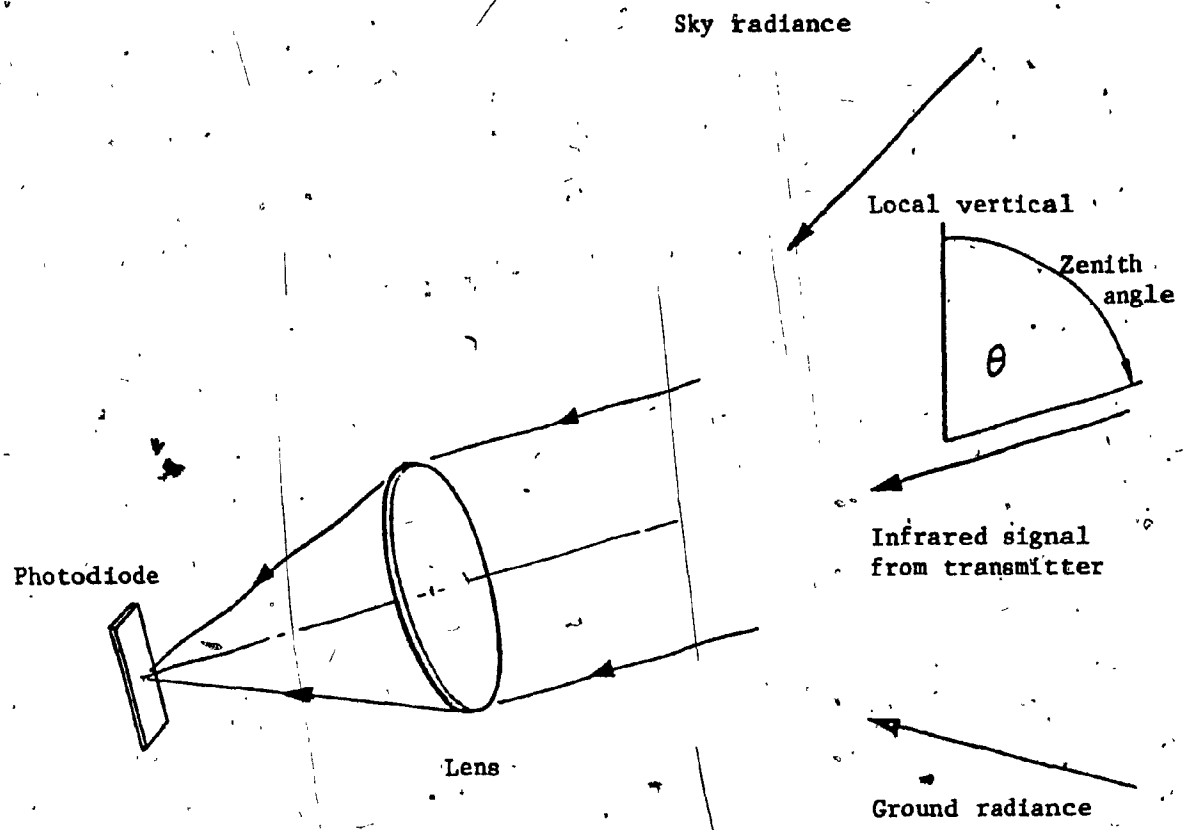

Figure 2.4 Schematic of infrared receiver

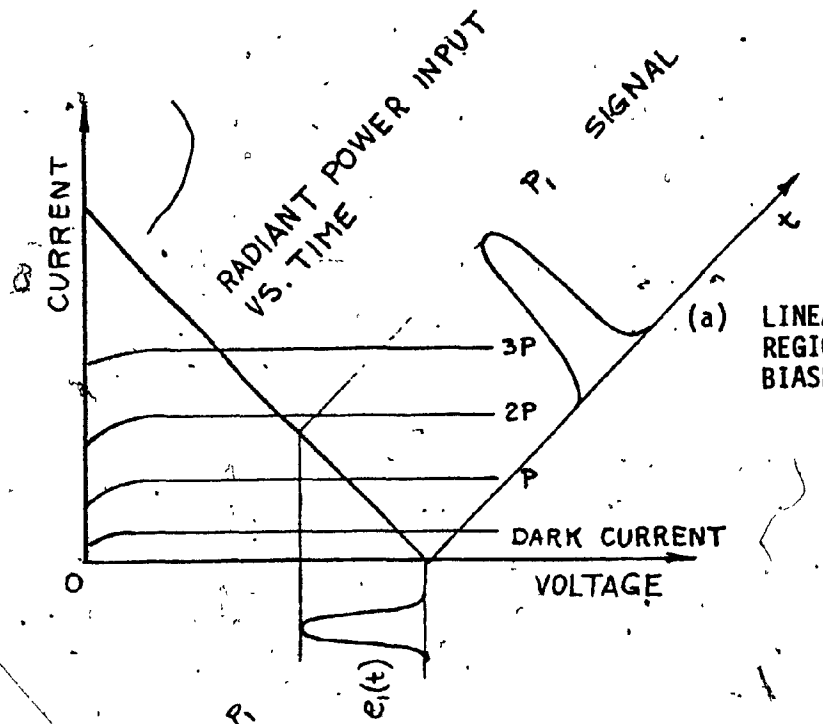

(a) LINEAR OPERATING REGION OF REVERSE BIASED PHOTODIODE

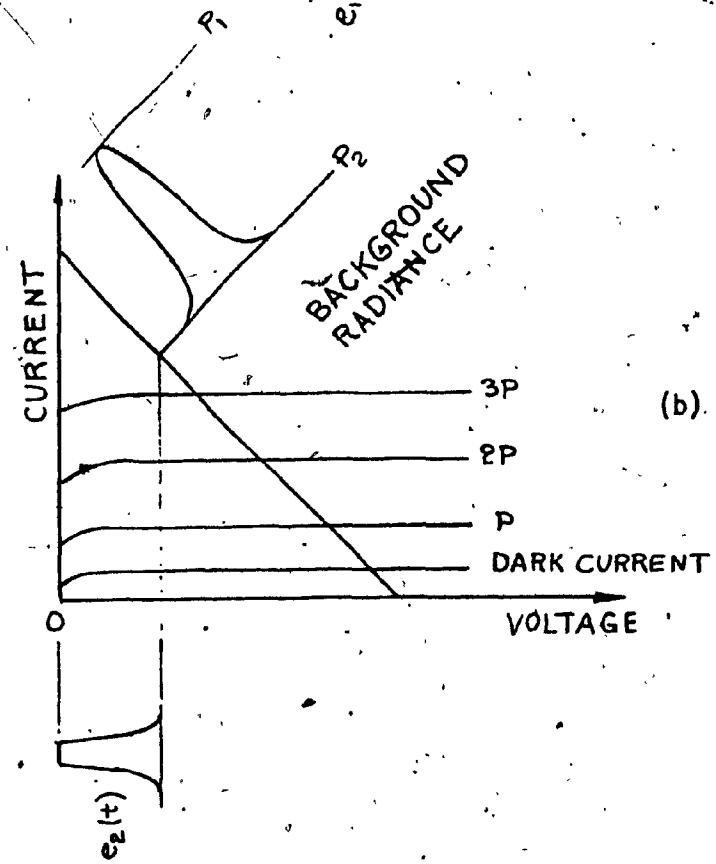

(b) NON-LINEAR OPERATING REGION OF REVERSE BIASED PHOTODIODE

Figure 2.5 Saturation of photodiode by background radiance

radiant power due to ambient radiance and establish whether or not it can cause an attenuation of the received signal.

b) Evaluation of Ground Radiance:

An opto-electronic receiver consisting of a silicon photodiode in the focal plane of a spherical lens is shown in Figure 2.6. It is installed at a height h above the ground, at a distance x_2 from the transmitter. In addition to the signal the receiver also detects radiant power emitted by a strip of ground irradiated by the sun. In the following an expression is obtained for the amount of detected ground radiance.

It is assumed that the radiant intensity from an elementary area $dA_g = wdx$ is defined by Lambert's law

$$I(\Theta) = I_o \cos \Theta \quad W/sr \qquad (2.22)$$

where I_o is the intensity normal to the surface and Θ is the angle between the normal to the surface $\vec{n}$ and the ray from the centre of dA_g. Such a surface is called perfectly diffusing. The total radiant flux emitted by dA_g (see Figure 2.7) into a hemisphere is $2\pi I_o \cos\Theta$. The irradiance H distributed over a hemisphere of radius r is obtained by dividing the total flux by the surface area of the hemisphere:

$$H = I_o \cos \Theta / r^2 \quad W/m^2 \qquad (2.23)$$

The radiant intensity distribution is symmetrical about the normal $\vec{n}$ to dA_g and the area of a spherical zone subtended by an angle $d\Theta$ is $2\pi r^2 \sin \Theta \, d\Theta$. Therefore the radiant power incident on this area is

$$H \, 2\pi r^2 \sin \Theta \, d\Theta = 2\pi I_o \cos\Theta \sin \Theta \, d\Theta. \qquad (2.24)$$

The total radiant power P_3 leaving dA_g is equal to the total radiant power passing through the hemisphere

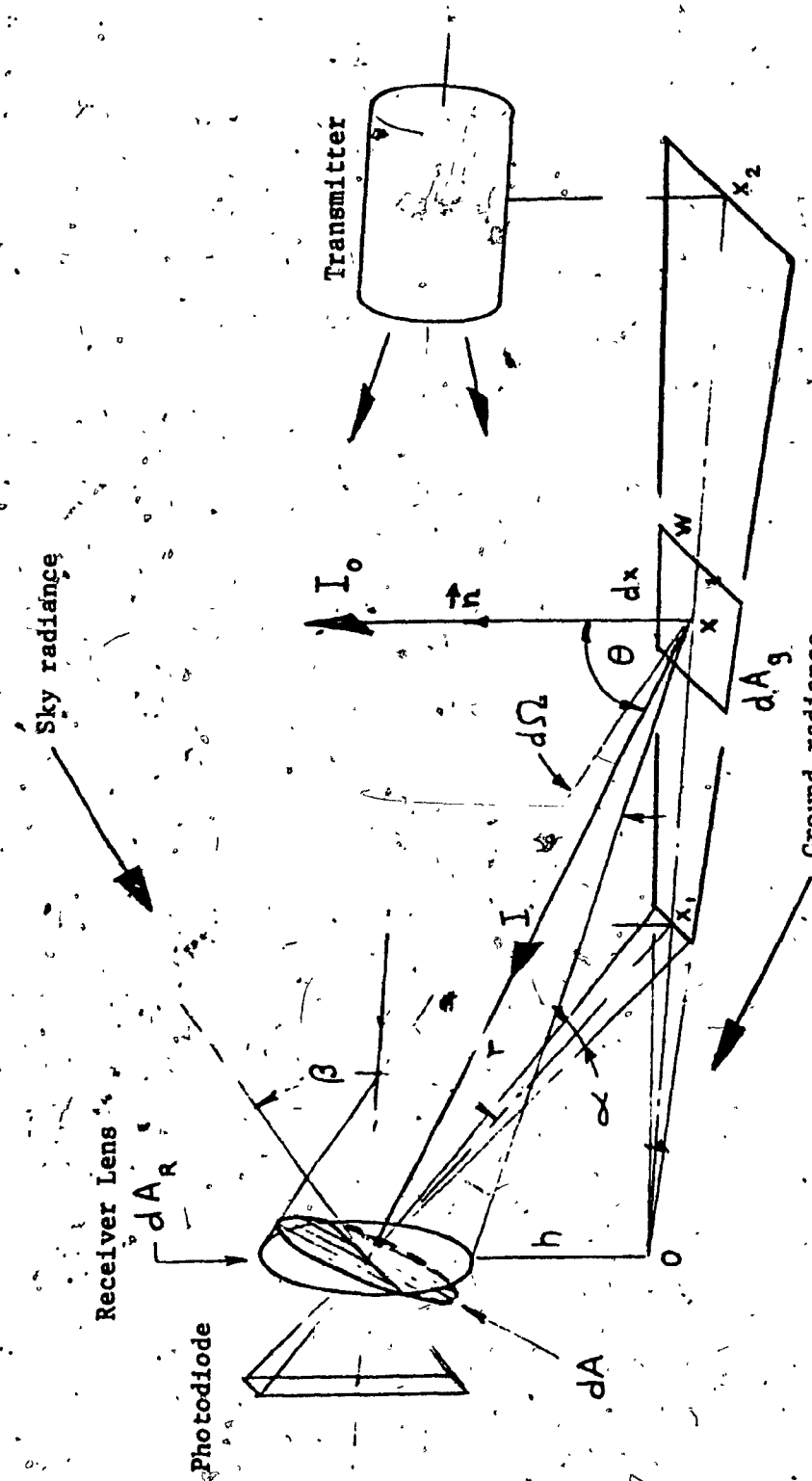

Figure 2.6 Definition of ground radiance

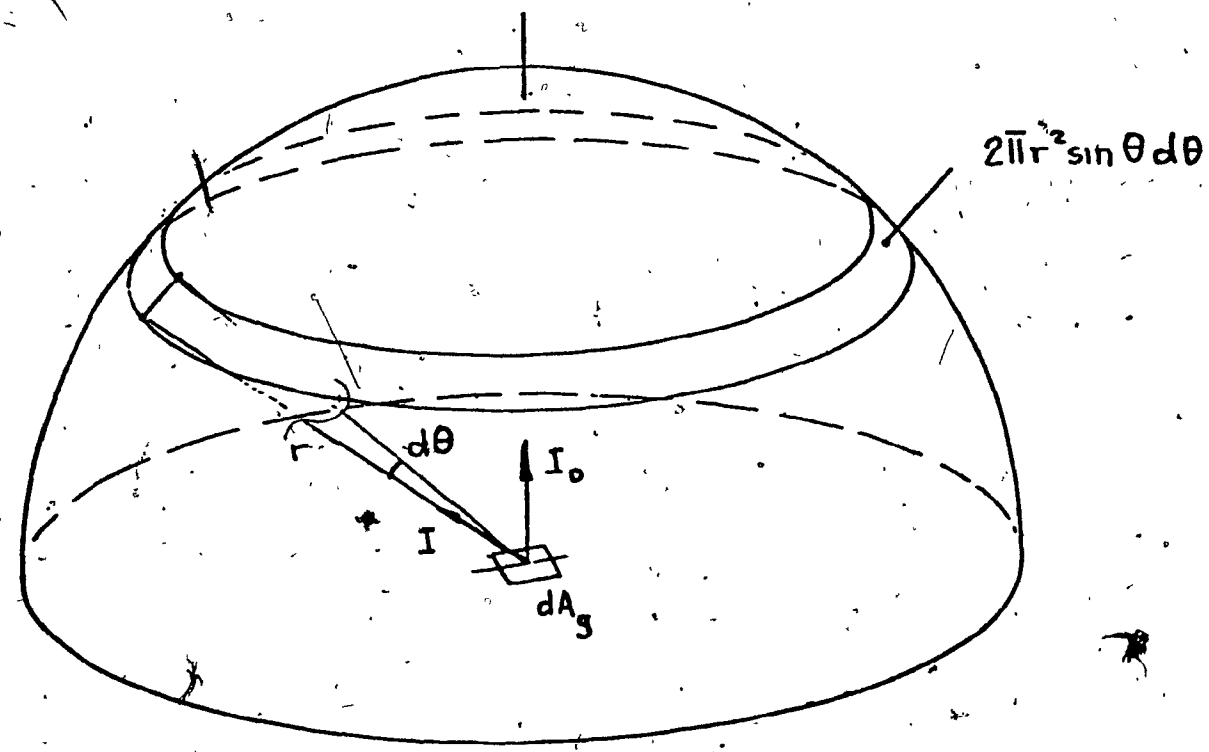

Figure 2.7 Hemispherical radiation from an elementary surface radiator.

$$P_3 = 2\pi I_o \int_o^{\pi/2} \cos\theta \sin\theta \, d\theta \qquad (2.25)$$

$$= \pi I_o \quad W$$

Equation (2.25) expresses the important result that radiant power emitted from a perfectly diffusing plane surface is π times the intensity normal to the surface. The radiant power output density from a surface is defined as its emittance E_g measured in W/m^2 hence (2.25) may be formulated in terms of this emittance as:

$$E_g A_g = \pi I_o \quad W \qquad (2.26)$$

The results derived above will now be used to determine at the receiver lens the irradiance H_g emanating from the ground strip extending between $x = x_1$ and $x = x_2$ as shown in Figure 2.6. To this end one computes first the incremental irradiance H_g due to A_g. Let dA be an elementary area perpendicular to the ray joining the centre of dA_g to the centre of the receiver lens. The incremental irradiance at dA is defined as:

$$H_g = dP/dA = Id\Omega/dA = I_o \cos\theta/r^2 \qquad (2.27)$$

where dP is the incremental radiant flux within the cone defined by the solid angle $d\Omega = dA/r^2$. Since the plane of the lens subtends an angle $\pi/2 - \theta$ with the ray, the irradiance in the plane of the lens is

$$H_g = I_o \cos\theta \sin\theta/r^2. \qquad (2.28)$$

Substituting I_o from (2.26) into this equation yields

$$H_g = E_g \cos\theta \sin\theta \, A_g/\pi r^2. \qquad (2.29)$$

Since $dA_g = w(x)dx$ the above equation becomes

$$dH_g = E_g \cos\theta \sin\theta \, w(x)dx/\pi r^2 \qquad (2.30)$$

In order to determine the total irradiance H_g at the receiver lens produced by the sun-irradiated ground shown in Figure 2.6 (2.30) is integrated between $x = x_1$ and $x = x_2$. Using relations $x = h \tan \theta$, $dx = h \sec^2 \theta \, d\theta$, $r = h \sec \theta$ and $w(x) = \alpha x$ where α is the horizontal acceptance angle of the receiver

$$H_g = \alpha E_g \int_{\theta_1}^{\theta_1} \sin^2 \theta \, d\theta \tag{2.31}$$

$$= \alpha E_g \left[\theta/2 - 1/4 (\sin 2\theta)\right]_{\theta_1}^{\theta_2} \tag{2.32}$$

The lower limit of θ corresponds to the location (see Figure 2.6) where the lower portion of the receiver vertical acceptance angle intersects the ground, consequently $\theta_1 = \pi/2 - \beta/2$, where β is the vertical acceptance angle of the receiver. The upper limit is $\theta_2 = \tan^{-1} x_2/h$, where x_2 is the distance between the transmitter and the receiver. Using data pertaining to a practical opto-electronic system: $h = 1.5$ m, $x_2 = 500$ m, $\alpha = 4$ mrad and $\beta = 300$ mrad the ground irradiance is found to be

$$H_g = 3 \times 10^{-4} E_g \ \text{W/m}^2 \tag{2.33}$$

The radiant emittance of the ground E_g can be determined provided the total irradiance and the reflectance of the ground are known. Thus

$$E_g = \rho_1 \, H_s(\lambda=0.9\mu\text{m}) \Delta\lambda \tag{2.34}$$

where ρ_1 is the reflectance of the ground, $H_s(\lambda=0.9\mu\text{m})$ the spectral irradiance at 900 nm, and $\Delta\lambda$ is the linewidth of the system. Using the numerical values $\rho_1 = 0.41$ [8], $H_s(\lambda=0.9\mu\text{m}) = 0.07$ W/m^2/nm and $\Delta\lambda = 100$ nm

$$E_g = 0.0287 \times 10^3 \ \text{W/m}^2 \tag{2.35}$$

is obtained. Substituting this value into (2.33) gives

$$H_g = 8.61 \text{ mW/m}^2 \qquad (2.36)$$

The total radiant power P_g due to the sun irradiance reflected from the ground can be estimated by multiplying the above value by the area of the receiver lens. Assuming a lens diameter of 3 cm $P_g = 6.1\mu W$.

c) Evaluation of Sky Radiance

The solar radiation dispersed by air and reflected from the clouds generates a radiant flux P_{sky} which is focussed on the photodetector:

$$P_{sky} = N_{sky}\, \Omega_R\, A_R\, \Delta\lambda \qquad (2.37)$$

where N_{sky} is the sky radiance and its typical value on a sunny day is $2.0 \times 10^4\ \mu W.cm^{-2}\ sr^{-1}\ \mu^{-1}$, Ω_R is the solid acceptance angle of the receiver, A_R is the receiver lens area and $\Delta\lambda$ is the optical linewidth of the receiver. Assuming the numerical values $\Omega_R = 1.2 \times 10^{-3}$ mrad, $A_R = 7.07\ cm^2$ and $\Delta\lambda = 100$ nm $= 0.1\mu$ one obtains from (2.37) $P_{sky} = 17.0\ \mu W$.

The sum of ground and sky radiance is equal to the total background radiant power P_{bg}. Using the above numerical values

$$P_{bg} = P_g + P_{sky} = 6.1 + 17.0 = 23.1\ \mu W \qquad (2.38)$$

This value is small compared to the typical radiant power input of 100 μW at which the photodiode starts to saturate. In the design of the opto-electronic transmission system described in Chapter III the influence of background radiance can therefore be neglected.

2.3.2 The "Spot Dancing" Phenomenon

When an electromagnetic wave is transmitted through the atmosphere its direction of propagation changes because of variations in the air refractive index. These variations are caused by density gradients and by turbulence as described below:

a) The air refractive index is a function of density and consequently a function of altitude. The higher the altitude, the lower the density and the lower the refractive index. An infrared beam transmitted at a zenith angle θ traverses layers of air with progressively lower refractive indices and is therefore deflected downward. This effect is illustrated in Figure 2.8a showing the receiver at an altitude h_1 above the transmitter. The irradiance detected by the receiver lens is concentrated within the focal spot on the photodiode. As the ambient temperature changes during the diurnal cycle, variations in the air refractive index occur. Consequently, the incident angle at the receiver lens changes causing a displacement of the focal spot in the vertical plane. The same phenomenon also occurs when the transmitter and the receiver are at the same level above the surface of the earth but separated by a large distance as shown in Figure 2.8b. In this case the infrared beam crosses spherical layers of the atmosphere whose refractive indices decrease with altitude and is also deflected downward.

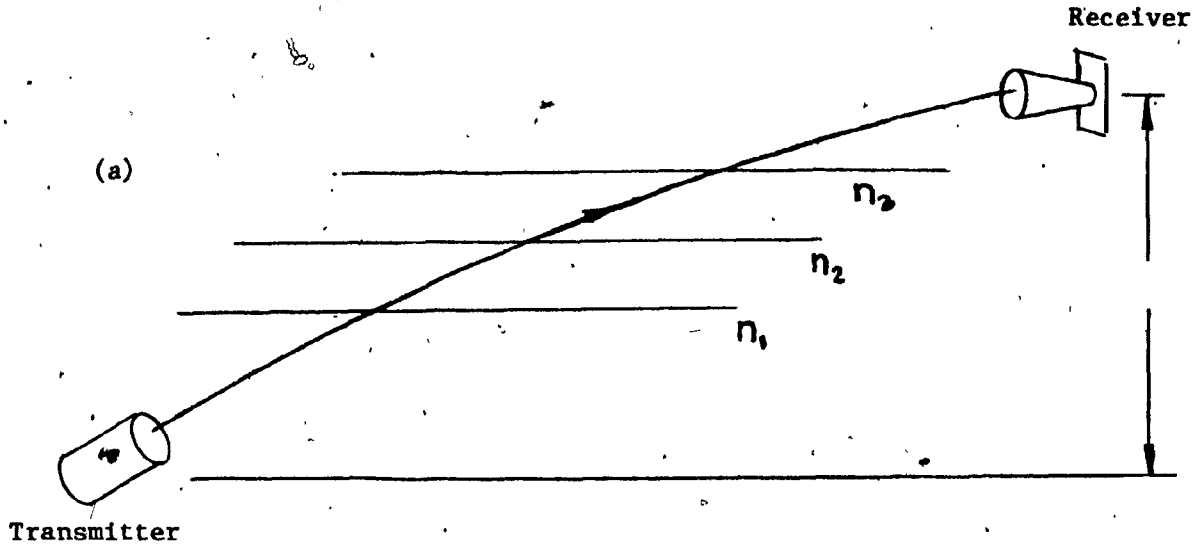

Beam bending in the vertical plane, transmitter and receiver are separated by height h_1

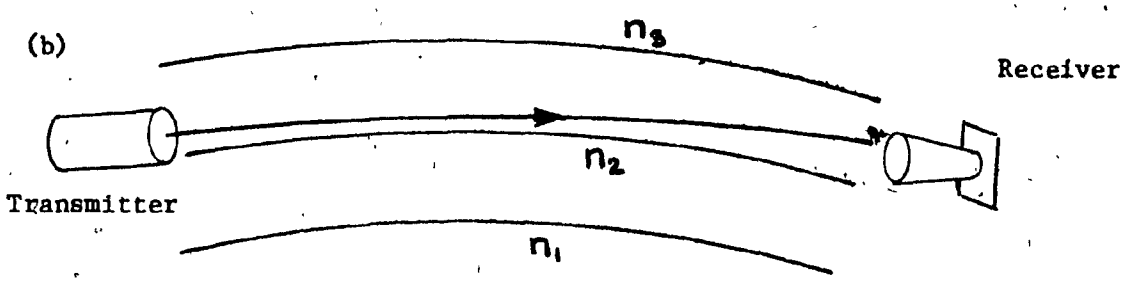

Beam bending in the vertical plane, transmitter and receiver are on the same level.

Figure 2.8 Direction of propagation changes caused by air refractive index variations as a function of altitude.

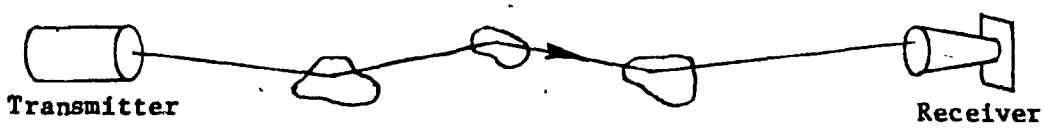

Beam is refracted at random in all planes about the line-of-sight.

Figure 2.9 Direction of propagation changes caused by air refractive index variations due to atmospheric turbulence.

b) Wind and temperature gradients near the earth's surface create turbulences of different refractive indices and change the beam direction about the straight line between the transmitter and the receiver (see Figure 2.9). Consequently, the incident angle at the receiver lens varies and causes random motions of the focal spot over the active area of the photodiode.

The displacements of the beam in the focal plane of the receiver lens caused by this effect are called "spot dancing". If the focal spot leaves the active area of the photodiode during these random motions, part or all of the focussed beam remains undetected and the amplitude of the received signal decreases. In this section the maximum displacement of the beam in the focal plane due to refractive index variations as a function of altitude will be determined. This quantity is taken into account in the design of the opto-electronic communication link described in Chapter III, in order to insure that the focal spot does not leave the active area of the photodiode. The maximum spot displacement due to multiple refractions through turbulences is discussed in Section 2.5.

The curvature of an infrared beam propagating through spherical layers of air (refractive indices n and n + dn) is illustrated in Figure 2.10. A plane wavefront moves from AB to A'B' along a circular ray path. The phase velocities along AA' and BB' are respectively v and v + dv. The angular velocities along AA' and BB' are equal and therefore

$$dv/v = dR/R \qquad (2.39)$$

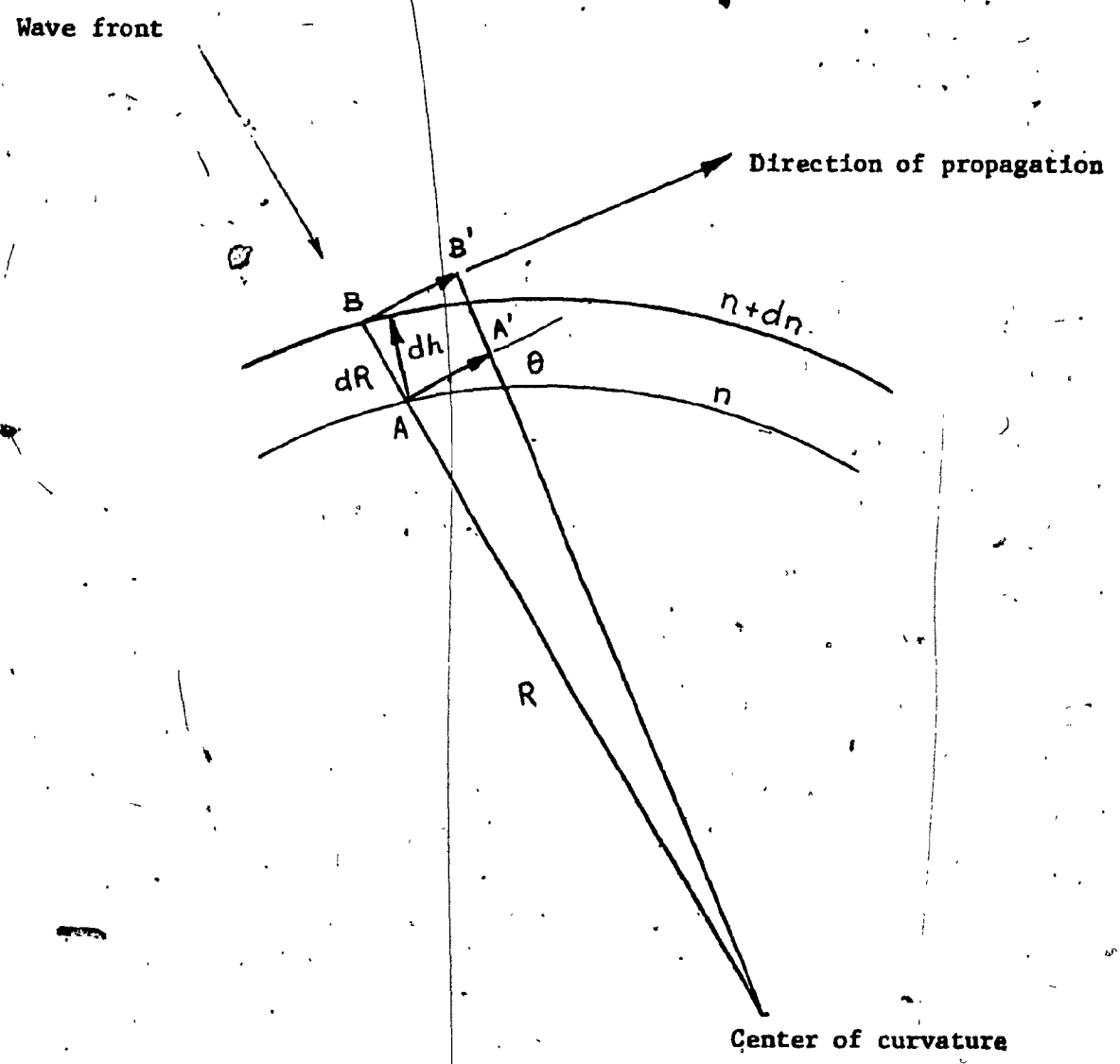

Figure 2.10 Curvature of beam deflection in the vertical plane

where R is the radius of curvature of AA'. Since v = c/n, where c is the velocity of light in vacuum and n is the refractive index, it follows that

$$R^{-1} = -dn/ndR \tag{2.40}$$

Let Θ denote the angle between the ray direction and the constant refractive index surface and let dh be the height above sea level (see Figure 2.10), then

$$dh = dR \cos \Theta \tag{2.41}$$

and by substitution into (2.40)

$$R^{-1} = - \cos \Theta \, dn/ndh. \tag{2.42}$$

For a horizontal path $\Theta = 0$ and

$$R^{-1} = -dn/dh \tag{2.43}$$

where $n \simeq 1$ was assumed. The curvature of the ray path is the absolute value of (2.43). The variations of the atmospheric refractive index with altitude above sea level can be computed from the U.S. Standard Atmosphere [9] adopted by the International Civil Aviation Organization. They are customarily described in terms of the refractivity N_1 which is related to the refractive index by the formula

$$N_1 = (n-1)10^6 \tag{2.44}$$

For optical wavelengths the above reference gives

$$N_1 \simeq 79 \, p/T \tag{2.45}$$

where p is the atmospheric pressure in millibars and T the absolute temperature in °K; both quantities are functions of altitude. Differentiating (2.45) with respect to h and substituting the results into (2.43) produces

$$|R^{-1}| = |(79\partial p/T\partial h - 79p\partial T/T^2\partial h)|.10^{-6}. \tag{2.46}$$

Ochs and Lawrence [10] verified (2.46) experimentally and measured the curvature of a He-Ne laser beam operating at 630 nm over a near horizontal 5.5 km path. They found that the maximum diurnal curvature variation in hot weather is 4 μrad/100 m. Applying their result to a transmission path of 500 m and assuming that the focal length of the receiver lens is 10 cm, the vertical displacement of the focal spot on the photodiode is $20 \times 10^{-6} \times 100 = 2 \times 10^{-3}$ mm. Since the height of a photodiode is much larger than this displacement, the focal spot cannot leave the active area and attenuation due to beam bending can be neglected in the design of the opto-electronic communication link.

2.4 Basic Structure Functions

Molecular absorption as well as Rayleigh and Mie scattering attenuate the irradiance of an electromagnetic wave which propagates through the atmosphere. These phenomena are deterministic functions of distance and are independent of time. However, irradiance is also subjected to random fluctuations caused by air turbulence which are functions of space as well as time and have to be described by statistical methods introduced in this section.

Consider a time dependent continuous random variable $y(t)$ whose graph is shown in Figure 2.11. By sampling this function every Δt seconds at times $t_1, t_2, \ldots t_m$, the mean value is defined by:

$$\overline{y(t)} = (m)^{-1}[y(t_1) + y(t_2) + \ldots + y(t_m)] \qquad (2.46)$$

where $y(t_i)$, $i = 1,2\ldots m$, are the sampled values of $y(t)$ taken at time t_i and m is the total number of samples. The sampled values can be used to determine the histogram of the random variable shown in Figure 2.12. The quantity $m_i/m\Delta y$ is plotted as a function of $y(t_i)$, where m_i/m is the relative frequency of occurrence of $y(t)$ in the interval $y(t_{i+1}) - y(t_i)$ and Δy is the width of this interval. Schwartz [11] has shown that by decreasing Δy the histogram approximates the graph of the continuous probability density function $p[y(t)]$ of the random variable. The probability that $y(t)$ is less than or equal to a fixed value α, i.e. $P[y(t) \leq \alpha]$ is defined by the cumulative distribution function $P^*[y(t)]$

$$P[y(t) \leq \alpha] = P^*[\alpha] = \int_{-\infty}^{\alpha} p[y(t)]dy \qquad (2.47)$$

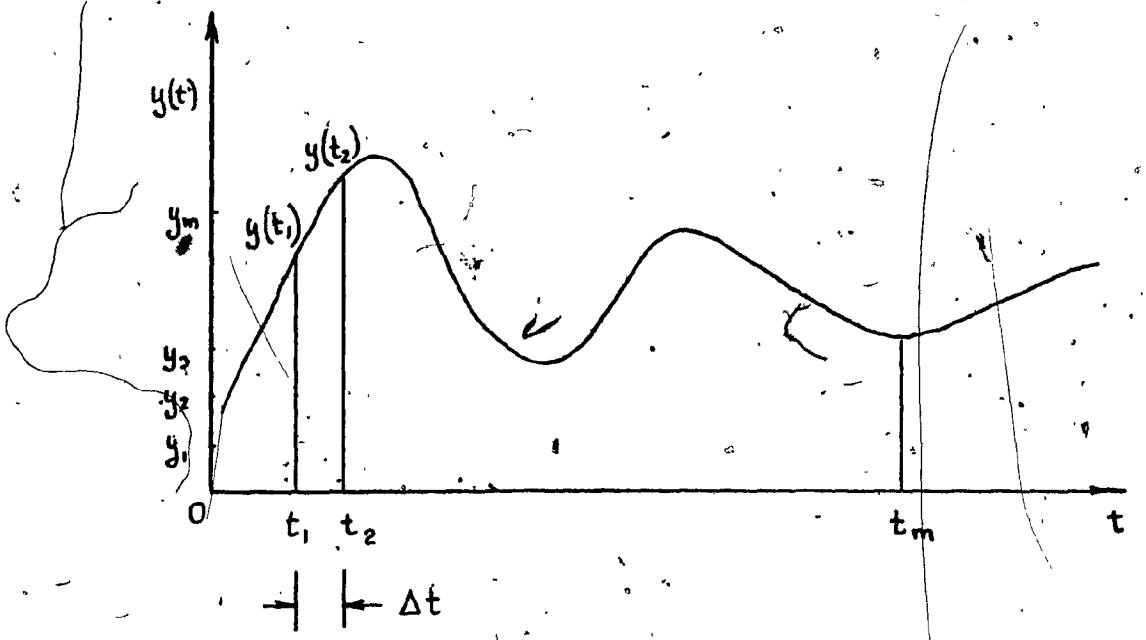

Figure 2.11 Sampled continuous random variable

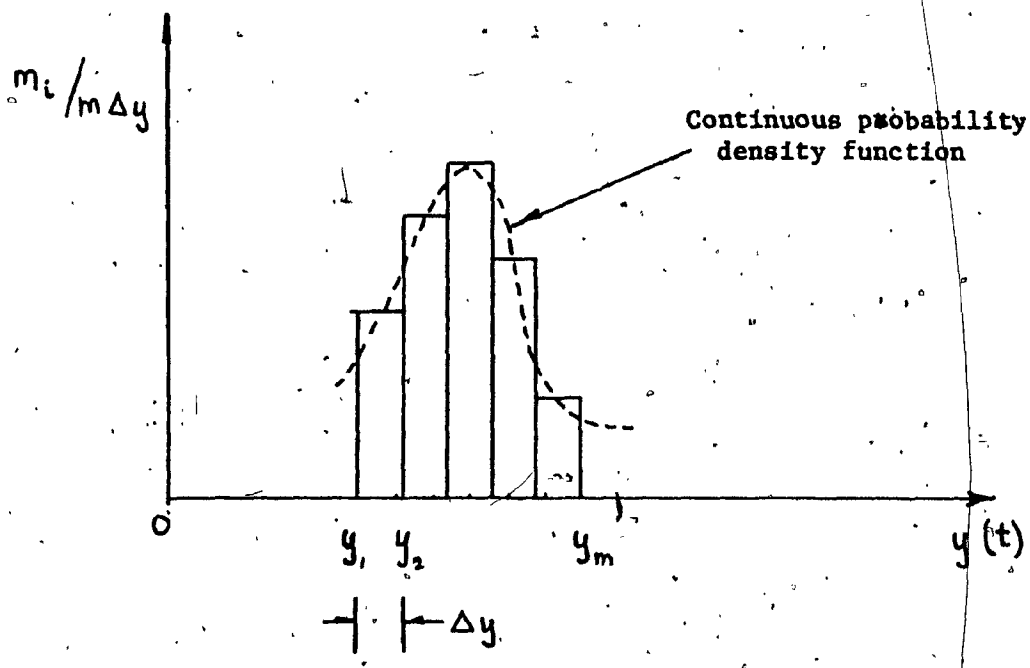

Figure 2.12 Histogram of sampled random variable

Similarly, the probability distribution function of the sampled values $y(t_1), y(t_2) \ldots y(t_m)$ is

$$P^*[y(t)] = \sum_{i=1}^{m} P[y(t_i)]\, u\,[y(t) - y(t_i)] \qquad (2.48)$$

where $u[y(t) - y(t_i)]$ is the unit step function starting at $t = t_i$.

The variance s^2 of $y(t)$ is given by the expression

$$s^2 = \int_{-\infty}^{\infty} p[y(t)]\, [y(t) - \overline{y(t)}]^2\, dy \qquad (2.49)$$

while the variance of the sampled values $y(t_1)$, $y(t_2)$ ... $y(t_m)$ is

$$s^2 = (m-1)^{-1} \sum_{i=1}^{m} [y(t_i) - \overline{y(t)}]^2 \qquad (2.50)$$

If the average value of $y(t)$ is zero (2.49) and (2.50) define the mean square value of $y(t)$, i.e.

$$\overline{y^2(t)} = \int_{-\infty}^{\infty} p[y(t)]\, y^2(t)\, dy \qquad (2.51)$$

in the continuous case and

$$\overline{y^2(t)} = (m-1)^{-1} \sum_{i=1}^{m} y^2(t_i) \qquad (2.52)$$

for sampled values of $y(t)$.

All the characteristics of a random variable discussed so far provided information on the amplitude statistics. The frequency dependence of the random variable is on the other hand described by the autocorrelation function

$$\phi(\tau) = \lim_{T\to\infty} (T)^{-1} \int_{-T/2}^{T/2} y(t)\, y(t+\tau)\, dt \qquad (2.53)$$

Lathi [12] gives the following physical interpretation of the autocorrelation function.

Consider two values $y(t)$ and $y(t + \tau)$ of a random signal at times t and $t + \tau$ (see Figure 2.13a). If the signal contains predominantly low frequencies it varies slowly and therefore it is not expected to change in τ seconds. Thus $y(t)$ and $y(t + \tau)$ have a measure of similarity and it is possible to obtain some information about one from a known characteristic of the other. This is true for reasonably small values of τ. If τ is large the interdependence between $y(t)$ and $y(t + \tau)$ will be reduced. However, the slower the signal variations, the larger will be the value of τ for which $y(t)$ and $y(t + \tau)$ retain their interdependence. If a signal contains predominantly high frequencies, it varies rapidly and therefore $y(t)$ and $y(t + \tau)$ lose their interdependence for small values of τ. A typical autocorrelation function of slowly varying signal is shown in Figure 2.13b while that of a rapidly varying signal is shown in Figure 2.13c. Both graphs illustrate the fact that the autocorrelation function is a measure of the signal variation rate.

Note that for $\tau = 0$ the autocorrelation function is maximum and equal to the mean square value $\overline{y^2(t)}$. The autocorrelation function can be approximately evaluated by sampling $y(t)$ and $y(t + \tau)$ at regular Δt intervals. These samples are then multiplied and added so that the discete approximation of (2.53) is

$$\phi(\tau) \simeq (m)^{-1} \sum_{i=1}^{m} y(t_i)\, y(t_i + \tau) \qquad (2.54)$$

where m is the number of sampling intervals. This method is illustrated in Figure 2.14.

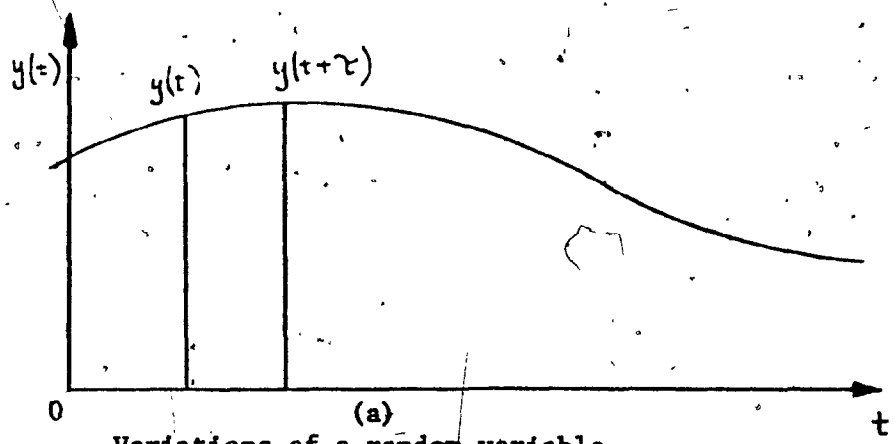

(a)

Variations of a random variable as a function of time

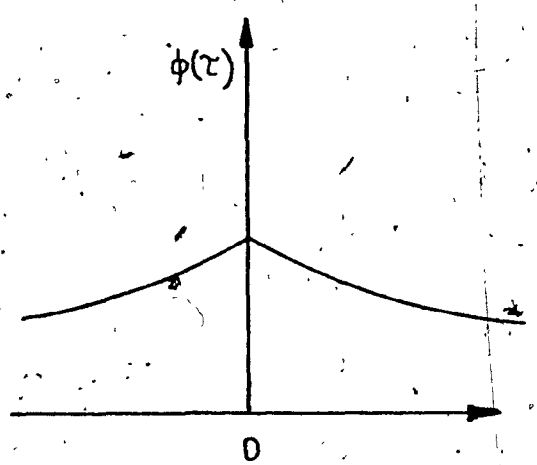

(b)

Autocorrelation function of slowly varying random variable

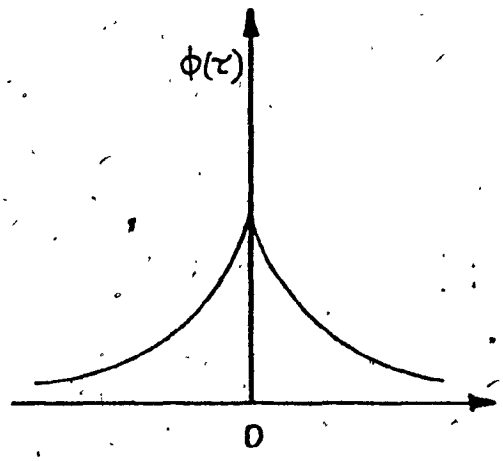

(c)

Autocorrelation function of a rapidly varying random variable

Figure 2.13 Examples of autocorrelation functions

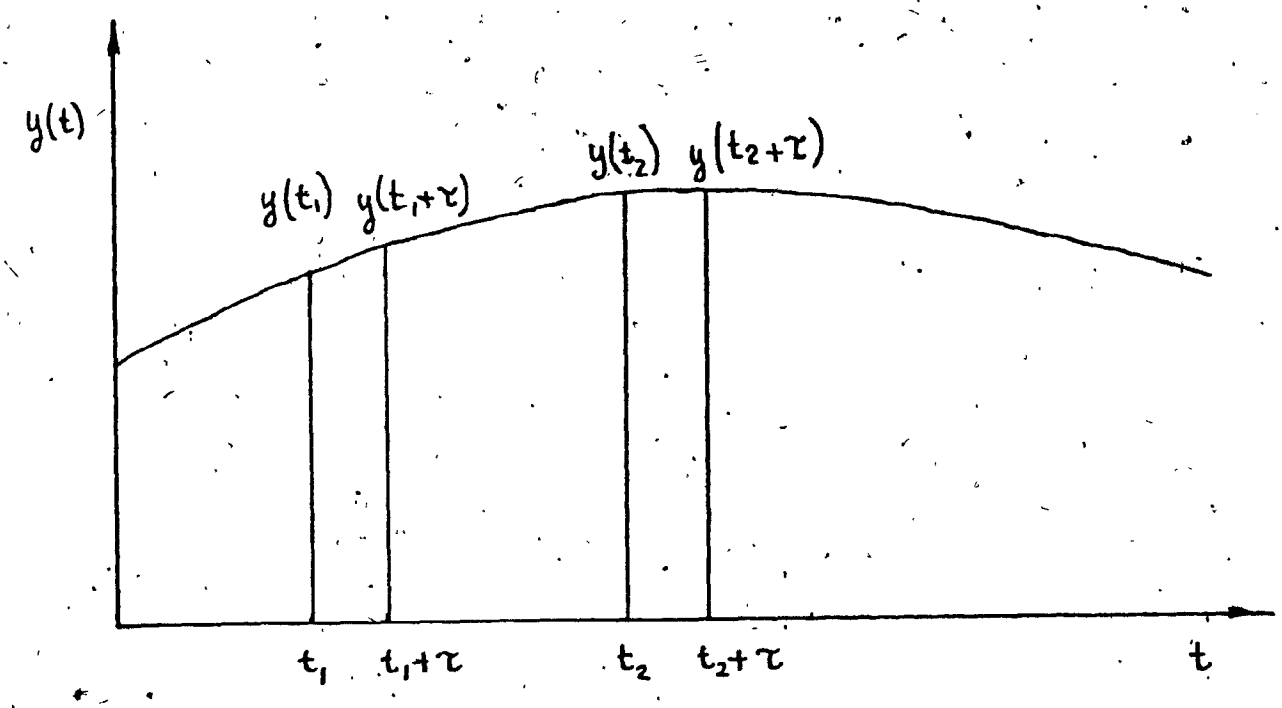

$$\phi(\tau) \simeq (m)^{-1} \sum_{i=1}^{m} y(t_i)\, y(t_i+\tau)$$

Figure 2.14 Determination of autocorrelation function from sampled data

A random process is stationary in the wide sense if its mean is constant and if its autocorrelation function is a function of τ only. Information on the frequency content of a stationary random process is provided by the Wiener-Khintchine theorem which states that the autocorrelation function $\phi(\tau)$ and the power density spectrum $\Phi(\omega)$ are related by Fourier transformation

$$\phi(\tau) = (2\pi)^{-1} \int_{-\infty}^{\infty} \exp(j\omega\tau)\Phi(\omega)d\omega \qquad (2.55)$$

Most random processes occurring in the atmosphere are not wide-sense stationary because their mean and their autocorrelation function vary with time, hence (2.55) cannot be used to determine their power frequency spectra. In order to be able to apply the Wiener-Khinchine theorem to random processes which are not wide-sense stationary Kolmogorov [13] introduced the concept of a random process with stationary increments. He replaced the process which is not stationary in the wide sense by the difference $F_\tau(t) = y(t + \tau) - y(t)$. For moderate values of τ slow changes in $y(t)$ do not affect the value of this difference and it can therefore be considered as a wide-sense stationary process. In this case $y(t)$ is called a random process with stationary increments. While the autocorrelation function is the important characteristics of a stationary random process, the analogous expression used to describe a random process with stationary increments is the structure function

$$D(\tau) = \lim_{T\to\infty}(T)^{-1} \int_{-T/2}^{T/2}[y(t + \tau) - y(t)]^2 \, dt. \qquad (2.56)$$

Note that when $\tau = 0$ the structure function is also zero, hence a low

value of $D(\tau)$ indicates a close interdependence between $y(t)$ and $y(t + \tau)$. By expanding the integrand in (2.56) and using (2.53), the structure function can be expressed in terms of the autocorrelation function

$$D(\tau) = 2[\phi(o) - \phi(\tau)] \tag{2.57}$$

Kolmogorov showed that the Fourier transformation relates the structure function $D(\tau)$ of a random process with stationary increments to the power density spectrum $\Phi(\omega)$ of the same process:

$$D(\tau) = (\pi)^{-1} \int_{-\infty}^{\infty} [1 - \exp(j\omega\tau)]\Phi(\omega)d\omega \ . \tag{2.58}$$

It is apparent from this brief introduction that the methods for analyzing wide-sense stationary random processes and random processes with stationary increments are very similar.

So far the time dependence of wide-sense stationary processes and random processes with stationary increments has been discussed. However, in order to describe phenomena such as wind velocity in a turbulent atmosphere or scalar fields of temperature, humidity and air refractive index it is also necessary to study random processes as functions of space coordinates. A homogeneous random field in space is analogous to a wide-sense stationary process in time therefore a random field is homogeneous if its mean value is constant and if its autocorrelation function is translation independent. A homogeneous random field is called isotropic if its autocorrelation function

$$\phi(x_o) = \lim_{S\to\infty} (S)^{-1} \int_{-S/2}^{S/2} y(x)\ y(x + x_o)dx \tag{2.59}$$

is a function of x_o only, along any straight line within the medium.

The parameter x_o in (2.59) is analogous to τ in (2.53). By analogy with (2.55) the Fourier transformation relates the spatial auto-correlation function $\phi(x_o)$ to the spatial power density spectrum $\Phi(\kappa)$

$$\phi(x_o) = (2\pi)^{-1} \int_{-\infty}^{\infty} \exp(j\kappa x_o)\Phi(\kappa)d\kappa. \qquad (2.60)$$

Atmospheric turbulence contains eddies whose size varies considerably and therefore it cannot be considered as a homogeneous isotropic medium. Hence, (2.59) and (2.60) cannot be used to describe atmospheric turbulence. In analyzing meteorological fields it is appropriate to apply the method of structure functions by making the assumption that the difference $F_{x_o}(x) = y(x + x_o) - y(x)$ is only affected by inhomogeneities in the random field smaller than x_o. This approach is similar to the one introduced previously in the time domain and in this case $y(x)$ is said to be locally isotropic. The spatial structure function is defined by an expression similar to (2.56)

$$D(x_o) = \lim_{S\to\infty} (S)^{-1} \int_{-S/2}^{S/2} [y(x + x_o) - y(x)]^2 \, dx. \qquad (2.61)$$

Fourier transformation relates $D(x_o)$ to the power density spectrum of a random locally isotropic field $\Phi(\kappa)$ by an expression which resembles (2.58)

$$D(x_o) = (\pi)^{-1} \int_{-\infty}^{\infty} [1 - \exp(j\kappa x_o)] \, \Phi(\kappa)d\kappa. \qquad (2.62)$$

Having introduced the basic mathematical concepts required for the study of random processes and random fields, the largest size l_o and the smallest size ℓ_o of the turbulent eddies will be discussed and turbulence phenomena will be described by means of structure functions.

Wind blowing over the earth's surface creates an air flow characterized by the Reynolds number $R = v\ell/\nu$, where v is the air velocity, ℓ is a characteristic length of the air flow and ν is the kinematic viscosity of air. The flow is laminar if $R < R_{cr}$, where R_{cr} is the critical value of Reynolds number; if $R > R_{cr}$ then the flow is turbulent. In Figure 2.15 the air flow is shown to be laminar over a distance ℓ_o. By increasing this dimension Reynolds number exceeds R_{cr} and the transition from the laminar to the turbulent flow is initiated after the occurrence of velocity fluctuations v_n in an atmospheric region of size ℓ_n. The time $\tau = \ell_n/v_n$ is characteristic of the disturbance duration and the kinetic energy per unit mass associated with the disturbance is v_n^2. When the velocity fluctuation takes place the power per unit mass transferred from the initial laminar flow to the turbulent flow is

$$\varepsilon \cong v_n^2/\tau \cong v_n^3/\ell_n \tag{2.63}$$

If the Reynolds number continues to increase, eddies of approximate dimension ℓ_n supply power for the creation of smaller eddies. Tatarski [14] states that this power is constant i.e.

$$v_n^3/\ell_n = v_{n-1}^3/\ell_{n-1} = \varepsilon \tag{2.64}$$

This process continues down to the level of the smallest disturbances of size ℓ_o where the kinetic energy is converted to heat. At this level the velocity gradient is v_o/ℓ_o and accordingly the conversion rate of energy to heat per unit mass is

$$\varepsilon = \nu \, v_o^2/\ell_o^2 \tag{2.65}$$

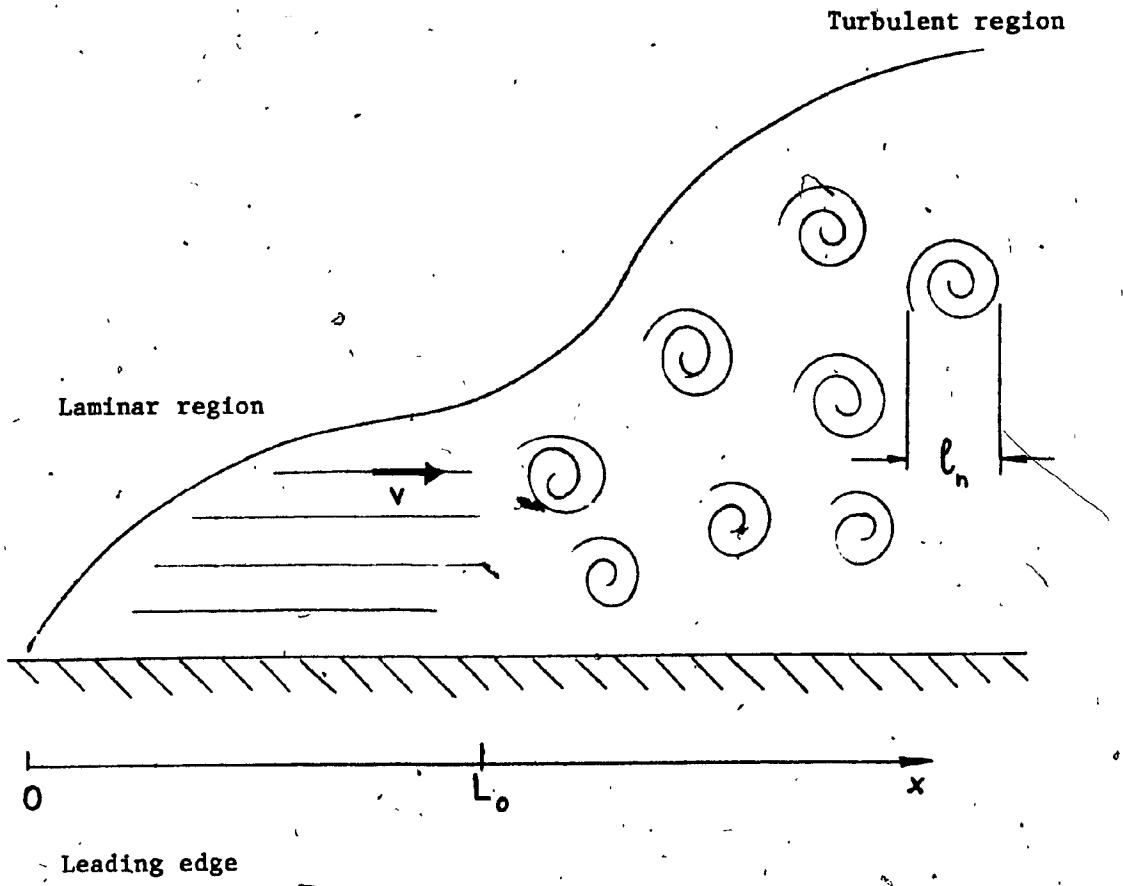

Figure 2.15 Airflow over the earth's surface

Since ν is measured in m^2/s, v_o in m/s and ℓ_o in m, the dimensions of (2.65) are W/kg. Substituting $v_n = v_o$ and $\ell_n = \ell_o$ into (2.63) and combining the result with (2.65), the size of the smallest eddies in terms of ε and ν is obtained:

$$\ell_o \simeq (\nu^3/\varepsilon)^{1/4} \qquad (2.66)$$

According to Tatarski [14] the largest eddy dimension is of the same order as L_o, the length of the laminar region. The smallest eddy size ℓ_o can also be expressed in terms of the largest eddy size L_o. From (2.64) $\varepsilon \simeq v^3/L_o$; substituting this value into (2.66) and bearing in mind that $R = vL_o/\nu$:

$$\ell_o \simeq L_o/R^{3/4} . \qquad (2.67)$$

According to measurements performed by Gray and Waterman [15] the size of ℓ_o varies between 5 to 12 mm. The size of L_o obtained from Lawrence and Strohbehn [16] is of the order of 100 m.

The results of the discussion on structure functions will now be applied to study the wind velocity random field in the turbulent atmosphere. The relationship between velocity components at points x and $x + x_o$ along a straight path in a locally isotropic medium can be represented by the structure function

$$D_v(x_o) = \lim_{S\to\infty} (S)^{-1} \int_{-S/2}^{S/2} [v(x + x_o) - v(x)]^2 \, dx \qquad (2.68)$$

where $\ell_o < x_o < L_o$. Taking into account that $D_v(x_o)$ is the square of a velocity and that from (2.63) $v_o \simeq (\varepsilon x_o)^{1/3}$ it can be concluded that

$$D_v(x_o) = C_2(\varepsilon\, x_o)^{2/3} \qquad (2.69)$$

where C_2 is a dimensionless constant. This equation was derived by Kolmogorov [13] and Oboukhov [17] and bears the name of "two thirds" law. Tatarski [14] has shown that the random field of atmospheric temperature can be described by a similar expression

$$D_T(x_o) = C_T\, x_o^{2/3} \qquad (2.70)$$

where C_T is called the structure coefficient of temperature. The same considerations apply to the random field of atmospheric refractive index

$$D_n(x_o) = C_n^2\, \ell_o^{2/3} \qquad (2.71)$$

where C_n is the structure coefficient of the refractive index. Gurvich, Tatarski and Tsvang [34] established the relationship between C_n and C_T

$$C_n = 69 \times 10^{-6} p\, C_T/T^2 \qquad (2.72)$$

where p is the atmospheric pressure in millibars and T is the ambient temperature in K. C_T can be determined from two average temperature measurements $\overline{T}_1$ and $\overline{T}_2$ at heights h_1 and h_2 above the ground, thus

$$C_T = 1.4(\overline{T}_1 - \overline{T}_2) \,/\, [h^{1/3} \ln (h_1/h_2)] \qquad (2.73)$$

where $h = (h_1 + h_2)/2$.

In the following section structure functions and structure coefficients will be used to describe the effect of atmospheric turbulence on optical wave propagation.

2.5 Optical Wave Propagation through the Turbulent Atmosphere

Atmospheric turbulence is caused by pressure and temperature gradients between layers of air. Turbulence leads to local fluctuations of the air refractive index which causes random variations in the direction of propagation of an optical wave as well as random changes in the irradiance. Figure 2.16 illustrates a plane optical wave and the associated Poynting vector as it emerges from a transmitter. During its propagation through turbulent atmosphere the wave is scattered and breaks up into secondary waves whose Poynting vectors vary in direction and magnitude. The scattered waves are detected by the receiver lens and their energy is concentrated in the focal spot located on the photodector. The direction variations of the Poynting vectors cause incidence angle changes at the receiver and this effect leads to random motions of the focal spot on the photodetector called "spot dancing". Low frequency spot movements associated with beam bending caused by diurnal temperature and pressure changes were described in Section 2.3. In this section "spot dancing" in the range of 1 kHz will be briefly discussed. The magnitude variations of the Poynting vectors lead to fluctuations in the radiant power focussed on the photodetector. Since the photodetector converts radiant power to electrical current, this effect causes an amplitude modulation of the receiver output signal. A discussion of both phenomena follows.

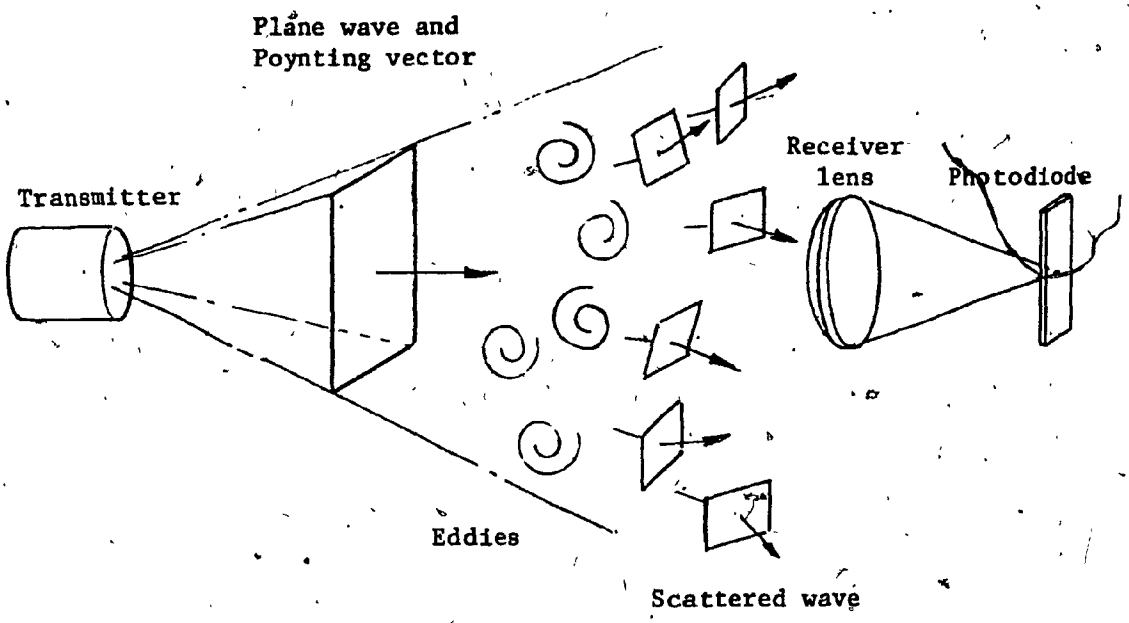

Figure 2.16 Scattering of a plane electromagnetic wave by atmospheric turbulence.

a) High Frequency "Spot Dancing"

Chiba [18] studied variations of the incidence angle due to atmospheric turbulence and found that

$$\overline{\Delta\theta^2} = \overline{\Delta n^2} \times k/\pi \qquad (2.74)$$

where Δn is an increment of the refractive index, θ is the angle of incidence, x is the distance between the transmitter and the receiver and k is the wavenumber of transmitted radiation. Under conditions of strong atmospheric turbulence over a distance of 480 m he measured a maximum laser beam deflection in the horizontal plane of 60 μrad. Assuming that the focal length of the receiver lens is 10 cm, the maximum displacement corresponding to this incident angle variation is $60 \times 10^{-6} \times 100 = 6 \times 10^{-3}$ mm. Since the typical active area width of a photodiode is 0.5 mm the focal spot will remain on the photodetector during its random motion. Therefore, "spot dancing" will not cause amplitude variations of the receiver output signal over an anticipated operating distance of 500 m.

b) Irradiance Variations due to Atmospheric Turbulence

The effect of eddies of characteristic dimensions ℓ on a collimated beam of diameter d is illustrated in Figure 2.17 and summarized in Table 2.1.

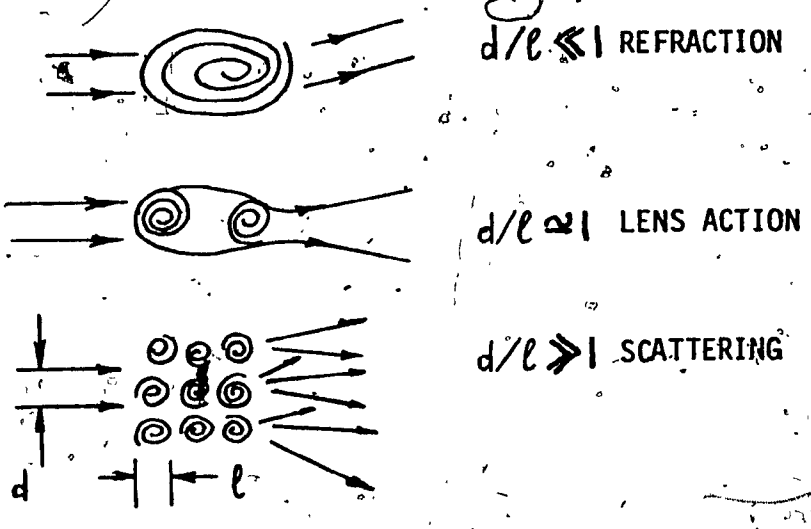

Figure 2.17 Effect of eddies of characteristic length l on a beam of diameter d

TABLE 2.1

Effect of Turbulence Size ℓ on a Collimated Beam of diameter d (after Gruss [19])

d/ℓ	Effect
$\ll 1$	refraction
≈ 1	turbulence acts as a lens and has either a beam spreading or beam focussing effect
$\gg 1$	scattering

The combined effect of several d/ℓ ranges on the output signal of an opto-electronic receiver is observed as an amplitude modulation. The depth of modulation depends both on the structure of turbulence (d/ℓ ranges and path length) as well as on the receiver aperture.

When the receiver aperture diameter is larger than the beam diameter, irradiance variations tend to be integrated and the modulation depth is small. A typical example of an optical transmission test performed under these conditions is described by Gruss [19] who used a collimated He - Ne laser as transmitter and a 150 cm diameter parabolic mirror as a receiver aperture. With this type of opto-electronic transmission link he observed maximum amplitude variations of 0.4 dB over a distance of 600 m. Subramanian and Collinson [20] report a modulation depth of less than 1% when a He - Ne laser was aligned with a 15.2 cm receiver lens. On the other hand, when the receiver aperture is smaller than the beam diameter the modulation is usually large because the

irradiance fluctuations are not integrated. Tatarski [14] as well as Gurvich and Gracheva [21] used small receiver lenses (2 mm diameter) to detect irradiance changes in a collimated beam generated by a mercury arc lamp and measured amplitude variations up to 150 dB. It must be emphasized that the refraction and scattering due to an eddy causes either a decrease or an increase in the detected irradiance as illustrated in Figures 2.18a and 2.18b. In Figure 2.18a a portion of the beam is deflected from the lens and the total radiant flux focussed on the photodiode is decreased. In Figure 2.18b an eddy adjacent to the central portion of the beam increases the irradiance detected by the receiver.

Irradiance variations caused by atmospheric turbulence are also known as scintillation. A quantitative description of scintillation has been given Tatarski [14] who introduced the modulation index σ

$$\sigma^2 = \frac{\overline{H^2(t)}}{\overline{H(t)}^2} \tag{2.75}$$

where $H(t)$ is the irradiance,

$$\overline{H(t)} = (m)^{-1} \sum_{i=1}^{m} H(t_i) \tag{2.76}$$

is the average value of irradiance, while

$$\overline{H^2(t)} = (m-1)^{-1} \sum_{i=1}^{m} [H(t_i) - \overline{H(t)}]^2 \tag{2.77}$$

is the variance of $H(t)$.

Three essential results of Tatarski's study on the effect of optical wave propagation through the turbulent atmosphere will be used in this thesis:

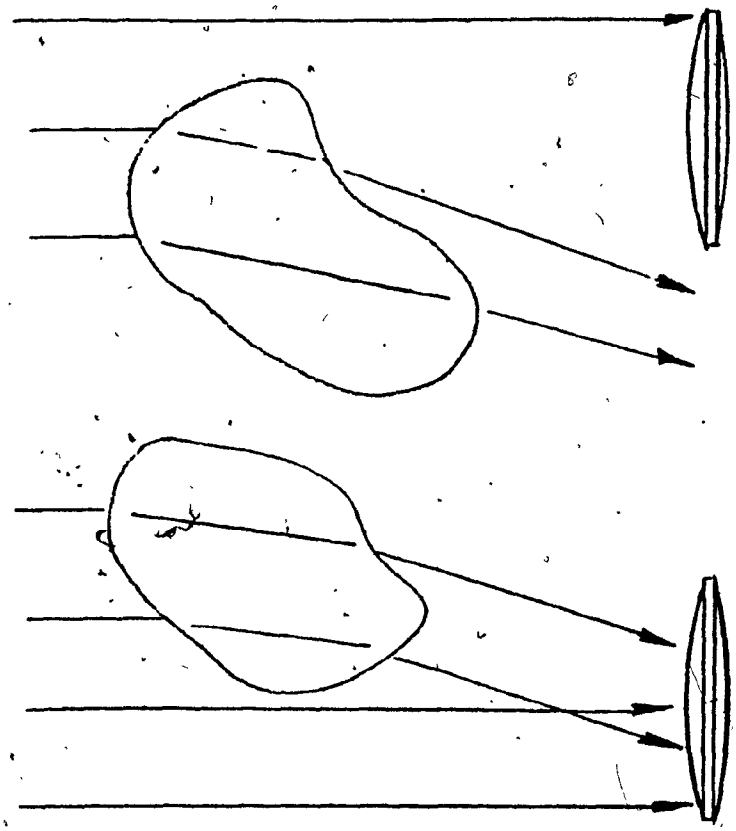

Figure 2.18 Effect of eddies on irradiance detected by the receiver.

i) According to the central limit theorem of probability theory the distribution of the sum of a large number of independent random variables $y_1, y_2 \ldots y_m$ approaches the gaussian distribution:

$$p(y) = \exp[-y^2/2s^2]/(2\pi s^2)^{1/2} \qquad (2.78)$$

where s^2 is the variance of y. Tatarski proved that when an optical wave propagates through a turbulent atmosphere the natural logarithm of irradiance follows a gaussian distribution

$$p(\ln H) = \exp[-(\ln H)^2/2\sigma_T^2]/(2\pi\sigma_T^2)^{1/2} \qquad (2.79)$$

where

$$\sigma_T^2 = (m-1)^{-1} \sum_{i=1}^{m} [\ln H(t_i) - \overline{\ln H(t)}]^2 \qquad (2.80)$$

is the variance of ln H.

ii) The variance of the logarithm of irradiance is given by the expression

$$\sigma_T^2 = 1.23\, C_n\, k^{7/6}\, x^{11/6} \qquad (2.81)$$

where C_n is the structure coefficient of refractive index, k is the wave number in m^{-1}, and x is the propagation distance in m. C_n can be expressed in terms of the refractive index structure function $D_n(x_o)$ and propagation distance by (2.71) or as a function of the temperature

structure coefficient C_T by (2.72). On the other hand C_T is a function of the temperature structure function given by (2.70). It is apparent from these remarks that σ_T is defined by the temperature structure function.

iii) The relationship between σ_T and σ is [21]

$$\sigma_T^2 = \ln(1 + \sigma^2) \tag{2.82}$$

It can be seen from (2.75) that σ increases with the deviation of irradiance from its average value i.e. the absolute value of the difference $H(t) - \overline{H(t)}$. In the absence of scintillation $\overline{H(t)} - \overline{H(t)} = 0$, $\sigma = 0$ and the only causes of irradiance attenuation are absorption, Rayleigh scattering and Mie scattering as shown in (2.21). In the presence of scintillation (2.21) has to be modified to include a function of σ, i.e.

$$H(t) = H_o \exp[-(k_a + k_s)x] f(\sigma) \tag{2.83}$$

where $f(\sigma) = 1$ for $\sigma = 0$. Irradiance $H(t)$ at a fixed distance x from the transmitter is a random function of time whose statistics depends on σ. From (2.81) it is apparent that σ_T is a function of ambient temperature. The diurnal behaviour of σ_T was studied by Ochs [22] who found that the modulation coefficient varies slowly with time: it is minimum during the night, starts increasing at dawn, reaches its maximum after mid-day, and then decreases through dusk. During field tests described in Section 4.2 sudden large variations of σ were observed under conditions of variable cloudiness and the purpose of the next section is to discuss this phenomenon.

2.6 Influence of Sun Irradiance on the Modulation Index

Experiments carried out in summer and winter indicate a large degree of variation in scintillation depending on whether or not the solar disc is obscured by clouds. The transition from one modulation mode to another and the corresponding variation in σ takes place within the very short time of approximately two seconds and therefore this phenomenon cannot be explained by the existing theory according to which C_n is a function of temperature only. The aim of this section is to review similar results described in papers on wave propagation through turbulent atmosphere and to show that no appreciable convective or radiative heat transfer associated with variable solar radiance can take place in such a short time. Since the accepted view is that C_n as well as n are functions of temperature only, the implications of this assumption on the molecular level are examined. Although no theory on the influence of solar irradiance is offered, suggestions for further investigations of this phenomenon are presented.

Kerr [23] observed an increase in scintillation with solar radiance and notes that:

> "Under conditions of broken clouds, the level of scintillation and turbulence is seen to vary from moment to moment, and in fact the response to the sun emerging from a cloud is essentially instantaneous".

Increased scintillation in sunny weather was also reported by Fried et al. [24] as well as by Lawrence and Strohbehn [16]. According to measured data shown in Table 4.2 σ_T varied by a factor of 7.4, within about two seconds when a passing cloud obscured the solar disc. If (2.81) is a complete description of the scintillation phenomenon then

to a variation σ_T^2 by a factor 7.4 within about two seconds must correspond a variation of C_n^2 by the same factor and in the same time. However, this is contradicted by extensive measurements of C_n^2 on sunny days as quoted in the references cited below. It is emphasized that in three cases large variations of C_n were measured over a period of hours and in one case over a period of minutes, but none over a period of seconds:

1) According to Ochs [22] C_n^2 varies by a factor of 15.4 on a summer day between 1200 and 1600 hours. The measurements were performed 2.0 m above the ground.

2) Deitz and Wright [26] recorded a variation of C_n^2 equal to 6.7 in the same time interval at a height of 2.0 m above the ground.

3) Fried, Mevers and Keister [24] report, during the same time interval, a change in C_n^2 by a factor of 1.56 for an optical path which is on the average 15 m above ground.

4) Kerr [23] measured an increase of C_n^2 by a factor of 3.4 within about 2.5 minutes.

From these results it can be concluded that whereas σ_T^2 can change by a factor of 7.4 within about two seconds, there is no evidence that C_n^2 behaves in the same way and therefore (2.81) is not a complete description of the scintillation phenomenon. According to the theory of atmospheric scintillation the parameters which control C_n^2 cannot change in such a short time. In Section 2.6 C_n was defined in terms of the structure coefficient of temperature C_T by (2.72) and C_T was, in turn, described by (2.73). Substituting (2.73) into (2.72) the following

expression is obtained:

$$C_n = 96.6 \times 10^{-6} p(\overline{T}_1 - \overline{T}_2)/[T^2 h^{1/3} \ln(h_1/h_2)] \qquad (2.84)$$

where p is the atmospheric pressure in millibars, $\overline{T}_1$ and $\overline{T}_2$ are average temperatures in K measured by two probes located at heights h_1 and h_2 (in metres) above the ground respectively, T is the ambient temperature and $h = (h_1 + h_2)/2$. Since the ambient temperature T remains constant when the solar disc is temporarily hidden by a cloud a variation of C_n^2 by a factor of 7.4 can only happen if $(\overline{T}_1 - \overline{T}_2)^2$ changes by the same factor in the corresponding time interval. Approximately 15% of the solar energy is absorbed by the atmosphere and the remaining 85% is absorbed by the earth which in turn warms up the atmosphere by convection. Under intermediate cloud conditions it is obvious that an absorption by the earth of variable irradiance followed by an air temperature increase due to convection is unlikely to occur within seconds. Therefore, the only remaining mechanism whereby $(\overline{T}_1 - \overline{T}_2)^2$ could change drastically in a short time would be through the absorption of solar energy by the turbulent air. An attempt will be made to formulate a mathematical model of this heat transfer.

Ochs and Little [28] measured $(\overline{T}_1 - \overline{T}_2)^2$ by means of two platinum filaments 2.5 μ in diameter and 1.5 mm long. Their response time to air temperature changes was 0.3 to 0.9 ms and the two sensors were mounted 10 cm apart at a height of 2 m above the ground. If P_b is the solar radiant power incident at the top of the air column separating the probes and P is the reduced power at the bottom of the air column, P and P_o are related by an expression similar to (2.14)

$$P = P_o \exp(-k_a z) \tag{2.85}$$

where k_a is the molecular absorption coefficient and z is the height of the air column. The amount of radiant power ΔP absorbed by the air column of unit cross-sectional area is given by the equation

$$\Delta P = P_o[1 - \exp(-k_a z)] \tag{2.86}$$

where $P_o = 0.135$ W/cm^2 solar radiation constant

$k_a = 0.14$ km^{-1} $= 1.4 \times 10^{-6}$ cm^{-1} (from [29])

$z = 10$ cm.

whence $\Delta P = 1.89 \times 10^{-6}$ W.

Assuming that the transition from high to low scintillation mode during variable cloud cover lasts 2 s the energy ΔQ supplied to the previously defined air column is

$$\Delta Q = 3.78 \times 10^{-6} \text{ J}$$

$$= 9.03 \times 10^{-7} \text{ cal.} \tag{2.87}$$

This energy warms up the air column according to the heat transfer equation

$$\Delta Q = m\, c_p\, \Delta T \tag{2.88}$$

where $m = 0.0129$ gm, mass of 10 cm^3 of air

$c_p = 0.240$ cal gm^{-1} K^{-1}, specific heat of air at constant pressure

ΔT = temperature increase in air column (1 cm^2 x 10 cm).

The above values result in a temperature increase

$$\Delta T = 2.92 \times 10^{-4} \text{ K}$$

Based on this result it can be concluded that if the temperature of the air surrounding the two temperature probes increases by 2.92×10^{-4} K it is unlikely to cause a variation in $(\overline{T}_1 - \overline{T}_2)^2$ by a factor of 7.4. This implies that the structure coefficient of refractive index C_n is not only a function of temperature, but also a function of solar irradiance.

The structure coefficient of refractive index C_n is related to the refractive index structure function $D_n(x_o)$ by (2.71). Therefore, the assumption that C_n is a function of temperature only implies that n is also temperature dependent, provided x_o is constant. The implication of this assumption at the molecular level will now be reviewed and it will be shown that if C_n depends on solar irradiance, n must also be a function of solar irradiance.

The refractive index of air is defined as the ratio of electromagnetic wave velocity in vacuum, c, to that in air, v

$$n = c/v = (\varepsilon \mu / \varepsilon_o \mu_o)^{1/2} \qquad (2.89)$$

where ε and μ are respectively the permittivity and permeability of air while ε_o and μ_o are the vacuum permittivity and permeability. Since air is non-magnetic $\mu = \mu_o$, and

$$n = K_e^{1/2} \qquad (2.90)$$

where $K_e = \varepsilon/\varepsilon_o$ is the relative permittivity.

When an electromagnetic wave propagates through a dielectric the electric charge distribution within its molecules is distorted and electric dipole moments are created. The resultant dipole moment per unit volume, called the electric polarization $\vec{P}$, is for linear, isotropic media given by

$$(\varepsilon - \varepsilon_o)\,\vec{E} = \vec{P} \tag{2.91}$$

When the dielectric is subjected to an incident harmonic electromagnetic wave, its internal charge structure will experience time-varying forces as well as torques. The refractive index of the dielectric is dispersive and it is a function of frequency of the incident electromagnetic field. It was shown in Section 2.2 that the displacement phasor $\tilde{X}(\omega)$ can be expressed as a function of the electric field phasor $\tilde{E}$ by (2.2). The elementary electronic dipole moment is equal to the product of the electronic charge e and the displacement $\tilde{X}(\omega)$, thus for an electron density N_e the electric polarization is

$$\tilde{P}(\omega) = e\,N_e\,\tilde{X}(\omega). \tag{2.92}$$

Substitution of the value of $\tilde{X}(\omega)$ from (2.4) into (2.92) gives

$$\tilde{P}(\omega) = j\,e^2\,N_e\,\tilde{E}_x/m\gamma\omega_a\,[1 + 2j(\omega - \omega_a)/\gamma]. \tag{2.93}$$

Combining (2.91) and (2.93)

$$\varepsilon = \varepsilon_o + je^2N_e/m\gamma\omega_a[1 + 2j(\omega - \omega_a)/\gamma] \tag{2.94}$$

Bearing in mind (2.90), n as a function of ω is given by the following expression

$$n^2(\omega) = 1 + je^2N_e/m\gamma\omega_a\varepsilon_o[1 + 2j(\omega - \omega_a)/\gamma] \qquad (2.95)$$

The magnitude of the second term on the right hand side of (2.95) is much smaller than one; a Taylor's series expansion of this equation and truncation after the second term yields

$$n(\omega) = 1 + je^2N_e/2m\gamma\omega_a\varepsilon_o[1 + 2j(\omega - \omega_a)/\gamma] \qquad (2.96)$$

In (2.96) a single resonant frequency ω_a was presumed. However, the above expression can be used to describe the refractive index of a gas mixture such as air, by assuming that there are N molecules per unit volume, each containing k_i oscillators having resonant frequency ω_{ai}. Thus for a composite system [3].

$$n(\omega) = 1 + je^2N \sum_i k_i/2m\gamma\omega_{ai}\varepsilon_o[1 + 2j(\omega-\omega_{ai})/\gamma] \qquad (2.97)$$

where k_i are weighting factors which satisfy the requirement $\sum_i k_i = 1$. It is important to realize that (2.97) defines $n(\omega)$ on the molecular and atomic level. The temperature dependence of $n(\omega)$ becomes apparent by making a transition from the microscopic definition of $n(\omega)$ provided by (2.97) to a macroscopic definition of $n(\omega)$. An example of this approach is described by Hodara [30]. In (2.97) N can be replaced by N_1/V where N_1 is the number of molecules in a volume V, Equation (2.97) therefore becomes

$$n - 1 = (1/V)je^2N_1 \sum_i k_i/2m\gamma\omega\varepsilon_o[1 + 2j(\omega - \omega_a)/\gamma] \qquad (2.98)$$

$$= C/V$$

where C is the multiplier of 1/V. The ideal gas law states that

$$pV = RT \qquad (2.99)$$

where p is the pressure, V is the volume, R is the gas constant and T is the absolute temperature. Under isobaric conditions the differential form of the above equation is,

$$\Delta V/V = \Delta T/T \qquad (2.100)$$

Differentiating (2.98) with respect to V and taking into consideration (2.100) yields

$$\Delta n = -(n - 1)\ \Delta T/T \qquad (2.101)$$

This expression is independent of C and implies that n and consequently C_n are functions of temperature only. Since it was found experimentally that C_n depends on temperature as well as solar irradiance, (2.101) fails to provide a complete description of scintillation. The question then arises as to how (2.98) and (2.99) can be combined to show the effect of temperature as well as solar irradiance on scintillation. A plausible answer is to substitute V from (2.99) into (2.98).

$$n = 1 + Cp/RT \qquad (2.102)$$

The coefficient C in (2.98) describes the molecular absorption of an

electromagnetic radiation and its magnitude is very likely affected by solar irradiance. It is therefore suggested that the increased scintillation observed when the solar disc, initially obscured by a cloud, becomes perfectly visible is due to a variation of C while p and T remain constant. The effect of the observed phenomenon appears to be an increase in absorption and/or scattering of infrared beams propagating through the atmosphere due to the polarization of air molecules by solar irradiance. It is beyond the scope of this thesis to derive a theory of scintillation variations due to solar irradiance. However, experimental methods for investigating this phenomenon in the field and under laboratory conditions are presented in Section 5.4.

CHAPTER III

SYSTEM DESIGN

3.1 Design Objectives.

The aim of this chapter is to describe the electrical and optical design of two opto-electronic communication links consisting of a narrow-beam laser transmitter, an omnidirectional xenon arc transmitter and a common receiver. First the electrical as well as the optical characteristics of the laser and xenon transmitters are discussed. Based on measurements of laser and xenon radiant power outputs the irradiance as a function of distance is calculated for both communication channels. The photodetector output signals in the receiver are then determined bearing in mind the irradiance values at the maximum range of 500 m, the area of the receiver lens and the responsivity of the photodiode. After estimating the shot noise and the Johnson noise at the photodetector outputs, the signal-to-noise ratios on both channels are evaluated. Specifications for the laser and xenon communication links were drawn up after studying the requirements of prospective users. A summary of these specifications is presented below.

a) Laser Communication Link

i) Transmitter

Radiation source	gallium-arsenide laser diode
Maximum horizontal divergence of laser beam	0.4 mrad at half-power points

Maximum vertical divergence of laser beam	300 mrad at half-power points
Range	50 m to 500 m
Minimum peak output	1 W
Spectral characteristics	near infrared
Maximum pulse repetition rate	25.6 kHz

ii) Receiver

Maximum horizontal acceptance angle of receiver	4 mrad
Maximum vertical acceptance angle of receiver	300 mrad

b) Xenon Arc Communication Link

i) Transmitter

Radiation source	xenon flash tube
Horizontal radiation pattern	uniform through 360°
Maximum vertical divergence of xenon beam	300 mrad at half-power points
Range	50 m to 500 m
Spectral characteristics	near infrared
Maximum pulse repetition rate	160 Hz

ii) Receiver

Maximum horizontal acceptance angle of receiver	4 mrad
Maximum vertical acceptance angle of receiver	300 mrad

3.2 Laser Transmitter

a) Drive Circuit

The selected radiation source was a type SG2005 gallium-arsenide laser diode manufactured by RCA. It has a typical radiant power output of 5 W at 904 nm when driven by a current of 20 A. The maximum permissible duty cycle for this device is 0.1%, which means that at the specified frequency repetition rate of 25.6 kHz the pulse length must not exceed 39.0 ns. The drive circuit is illustrated in Figure 3.1. Transistors Q1 and Q2 in conjunction of R1 and C2 form a 25.6 kHz relaxation oscillator. The transistors are connected in the avalanche mode and their operation is similar to that of a unijunction transistor. Transistor Q3 acts as a pulse width limiter, while the six integrated circuits U1, each delay the pulse by 6 ns for a total of 36 ns. A pulse generated by the relaxation oscillator is applied to the chain of U1 elements and after a 36 ns delay it switches on Q3 and recharges C3. The delayed output appears at the base of Q4 which in turn drives Q5. Capacitors C7 and C8 are used to stabilize the supply voltage, while Q7 and Q8 are driving the laser diode GR5. Diode CR2 separates the 20 V and 9 V supply voltages.

b) Optics

The active area of the laser diode is 1.53×10^{-2} cm high and 2.04×10^{-4} cm wide. Its radiation pattern illustrated in Figures 3.2a and 3.2b subtends an angle of 20° in the vertical plane and an angle of 15° in the horizontal plane, both measured between half-power points. The cross-section of the diode is illustrated in Figure 3.2c. In order to achieve the specified beam dimensions an optical system illustrated in Figure 3.3 is used. The optical system consisting of lenses 1 and 2

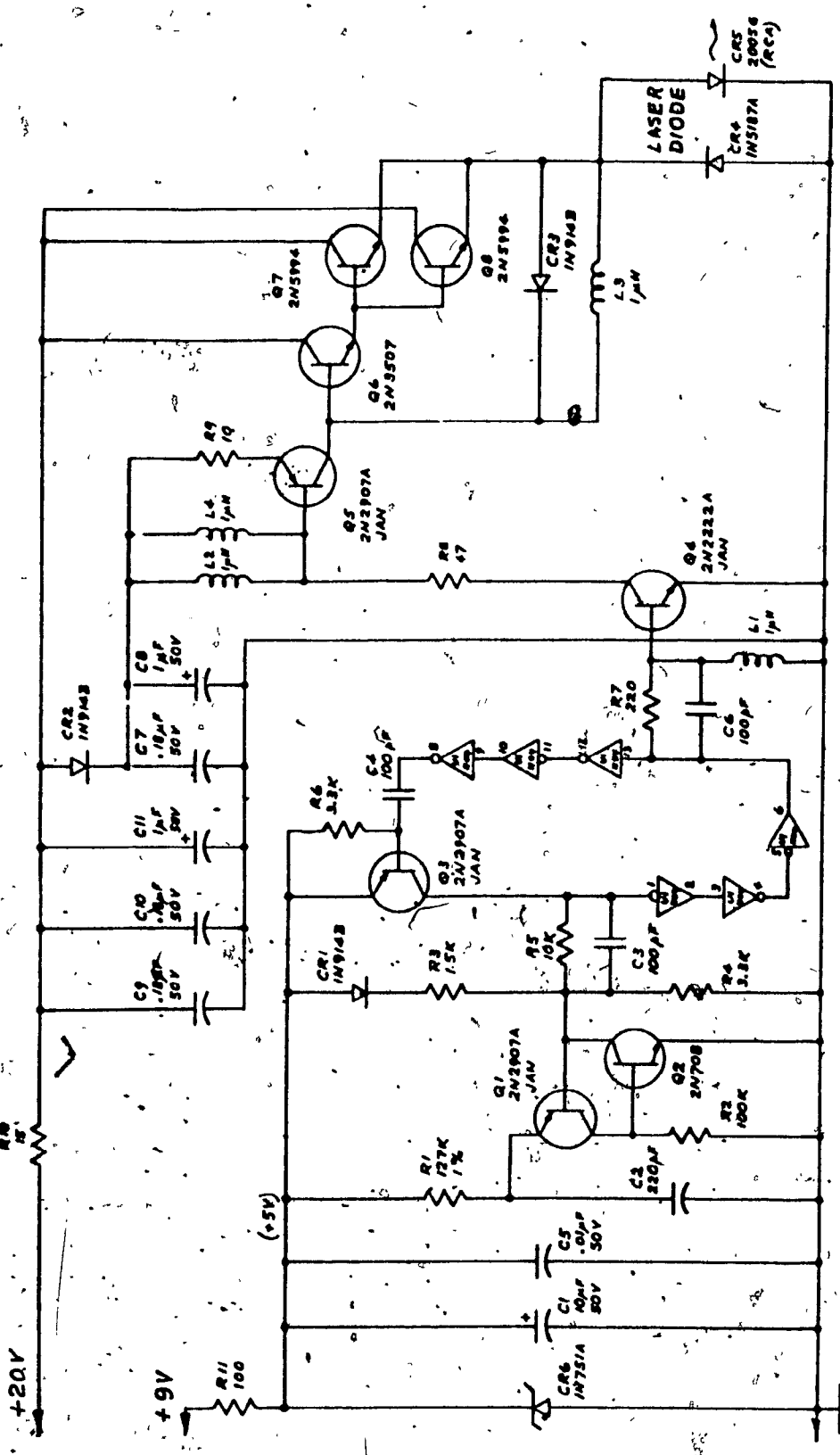

Figure 3.1 Drive circuit for laser diode

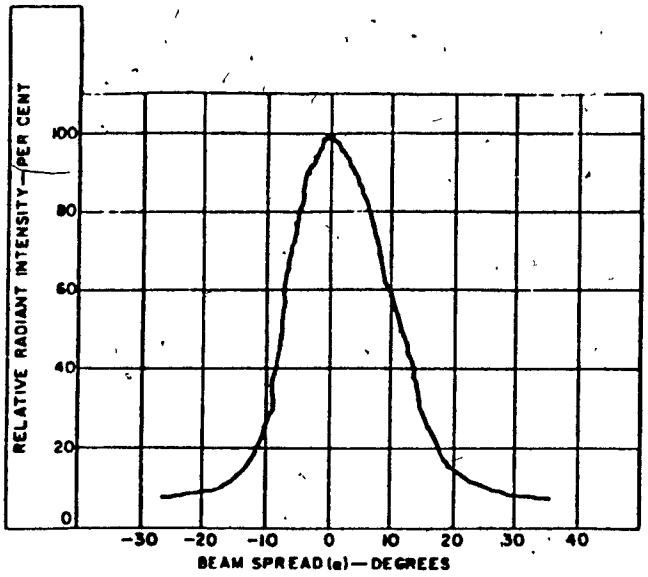

(a) Horizontal plane

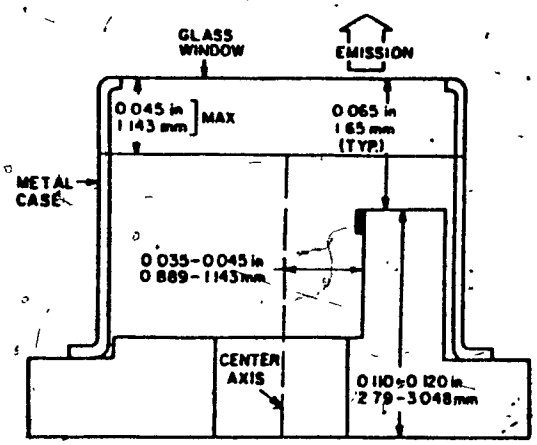

(c) Cross section of SG 2006 laser diode.

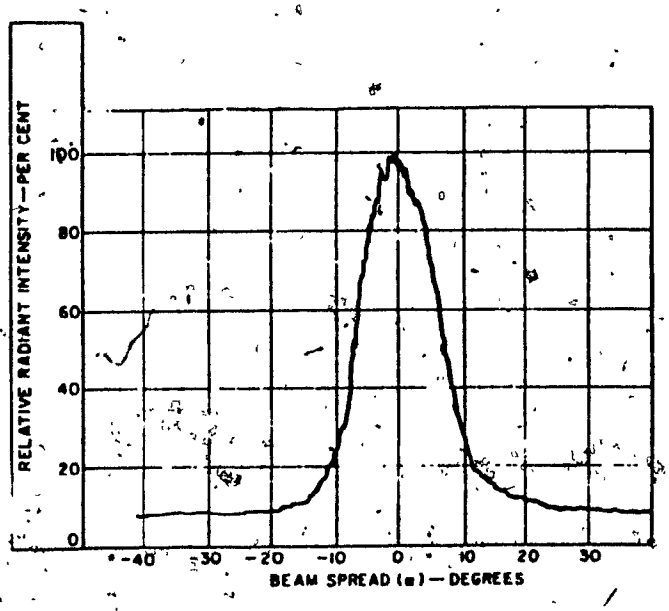

(b) Vertical plane

Figure 3.2 Radiation pattern and outline of gallium-arsenide laser diode.

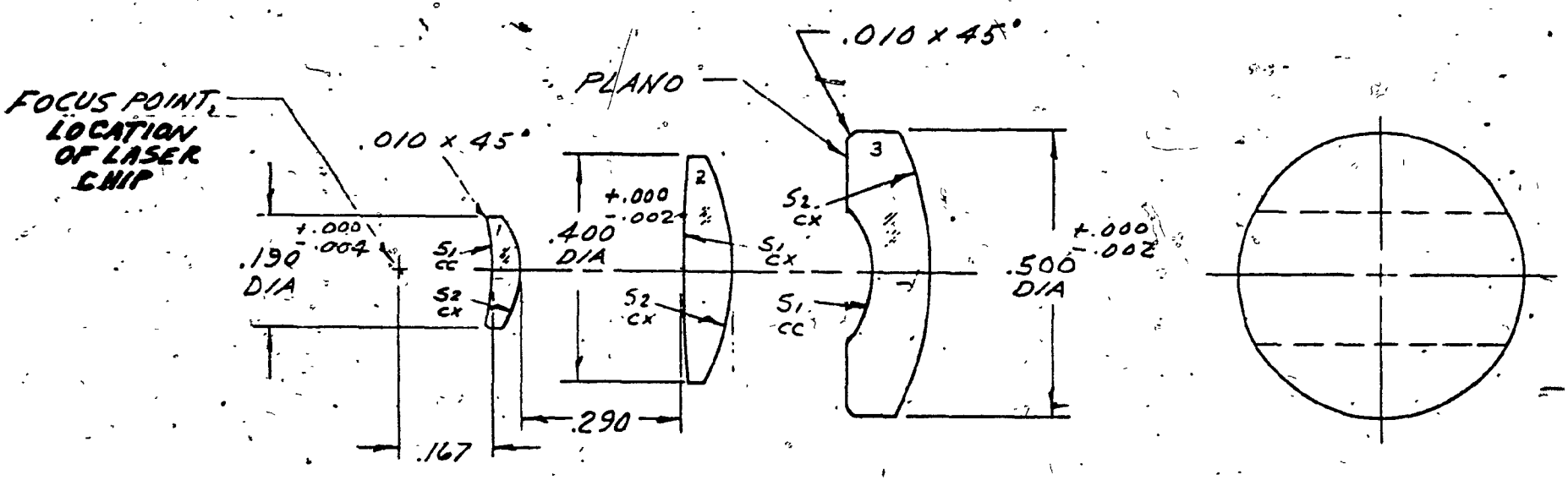

PART NO.	EL. NO	MAT'L.	S_1 RAD	S_1 C.A.	S_2 RAD	S_2 C.A.	E.T.	TOTAL THK.	C.T.	WEDGE
-1	1	BK-7	.3268 ± .008	.125	.1531 ± .004	.140	.032	.051	.051 ± .003	6 MIN
-2	2	BK-7	2.5826 ± .064	.340	.4156 ± .006	.340	.026	.085	.085 ± .004	6 MIN
-3	3	BK-7	.170 ± .005	.240	.578 ± .015	.345	.093	.150	.061 ± .004	10 MIN

Dimensions in inches

Figure 3.3 Optical projection system of laser transmitter.

has a short focal length and gathers over 90% of the radiant flux emitted by the laser diode which is positioned at its focus. The collimated beam emerging from lens 2 illuminates the cylindrical lens 3 which disperses the beam in the vertical plane but does not affect its width in the horizontal plane. A typical ray tracing is illustrated in Figure 3.4. The measured horizontal and vertical patterns of the laser diode-optical system combination are illustrated in Figures 3.5 and 3.6. These graphs show that the laser transmitter meets the specified beam shape requirements. All measurements were performed by means of a reverse biased silicon photodiode. This device acts as a current source whose output is proportional to the radiant flux input. The numerical values plotted on the graphs correspond to the amplitudes of voltage pulses which are generated when the photodiode current passes through a precision resistor. An oscilloscope was used to observe these signals.

The calibrated silicon photodiode was also used to measure the total radiant power output of the semiconductor laser. It was positioned within 0.5 cm from the transmitter thus insuring that its active area intercepted the whole flux. To avoid saturating the detector, the laser output signal was attenuated by calibrated neutral density filters. The radiant flux to current conversion efficiency of the device is called responsivity and is measured in A/W. From the responsivity, the voltage measured across a precision load resistor by means of an oscilloscope and the known attenuation of the filter the peak radiant flux was found to be 1.0 W. The radiant flux emanating from the laser diode is confined by the optical system to a solid angle defined by the horizontal divergence ζ and vertical divergence η, both

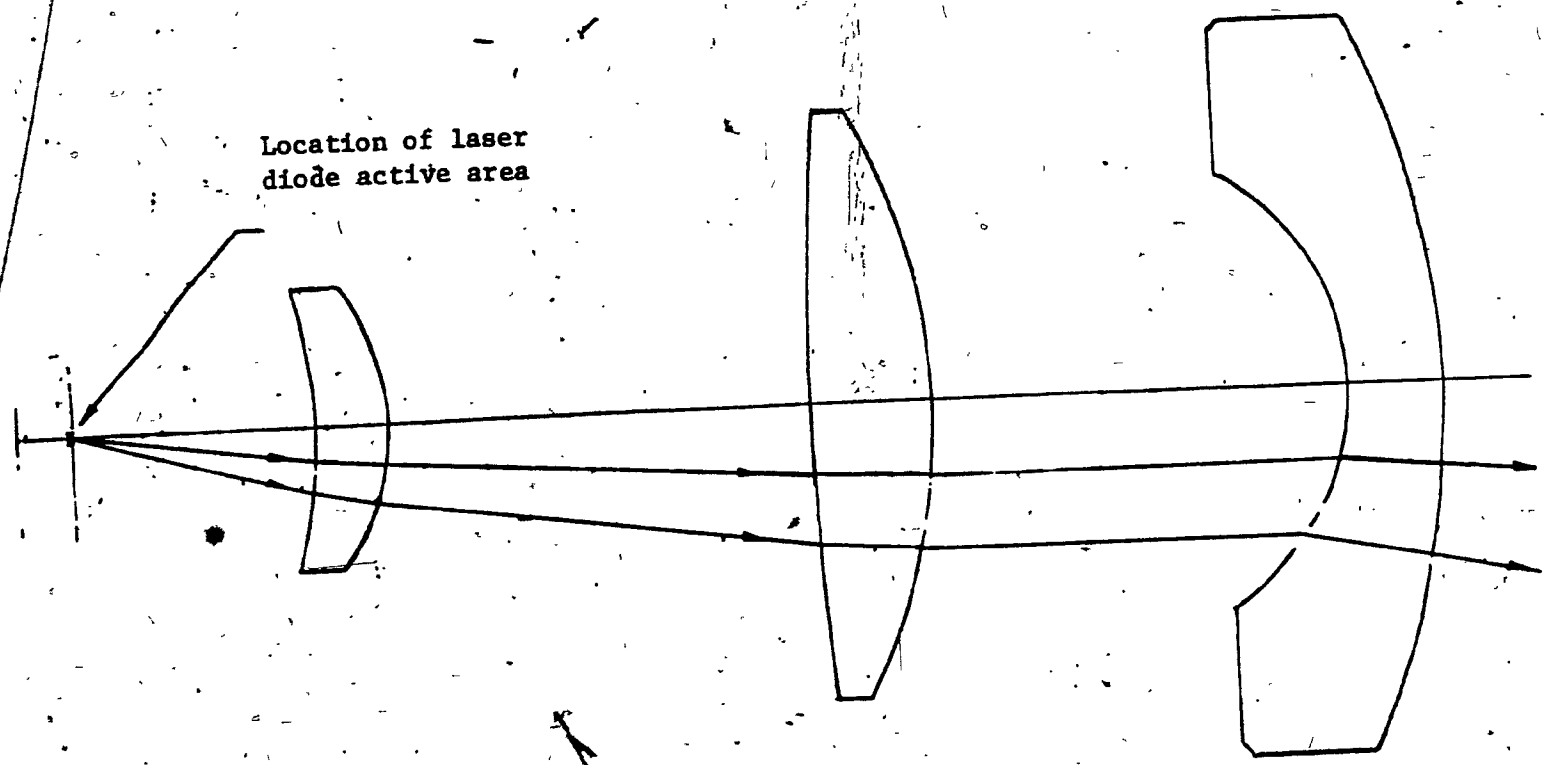

Figure 3.4 Ray tracing through laser projection system

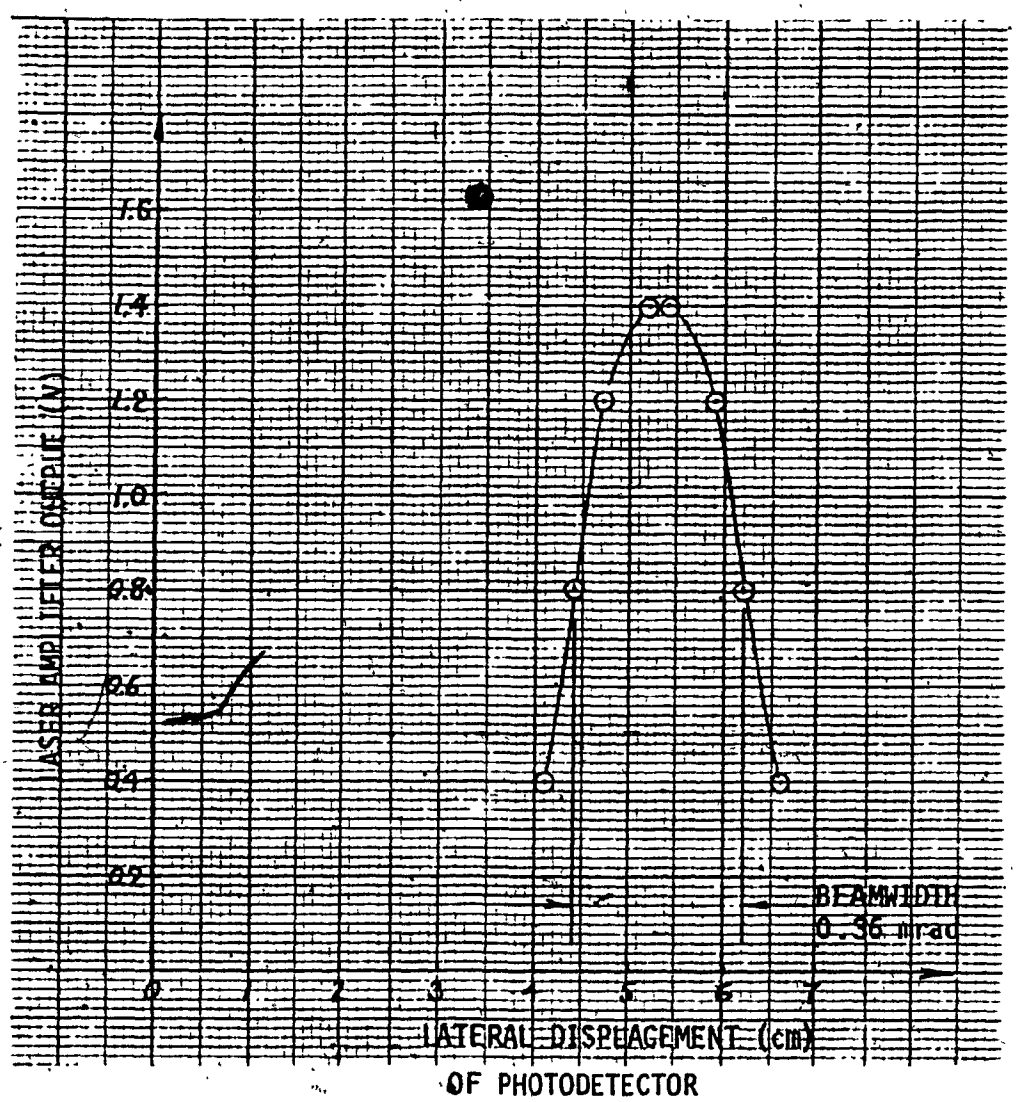

Figure 3.5 Radiation pattern of laser transmitter in the horizontal plane.

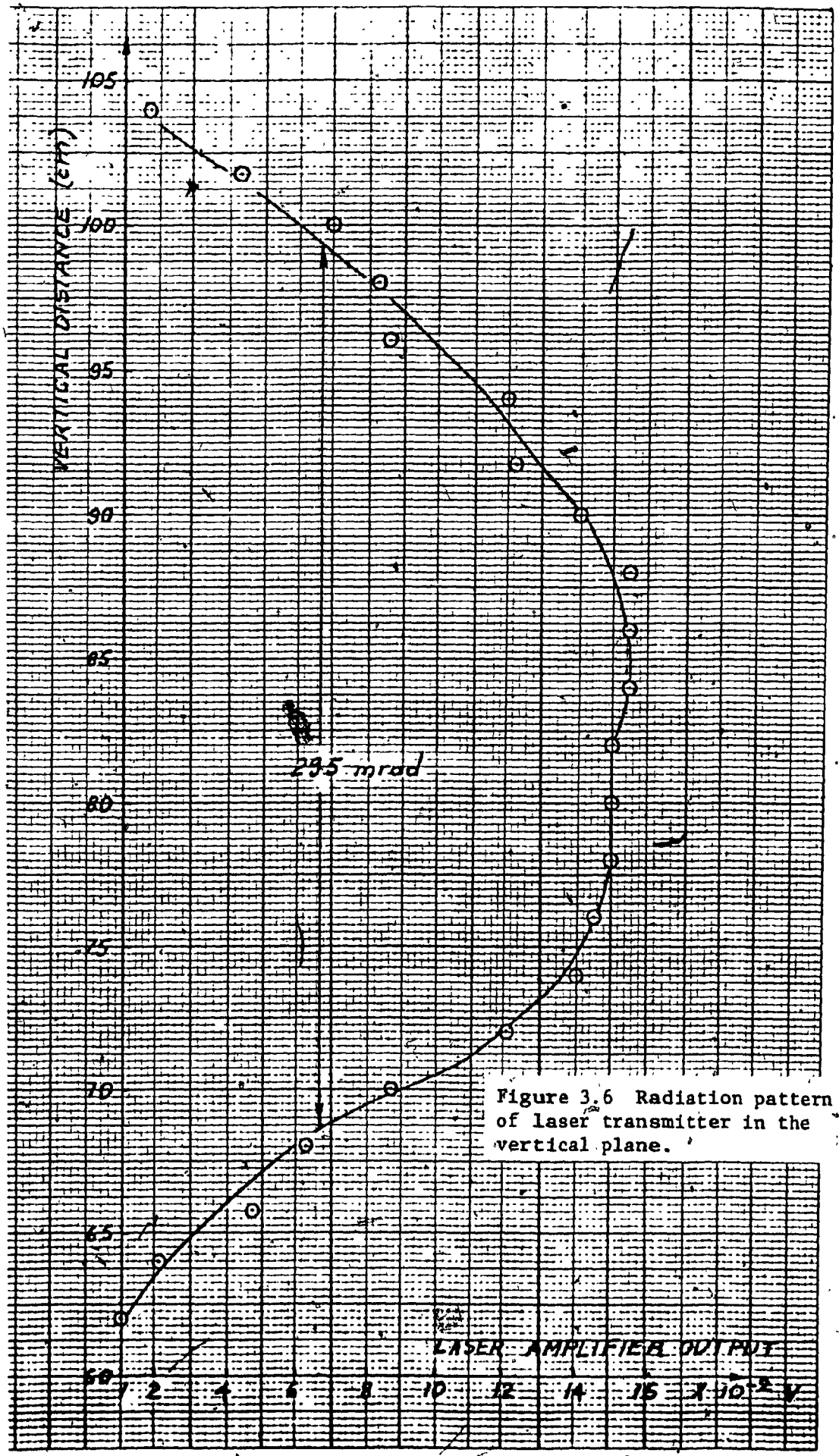

Figure 3.6 Radiation pattern of laser transmitter in the vertical plane.

measured in mrad between the half-power points. The cross-sectional area A_L of the laser beam as a function of distance x in m can be derived from the geometry shown in Figure 3.7

$$A_L = \zeta \eta x^2. \tag{3.1}$$

The laser irradiance over this area varies as shown in Figures 3.5 and 3.6. For the purpose of estimating the output signal from the infrared receiver at various distances, it will be assumed to be uniformly distributed over A_L. Based on this simplification the irradiance H_L as a function of distance is given by

$$H_L = t_L P_L / A_L$$

$$= t_L P_L / \zeta \eta x^2 \tag{3.2}$$

where t_L, the transmittance of the atmosphere over a distance x (omitting the effect of scintillation), is given by

$$t_L = H_L / H_{LO}$$

$$= \exp\left[-(k_a + k_s)\right] x \tag{3.3}$$

where H_{LO} is the irradiance at the laser transmitter, k_a is the molecular absorption coefficient and k_s is the volume scattering coefficient. The theoretical estimate of transmission losses discussed in Section 2.2 has shown that the effects of Rayleigh and Mie scattering are very small compared to molecular absorption and that the approximate transmittance calculated for a 0.5 km path is $t_L \approx 0.85$. Hence the laser irradiance as a function of distance deduced from (3.2) is

$$H_L = 0.85\ P_L / \zeta \eta x^2 \quad W/m^2 \tag{3.4}$$

Substituting the numerical values

$$P_L = 1.0\ W$$

$$\zeta = 0.36\ mrad$$

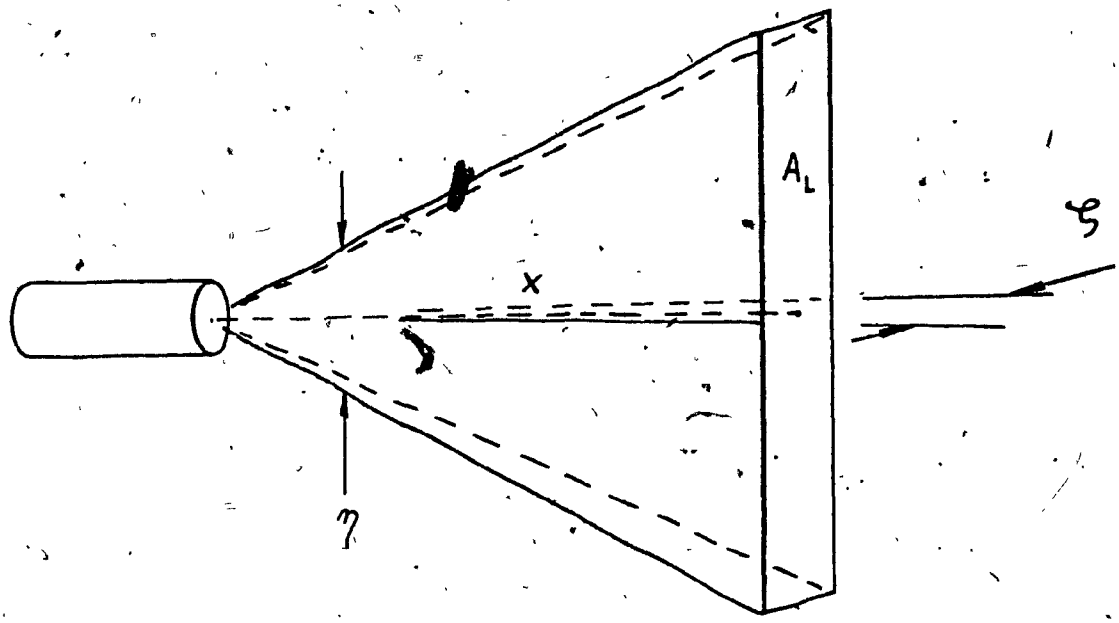

ξ : horizontal divergence angle
η : vertical divergence angle

Figure 3.7 Geometry of laser beam

$$\eta = 295 \text{ mrad}$$

$$x = 500 \text{ m}$$

into (3.4) one obtains for the irradiance

$$H_L = 0.0320 \text{ W/m}^2 \tag{3.5}$$

3.3 Xenon Transmitter

The selected radiation source was a type FX 48B xenon flash tube (see Figure 3.8) manufactured by the EG & G Corporation; the associated drive circuit is shown in Figure 3.9. The pulses from a 160 pps oscillator (not shown) are applied to the trigger gate of a silicon controlled rectifier. The pulse transformer generates a high voltage pulse which is applied to the electrodes of the xenon flash tube. The 0.22 μF storage capacitor is charged to 680 V and discharged 160 times per second so that the total energy input E per flash is

$$E = 1/2\ CV^2 = 5.12 \times 10^{-2} \text{J} \tag{3.6}$$

The gas discharge lasts approximately 1.7 μs therefore the peak electrical power absorbed during this time is 3.01×10^4 W. Since the firing frequency of the flash tube is 160 Hz the average consumed power is 8.19 W.

The horizontal radiation pattern in a plane perpendicular to the arc, lying half-way between the two electrodes is illustrated by a dotted line in Figure 3.10. It is characterized by shadow zones caused by the supporting structure of the electrodes inside the flashtube. The vertical radiation pattern of the xenon arc, represented by a dotted line in Figure 3.11, shows that a substantial portion of the energy is radiated outside the ± 150 mrad vertical angle which was specified as a design objective.

Reflective and refractive methods of eliminating the shadow

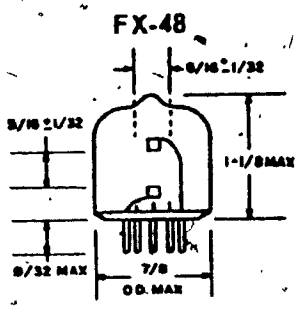

Figure 3.8 Schematic of xenon flashtube.

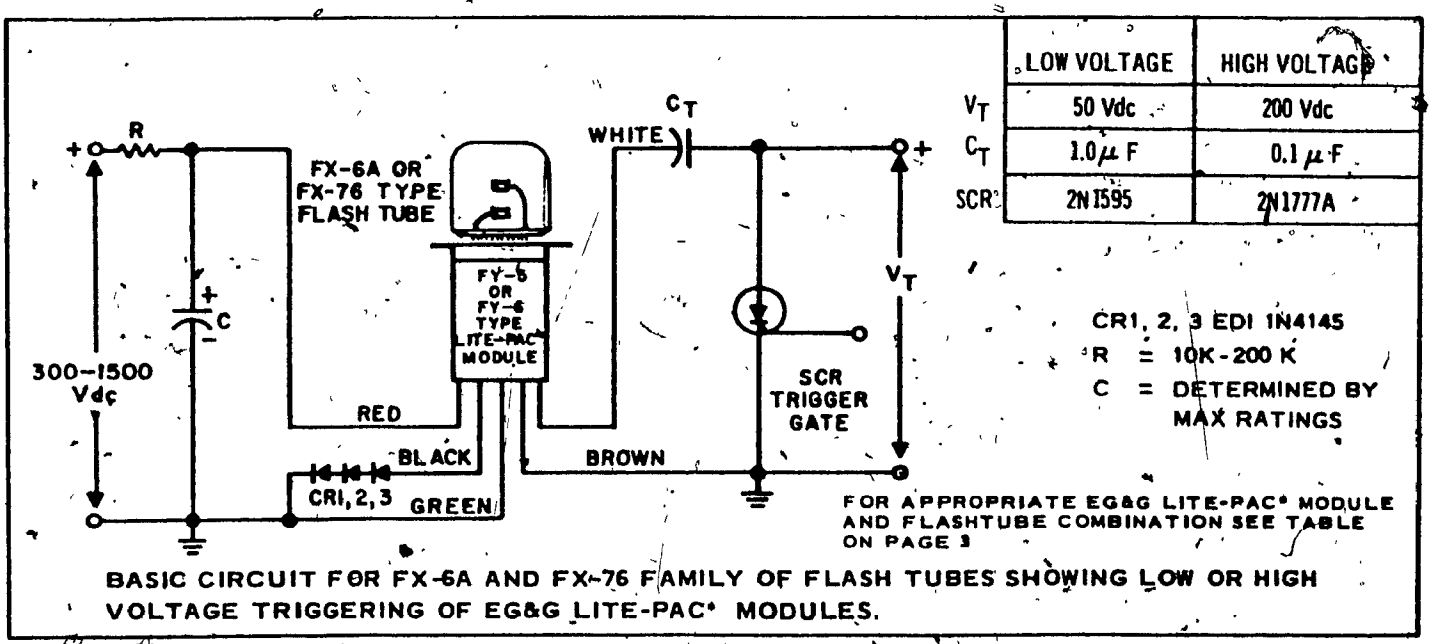

Figure 3.9 Drive circuit for xenon flashtube.

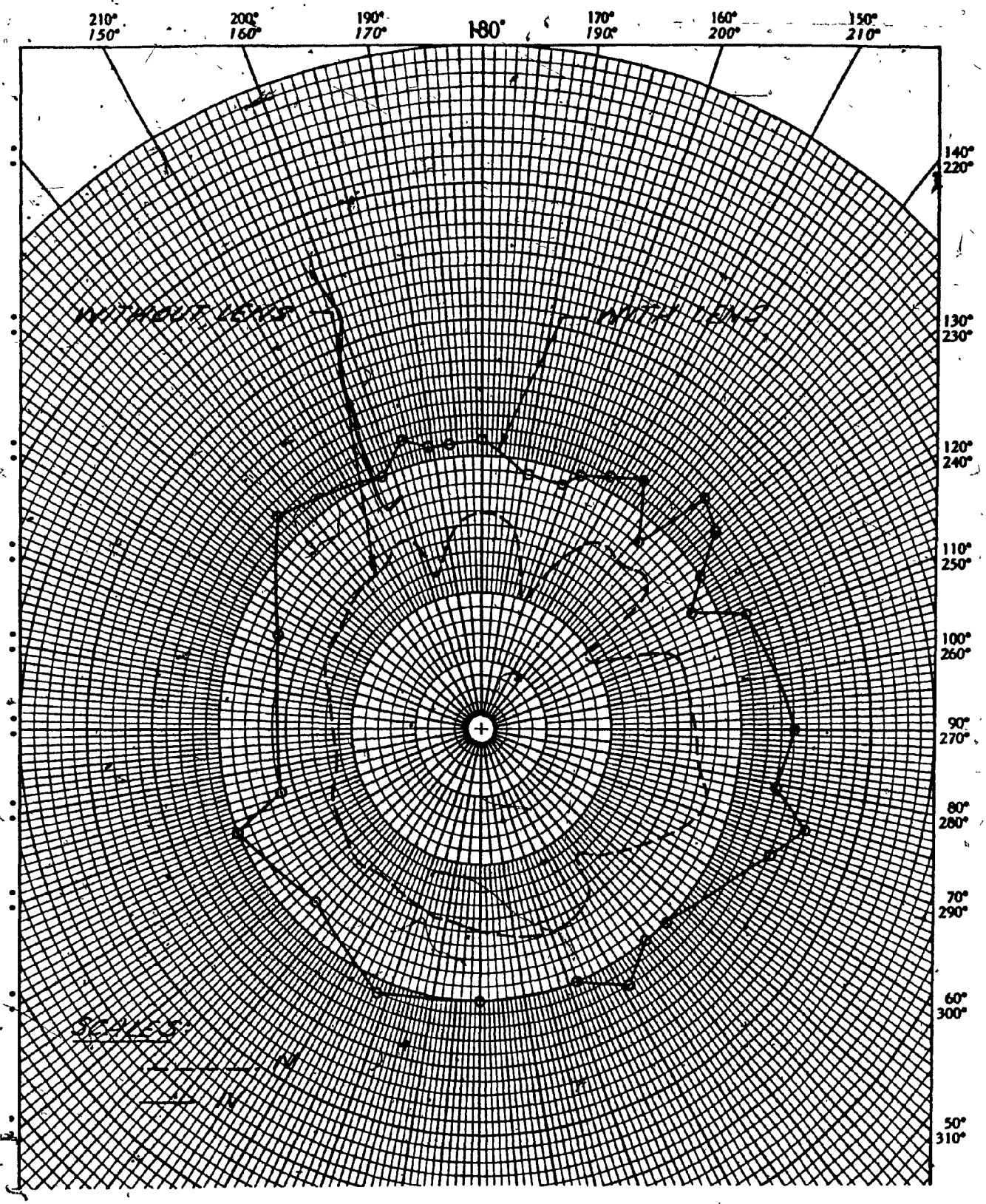

Figure 3.10 Horizontal radiation pattern of xenon flashtube

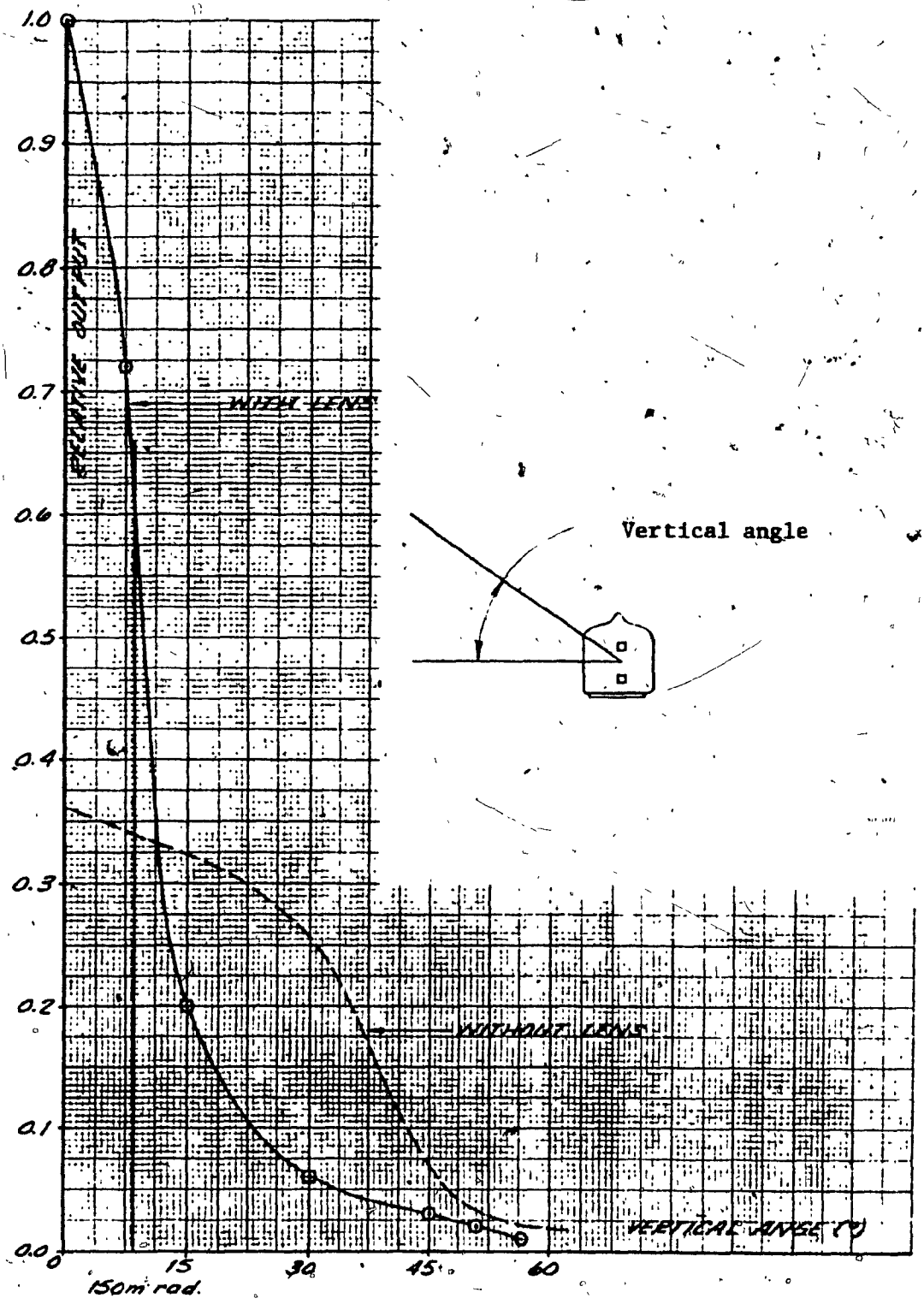

Figure 3.11 Vertical radiation pattern of xenon flashtube

zones in the horizontal radiation pattern and concentrating the energy within the prescribed vertical radiation angle, were investigated. Best results were achieved with a fluted toroidal lens made of acrylic illustrated in Figure 3.12. A typical ray tracing in the horizontal plane half-way between the two electrodes, shows that the vertical flutes form multiple line images of the xenon arc and that the radiation patterns originating from these sources overlap. Consequently, the shadow zones are considerably reduced and the ratio of maximum to minimum irradiance has been decreased from 1.9 (without lens) to 1.6 (with lens), while the irradiance is increased on the average by a factor of 3.6. These improvements are illustrated by the solid line radiation pattern in Figure 3.10. The effect of the lens on the vertical radiation is illustrated by the solid line curve in Figure 3.11. It is apparent from this graph that the toroidal lens increases the irradiance in the median plane of the electrodes by a factor of 4.2, and at ± 150 mrad by a factor of 2.1.

The wavelength of the radiation generated by xenon arc lies between 330 nm and [illegible] nm. However, according to the design specification the spectral components in the visible range must be eliminated. In order to meet this requirement a cylindrical low-pass filter with a 715 nm cut-off wavelength was placed between the flash tube and the acrylic lens.

The xenon irradiance was measured by means of a calibrated detector and an oscilloscope at a distance of 2.54 m from the transmitter and was found to be 4.8×10^{-5} W/cm^2. Since the irradiance varies inversely with the square of the distance, its value at 500 m is

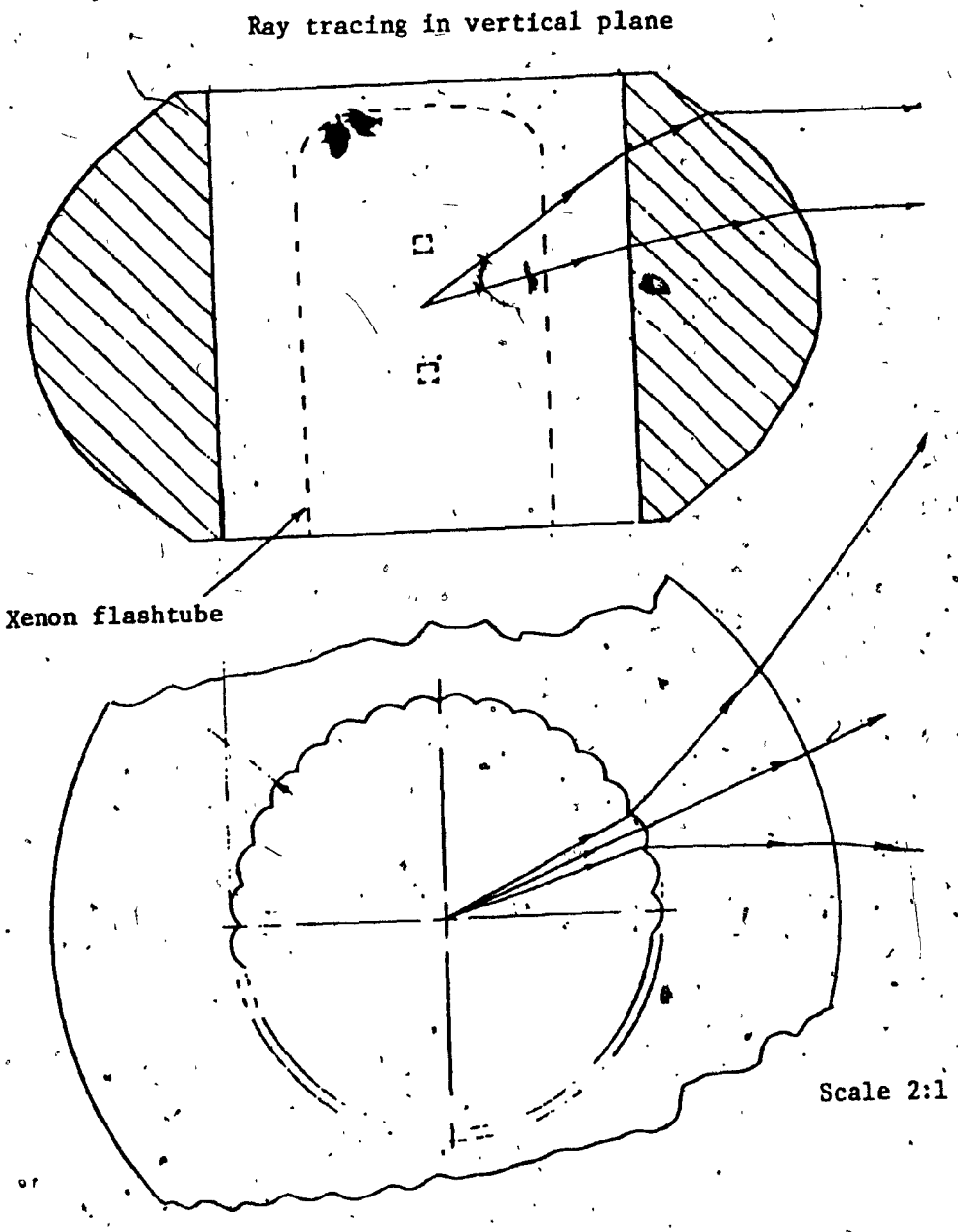

Figure 3.12 Toroidal lens in xenon arc transmitter

$$H_X = 1.23 \times 10^{-5} t_X \quad W/m^2 \qquad (3.7)$$

where t_X is the atmospheric transmittance of xenon radiation over a distance of 500 m. The atmospheric attenuation affecting xenon radiation is comparable to that affecting laser radiation and consequently its value according to [8, p. 252] is also about 85%. Thus $t_X = 0.85$ and the xenon irradiance (omitting the effect of scintillation) is

$$H_X = 1.05 \times 10^{-5} \quad W/m^2. \qquad (3.8)$$

3.4 Receiver

The infrared receiver consists of a convex lens, a photodiode and an amplifier; it can be used in conjunction with either transmitter. The two-element convex lens, corrected for spherical aberration has a focal length of 10 cm and a diameter of 3.0 cm (see Figure 3.13). A p type photodiode positioned in the focal plane of the lens is also shown in Figure 3.13. Its length of 2.90 cm subtends a vertical acceptance angle of 2 arctan (1.45/10) = 300 mrad, while its width of 0.040 cm subtends a horizontal acceptance angle of 2 arctan (0.02/10) = 4.0 mrad. The fully depleted p type silicon photodiode is reverse biased by a 80 V DC power supply (see Figure 3.14a). Under these conditions the device acts as a current source whose output is proportional to the radiant power focussed on its active area and its equivalent circuit is shown in Figure 3.14b. Its performance is defined by its responsivity of 0.60 A/W at 904 nm and its frequency response which depends on the time constant $C_d R$, where C_d is the junction capacitance of the device and R the externally connected load resistor. The load resistor for the laser and xenon channels is

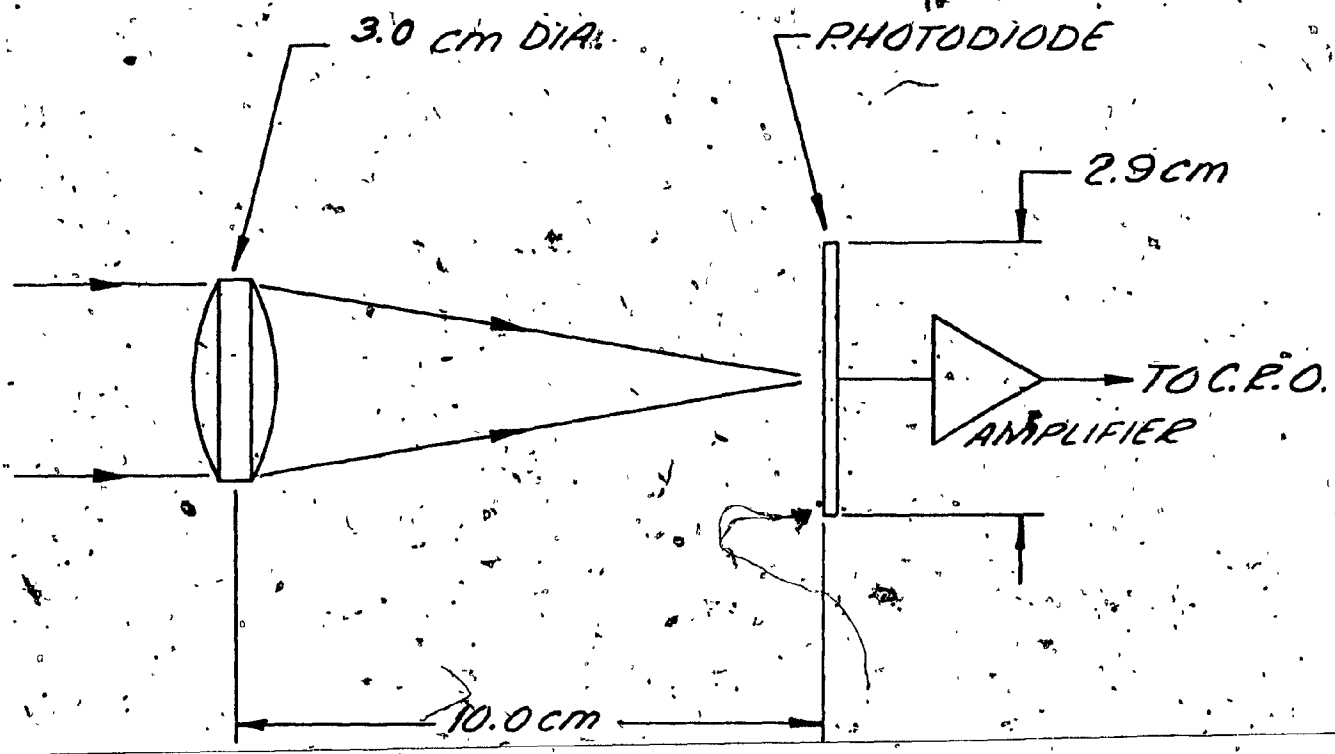

Figure 3.13 Schematic of infrared receiver.

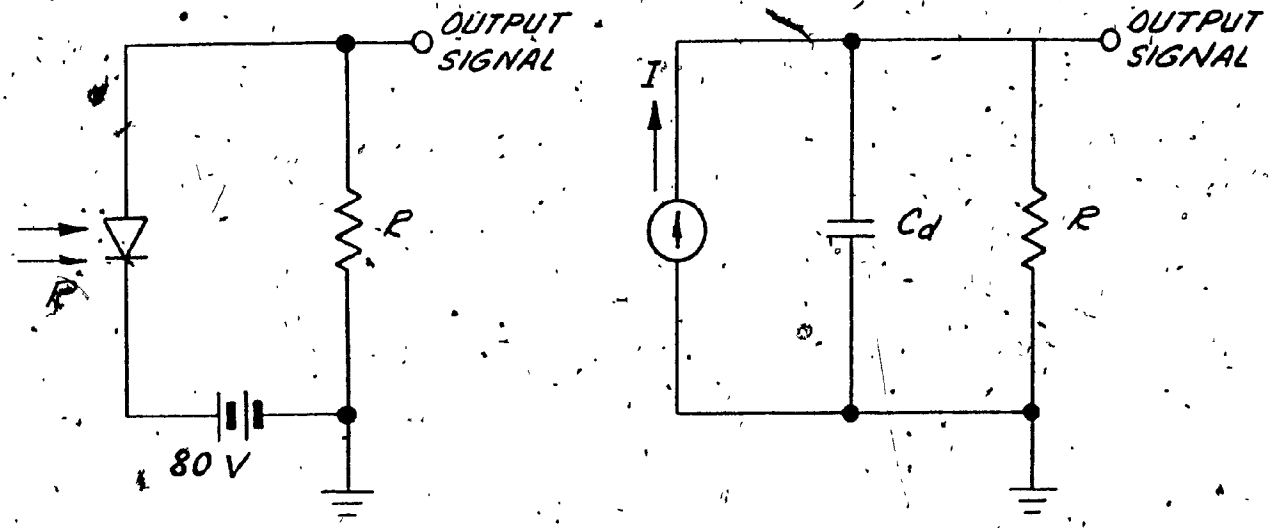

SILICON PHOTODIODE CIRCUIT (a)

EQUIVALENT CIRCUIT (b)

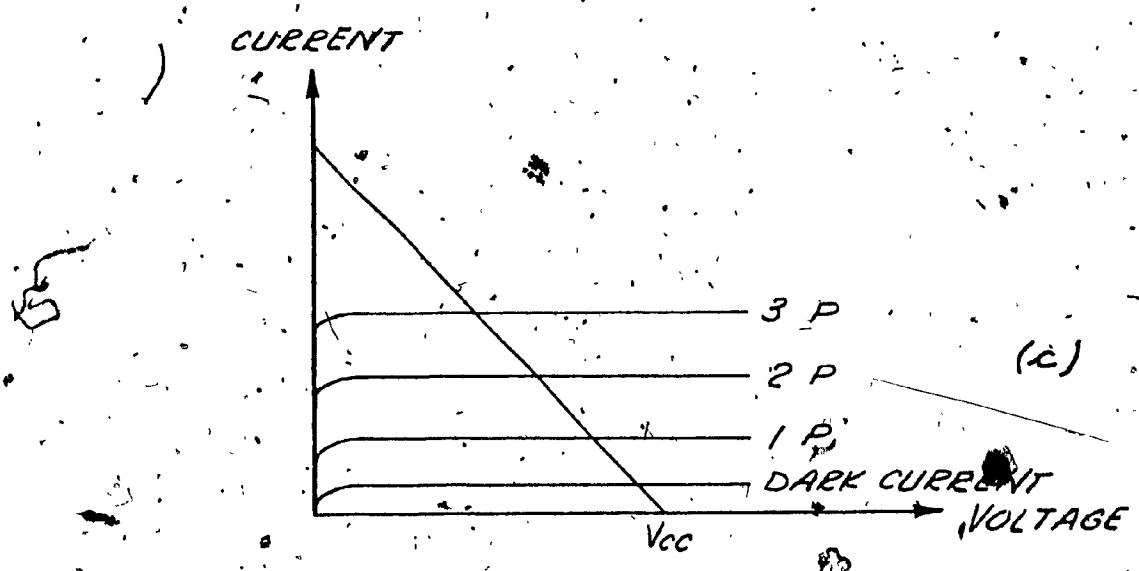

Figure 3.14 Typical characteristic curves of reverse biased silicon photodiode.

selected by comparing calculated and measured voltages across its terminals as a function of its resistance. Assuming that the radiant power laser and xenon inputs to the receiver are square pulses and providing distortion can be tolerated in the shape of the output pulses, the lower limit of the load resistance is defined by the inequality [8]

$$RC_d \geq \tau \qquad (3.9)$$

where τ is the pulse duration. For laser pulses τ_L = 40 ns and therefore $R_L \geq 2$ kΩ while for xenon pulses τ_X = 1.7 μs and consequently $R_X \geq 85$ kΩ.

The theoretical output voltage of the laser channel for an arbitrary load resistance is derived in the Appendix and plotted in Figure 3.15 (dotted line). The measured output voltage in Figure 3.15 (solid line) is shown for comparison. Since the receiver lens focusses the radiant power input within a 0.1 mm diameter spot, a 10% transmittance neutral density filter was used as an attenuator in the receiver in order to protect the active area of the photodiode from excessive radiant power densities. Its effect on the comparison between theoretical and experimental output voltage vs. load resistance variations is discussed in the Appendix. It can be seen in Figure 3.15 that although the ordinates of the theoretical data are lower than the ordinates of measured results the rate-of-change of output voltage vs. load resistance is similar. Bearing in mind that $R_L \geq 2$ kΩ and that the Johnson noise increases with load resistance, a relatively low value of R_L = 3.3 kΩ was selected. The theoretical output voltage variations of the xenon channel for an arbitrary load resistance is also derived in the Appendix and plotted in Figure 3.16 (dotted line). The measured results in Figure 3.16 (solid line) are shown for comparison. A 270 kΩ

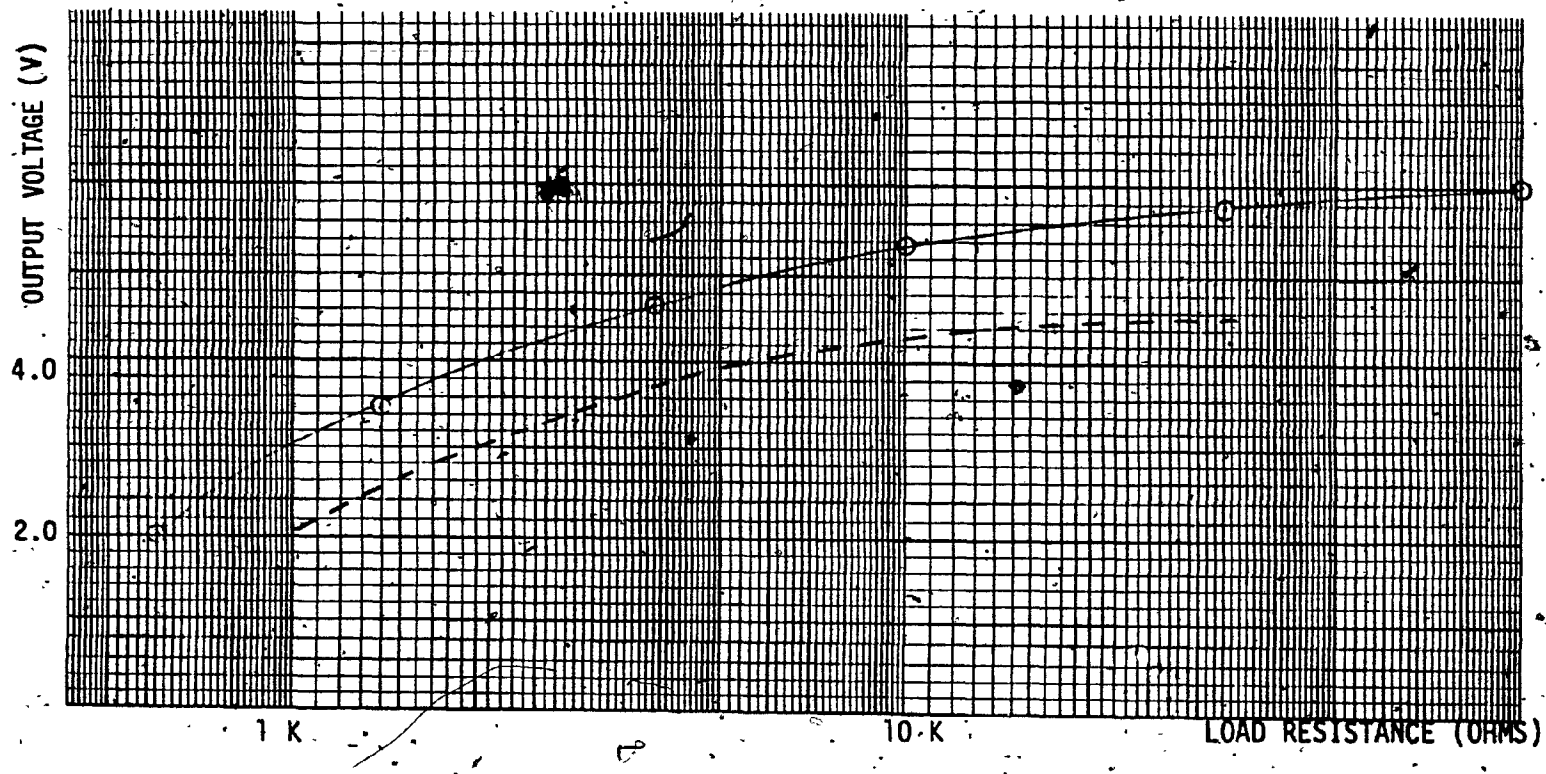

Figure 3.15 Laser channel, theoretical (dotted line) and experimental (solid line) output voltage vs. load resistance.

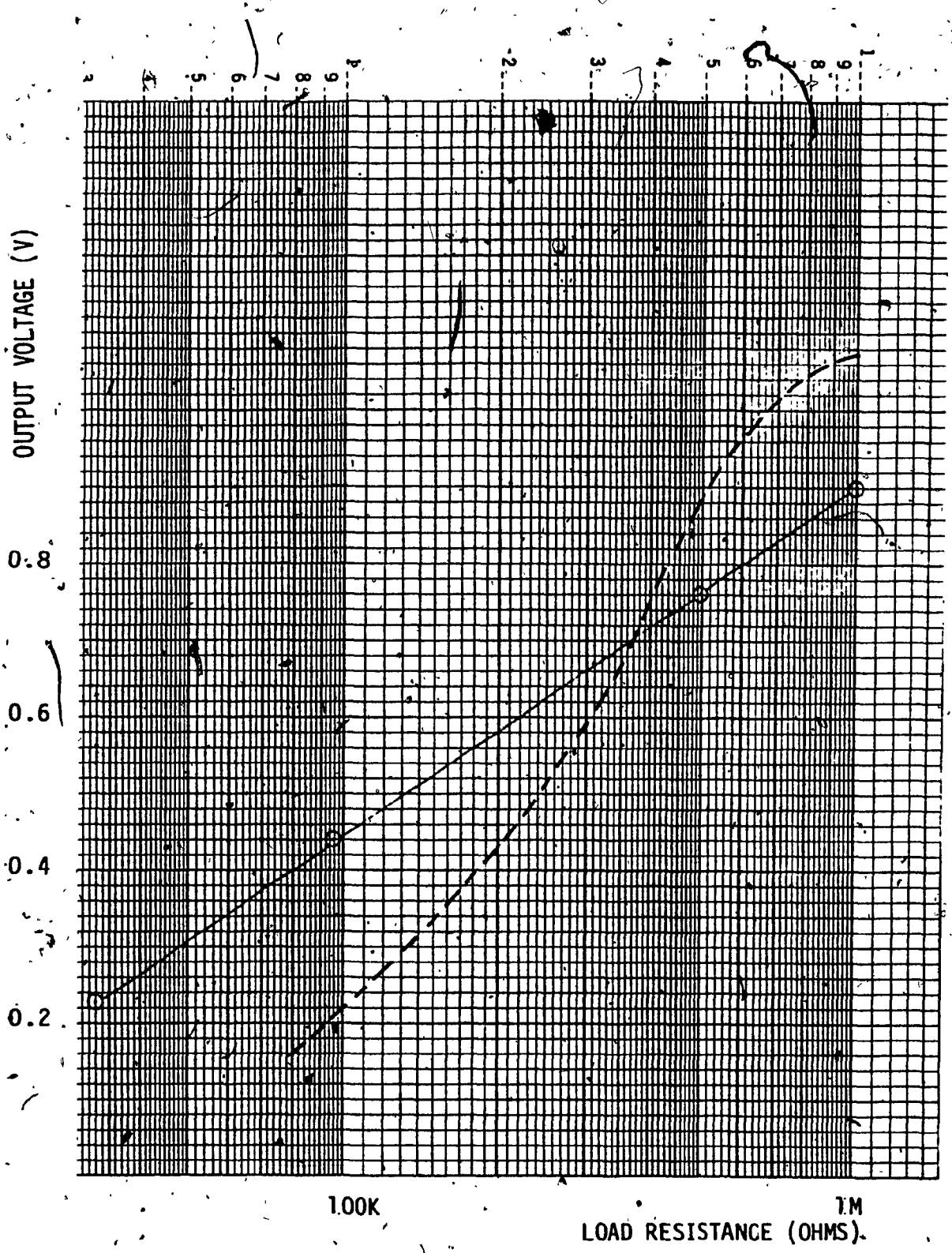

Figure 3.16 Xenon channel, theoretical (dotted line) and experimental (solid line) output voltage vs. load resistance.

load resistor was selected within a range of resistance values where both sets of data are in good agreement.

The amplifier for the photodiode output voltage is illustrated in Figure 3.17. It consists of a field effect transistor (FET) input stage followed by two MC 1590G integrated circuit radio frequency amplifiers manufactured by Motorola. The laser channel amplifier includes the FET stage and one IC stage (see Figure 3.17a); it has a numerical gain of 60. The xenon channel amplifier includes the FET stage and two IC stages (see Figure 3.17b); its numerical gain is 1200. Load resistance values determined previously were used.

3.5 Receiver Output Signal and Signal-to-Noise Ratio

a) Laser Channel

The surface area of the receiver lens is $A_R = 7.07 \times 10^{-4}$ m^2. In Section 3.2 the laser irradiance at 500 m was calculated to be $H_L = 3.20 \times 10^{-2}$ W/m^2. The total laser power P_L focussed on the silicon photodiode is given by

$$P_L = t_R A_R H_L \tag{3.10}$$

where t_R is the optical transmittance of the receiver lens. With $t_R = 0.92$ one obtains the total laser power, $P_L = 2.08 \times 10^{-5}$ W. The receiver signal output e_L across the load resistor R_L is given by the equation

$$e_L = \beta_r P_L R_L \tag{3.11}$$

where β_r, the responsivity of the photodiode, is its ability to generate a current for a given radiant power input. For a type RCA 3005 photodiode $\beta_r = 0.6$ A/W, therefore the receiver output across a load resistance of 3.3 kΩ is $e_L = 41.2$ mV.

Noise is introduced into the laser and xenon communication

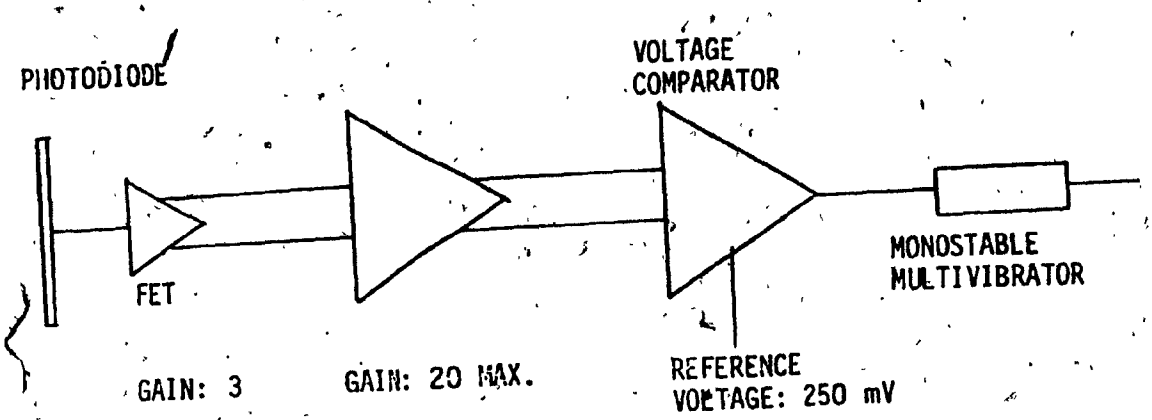

a) LASER CHANNEL

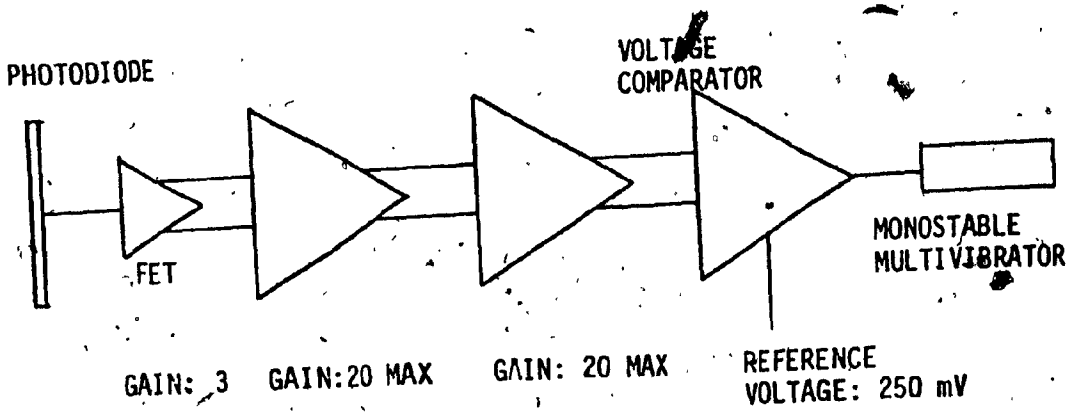

b) XENON CHANNEL

Figure 3.17 Block diagram of infrared receiver.

channels from two sources: the photodiode and the load resistor. Minority carriers moving across a reverse biased p-n silicon photodiode junction have been likened to a stream of small shot and for this reason the unwanted signal they generate is designated shot noise. In the absence of radiant flux the dark current passing through the detector is $I_d = 0.5\ \mu A$. The mean-square value of the shot noise current caused by the dark current is given by

$$\overline{i_s^2} = 2eI_d\Delta f \tag{3.12}$$

where $e = 1.6 \times 10^{-19}$ C is the electronic charge and $\Delta f = 1/\tau$ is the detector bandwidth. In the laser channel $\tau_L = 40$ ns and the detector bandwidth is $\Delta f_L = 25$ MHz. With these numerical values one obtains

$$\overline{i_s^2} = 4.0 \times 10^{-18}\ A^2. \tag{3.13}$$

The Johnson noise in the load resistor R caused by random motions of the electrons and is given by the expression

$$\overline{i_j^2} = 4kT\Delta f/R \tag{3.14}$$

where $k = 1.38 \times 10^{-23}$ J/°K is the Boltzmann constant and $T = 300$ °K is the ambient temperature. Substitution of the above values into (3.14) gives across a load resistance $R_L = 3.3\ k\Omega$

$$\overline{i_j^2} = 1.25 \times 10^{-16}\ A^2 \tag{3.15}$$

The total mean square electrical noise current is $i_n^2 = i_s^2 + i_j^2$ and its root is

$$\sqrt{\overline{i_n^2}} = 1.14 \times 10^{-8}\ A. \tag{3.16}$$

The total r.m.s. noise voltage generated by this current is

$$e_n = R_L\sqrt{\overline{i_n^2}} = 3.76 \times 10^{-5}\ V. \tag{3.17}$$

Since the output from the photodetector stage was calculated to be 42.2 mV the signal-to-noise ratio of the laser communication channel is

$$(S/N)_L = 60.8 \text{ dB}. \tag{3.18}$$

b) Xenon Channel

In Section 3.3 the irradiance from the xenon flash tube at 500 m was calculated to be 1.05×10^{-5} W/m^2. Bearing in mind that the surface area of the lens is 7.07×10^{-4} m^2 the total radiant flux focussed on the active area of the detector will be the product of these i.e. 7.42×10^{-9} W. Taking into account the responsivity of the device and applying (3.11) the output current is calculated to be 4.45×10^{-9} A and the output voltage from the photodetector stage across the load resistor R_X = 270 kΩ is 1.20 mV.

To obtain the signal-to-noise ratio methods used on the laser channel will be applied, except that in this case Δf_X = 590 kHz, since τ_X = 1.7 μs. Therefore, substituting the appropriate numerical values into (3.12) the mean square value of shot noise current is

$$\overline{i_s^2} = 9.44 \times 10^{-20} \text{ A}^2 \tag{3.19}$$

Similarly, (3.14) gives the mean square value of the Johnson noise

$$\overline{i_j^2} = 3.62 \times 10^{-20} \text{ A}^2 \tag{3.20}$$

whence the r.m.s. current using (3.16)

$$\sqrt{\overline{i_n^2}} = 3.61 \times 10^{-10} \text{ A} \tag{3.21}$$

The total r.m.s. voltage generated by this current as calculated from (3.17) is

$$e_n = 9.75 \times 10^{-5} \text{ V} \tag{3.22}$$

Since the output of the photodetector stage is 1.20 mV, the signal to noise ratio $(S/N)_X$ of the xenon communication channel is:

$$(S/N)_X = 24.9 \text{ dB} \qquad (3.23)$$

CHAPTER IV

EXPERIMENTAL RESULTS

4.1 Preliminary Considerations

In Chapter 2.0 the theory of optical transmission through the atmosphere was presented and it was pointed out that the laser and xenon irradiance is subjected to two kinds of attenuation:

a) attenuation caused by molecular absorption, and scattering which is a function of distance only,

b) attenuation caused by variations of the air refractive index which is a function of time, distance, temperature and solar radiance. It manifests itself as an amplitude modulation of the received signal.

When the amplitudes of received signals and signal-to-noise ratios were estimated in Section 3.4 the first type of attenuation only was considered and it was decided to measure the effect of the second type during field tests. In order to separate the two types of attenuation the field tests were conducted in two stages.

Stage 1: The laser and xenon communication links were operated over a short range to avoid the effect of atmospheric turbulence and the effect of distance was simulated by controlled attenuation. The measured laser and xenon channel output signals were compared to those estimated in Section 3.4. These data were used as criteria for evaluating the effect of atmospheric turbulence when the signal path length was extended. Results of these tests are presented in

Section 4.2.

Stage 2: The system was tested at full range and the influence of atmospheric turbulence and sun radiance on signal amplitude was measured. Experimental data gathered during this phase are summarized in Section 4.3.

4.2 Results of Simulation Tests

The transmitter and receiver were set up 50 m apart in a long corridor. Since the signal power varies in inverse proportion to the square of the distance, a neutral density filter with a 1% transmittance was used to simulate a 500 m path. The receiver output was measured with an oscilloscope and a Polaroid camera was used to record the data. A block diagram of the equipment used during the experiments is shown in Figure 4.1.

The laser signals at a simulated distance of 500 m are shown in Figures 4.2a and 4.2b. In Figure 4.2a the sweep rate was adjusted to 0.2 μs/cm to allow the recording of the pulse shape. With a pulse repetition rate of 25.6 kHz and a 0.1 s exposure time the photograph actually displays over 2500 superimposed pulses. The ratio of maximum signal to minimum signal is 1.2. In Figure 4.2b the horizontal scale was changed to 5 ms/cm to display the envelope of the amplitude variations. Since the effect of atmospheric turbulence over a distance of 50 m is negligible it is concluded that the observed variation in amplitude is caused by "laser jitter". This phenomenon is inherent in all laser diodes and according to information supplied by the RCA Electro-Optics Division it is due to variations (up to 10%) in the radiant power amplitude from one pulse to another.

Figure 4.3a and 4.3b show the outputs of the xenon communication

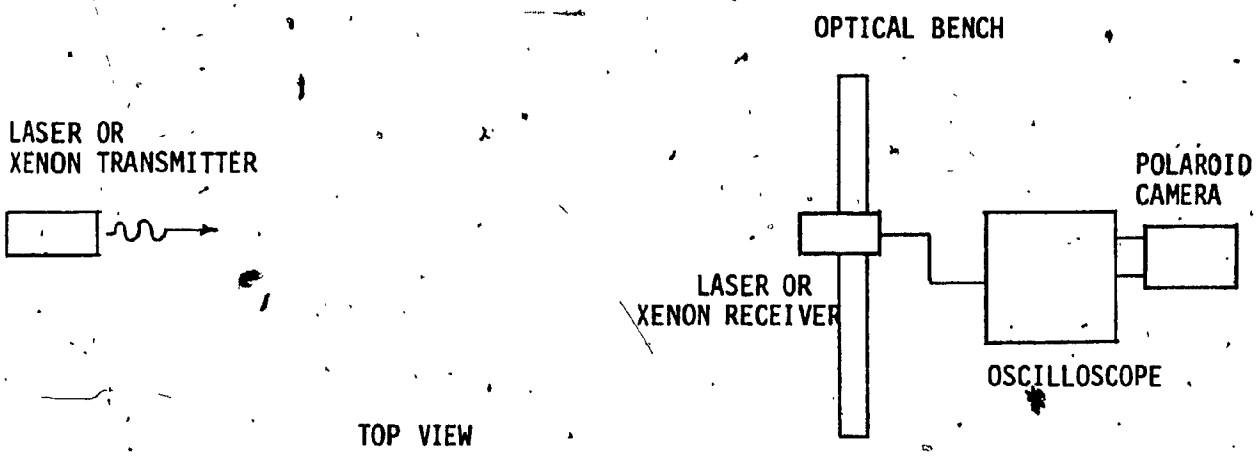

Figure 4.1 Equipment used during simulation and field tests

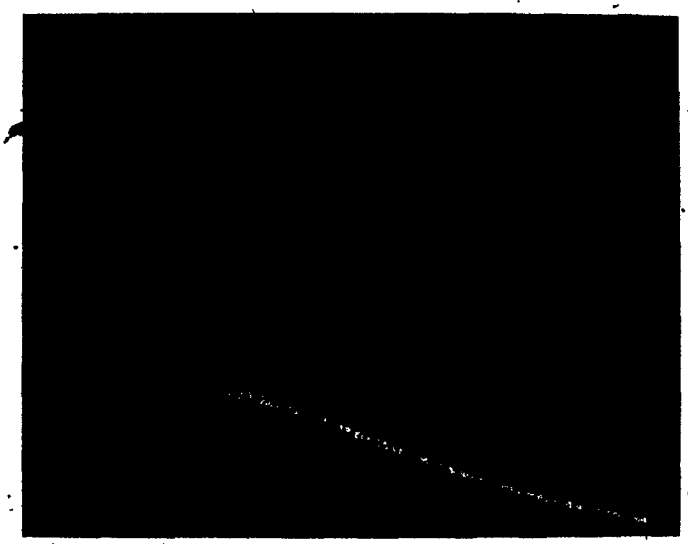

Horizontal Scale
0.2 μs/cm

Vertical Scale
0.5 V/cm

Figure 4.2a Laser signal at 50m, reference setup with 1% transmission neutral density filter

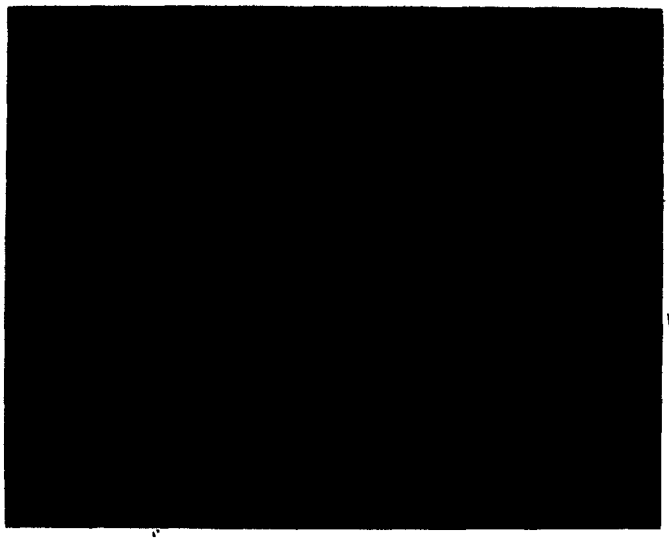

Horizontal Scale
5 ms/cm

Vertical Scale
0.5 V/cm

Figure 4.2b Laser signal at 50m, reference setup with 1% transmission neutral density filter; reference trace dropped by 2 cm

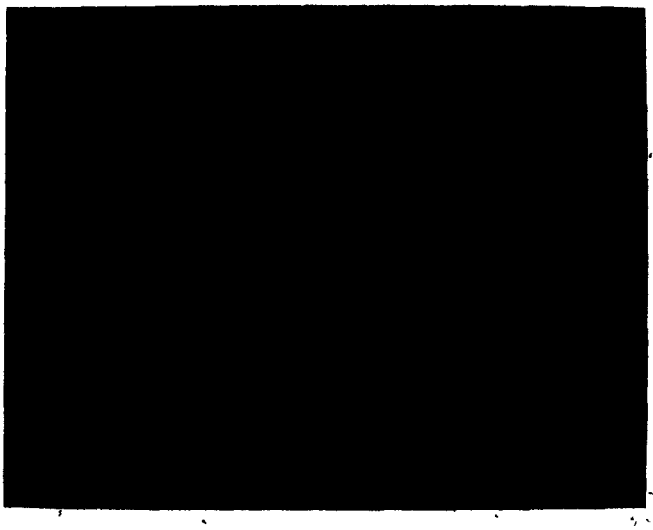

Horizontal Scale
10 μs/cm

Vertical Scale
0.5 V/cm

Figure 4.3a Xenon signal at 50 m, reference setup with 1% transmission neutral density filter.

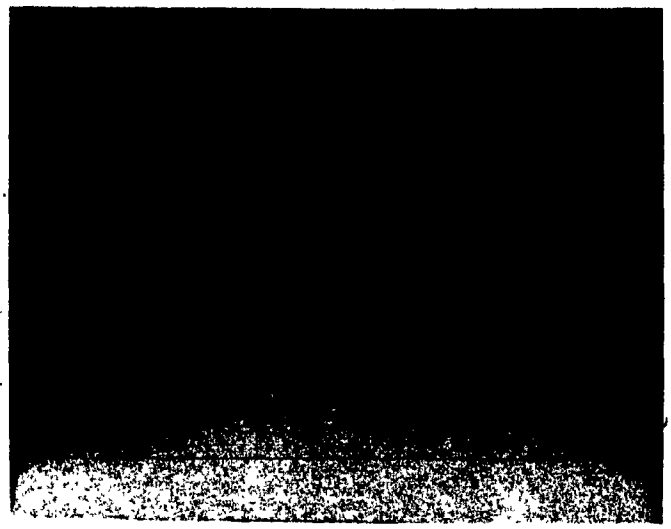

Horizontal Scale
5 ms/cm

Vertical Scale
0.5 V/cm

Figure 4.3b Xenon signal at 50 m, reference setup with 1% transmission neutral density filter.

channel; the pulse repetition frequency in this case is 160 Hz and the horizontal sweep rates are 10 μs/cm and 5ms/cm, respectively. With an exposure time of 0.1 s, Figure 4.3a displays 16 superimposed pulses. The envelope of small signal amplitude variations is displayed in Figure 4.3b, the ratio of maximum to minimum signal amplitude is 1.1. This phenomenon is caused by variations in the radiant power output of xenon flashes (up to ± 5%), according to data supplied by the EG & G Corporation, manufacturer of the device.

4.3 Results of Field Tests

a) Laser channel

The transmitter and receiver were subsequently set up 500 m apart on flat, grassy terrain. The alignment accuracy was verified visually by means of an infrared viewer. The center of the laser beam was found by seeking the maximum intensity of the source image generated by the infrared converter tube. The accuracy of this method was estimated to be within ± 3 cm and at 500 m this corresponds to an angular error of ± 0.06 mrad. This procedure was also used for xenon channel alignment. During these experiments, the infrared receiver mounted on an optical bench was moved perpendicularly to the line-of-sight between the transmitter and the receiver (see Figure 4.1). By displacing the receiver from the position corresponding to the maximum signal, the width of the laser beam at the half-power points was measured and was found to be 0.30 mrad. This result is again in good agreement with the 0.36 mrad width obtained at 50 m, described in Section 3.2 and illustrated in Figure 3.5. These measurements were performed at night when air turbulence is known to be minimal. Signal amplitudes observed on the laser channel are shown in Figures 4.4a and 4.4b. The pulse

Horizontal Scale
0.2 μs/cm

Vertical Scale
0.5 V/cm

Figure 4.4a Laser signal at 500 m; warm, clear night.

Horizontal Scale
5 ms/cm

Vertical Scale -
0.5 V/cm

Figure 4.4b Laser signal at 500 m; warm, clear night.

shape (Figure 4.4a) reveals a considerable amplitude variation and the ratio of maximum to minimum signal is 4.2. Since image dancing and saturation of the photodiode by background radiance were eliminated in Chapter II as possible causes of this amplitude modulation, it is concluded that the observed phenomenon is caused by time variations of the air refractive index which depend on ambient temperature and solar irradiance. Figure 4.4a also shows that the average signal amplitude is in good agreement with results obtained at 50 m with a 1% transmission filter: the average amplitude of the pulse is very close to that obtained under simulated conditions (see Figure 4.2a) minus a 15% decrease in amplitude which was the estimated transmission loss through the atmosphere calculated in (3.3). To further verify the validity of (3.3) the transmitter-receiver distance was changed to 250 m and in order to avoid saturation of the amplifier the incoming signal was attenuated by a 5.95% transmittance filter (see Figure 4.5). Subsequently, the same measurement was repeated at 500 m (see Figure 4.6). Comparison of average signal amplitudes in Figures 4.5 and 4.6 gives a 4:1 amplitude ratio for a 2:1 distance ratio, thus verifying the inverse square law dependency of irradiance on distance.

The envelope of the amplitude variations shown in Figure 4.4b provides data for estimating the highest frequency component of air turbulence: the shortest transient is of the order of 2 ms, hence the highest frequency component in the pulse envelope is approximately 500 Hz.

b) Xenon channel

Figures 4.7a and 4.7b show typical recordings of xenon signals and amplitude variations caused by air turbulence at 500 m. The average

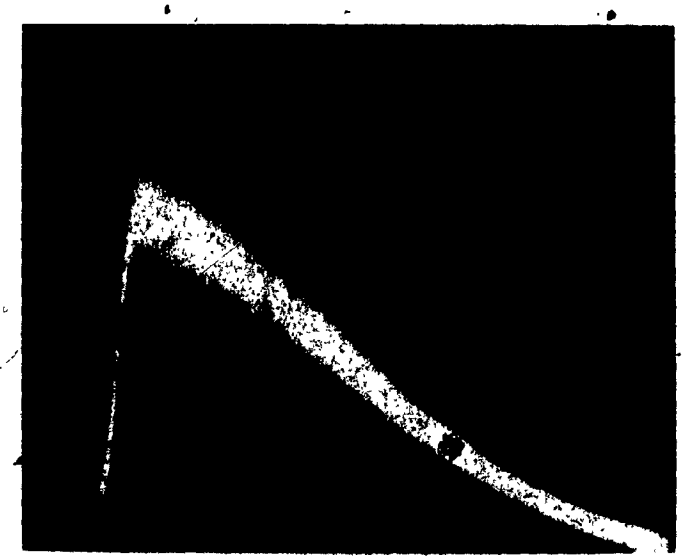

Horizontal Scale
0.2 μs/cm

Vertical Scale
50 mV/cm

Figure 4.5 Laser signal at 250 m; sun, haze, wind
6% transmission neutral density filter.

Horizontal Scale
0.2 ms/cm

Vertical scale
50 mV/cm

Figure 4.6 Laser signal at 500 m; overcast
6% transmission neutral density filter.

Horizontal Scale
0.2 μs/cm

Vertical Scale
0.5 V/cm

Figure 4.7a Xenon signal at 500 m; sunny.

Horizontal Scale
5 ms/cm

Vertical Scale
0.5 V/cm

Figure 4.7b Xenon signal at 500 m; sunny.

values of these signals are in good agreement with those obtained at 50 m with a 1% transmittance neutral density filter (see Figures 4.3a and 4.3b) which simulates the 500 m distance. These measurements verify that the xenon irradiance varies in inverse proportion to the square of the distance according to (3.4). In order to confirm the results obtained with the receiver, irradiance measurements as a function of distance were repeated with the radiometer described in Section 4.5 and the measured data are plotted in Figure 4.8, Curve 1. If the signal e_X is inversely proportional to the square of the distance then

$$e_X = C_1/x^2 \qquad (4.1)$$

where C_1 is a constant. This means that the product of the ordinate by the square of the abscissa is a constant whose dimensions are Vm^2. This product was evaluated at each measured point and its graph as a function of distance is Curve 2. These data are in good agreement with $e_X x^2 = C_1$ for distances up to 300 m. Large deviations (approximately 19%) from the inverse square law were observed at distances of 400 m and 500 m. They were caused by large amplitude variations due to air turbulence in a signal whose approximate amplitude was 20 mV. Under these conditions it was difficult to estimate the average value of the amplitude on the oscilloscope screen.

It was observed during field tests that the scintillation effect was much more pronounced in sunny weather than in cloudy weather. Especially interesting was the sudden transition of the scintillation from very large amplitude variations in bright sun light to considerably smaller variations under cloudy conditions. This effect was so sudden that an experimenter watching the cathode ray tube through a hood could detect the passing of a cloud. It is well known that the refractive

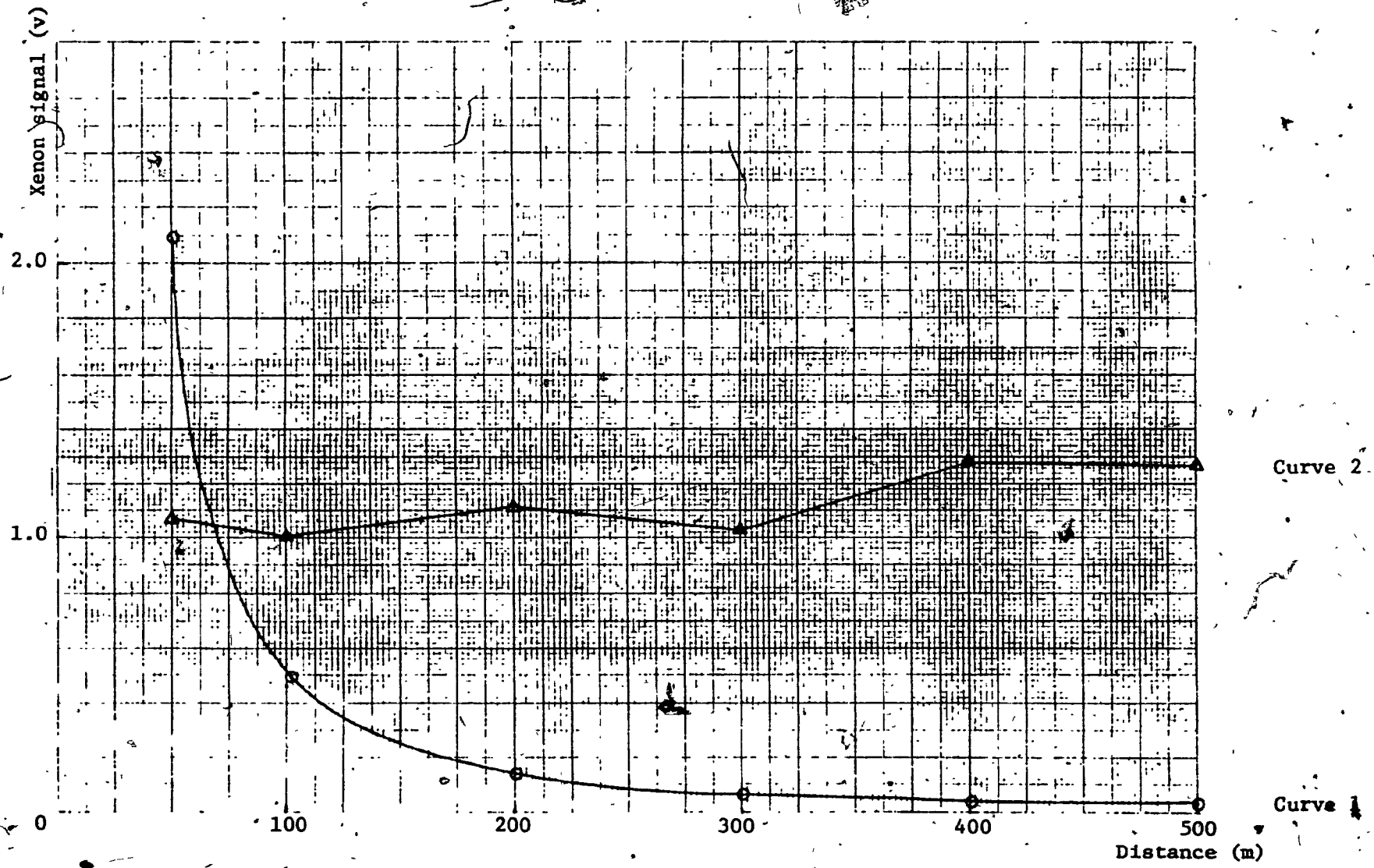

Figure 4.8 Variation of xenon signal as a function of distance (Curve 1); product (distance)^{2}x (signal) as a function of distance (Curve 2)

index of air varies as a function of temperature and therefore it is expected that in sunny weather there would be more air turbulence than in cloudy weather. However, the transition from one scintillation mode to another under conditions of variable cloudiness takes place within a few seconds, much faster than the time required for appreciable temperature changes to take place. This effect has been recorded on the laser (see Figures 4.9a and 4.9b) and xenon communication channel (Figures 4.10a and 4.10b) alike. In the latter case, the horizontal sweep rate was adjusted from 10 μs/cm to 1.0 μs/cm in order to enhance the recordings of amplitude modulation. It is difficult to reconcile the observed phenomenon with the existing theory of scintillation based on the assumption that the dominant cause of refractive index variations is due to ambient temperature fluctuations. An attempted explanation of this phenomenon is briefly outlined in Section 2.6.

The average temperature during the experiments described above was 27°C and the question arose whether or not variable cloudiness would have the same effect on the modulation index at low temperatures. A series of measurements was therefore undertaken at an ambient temperature of 0°C with the same laser transmitter but with an earlier version of the receiver described in Section 3.4. Its first amplification stage was a transistor operating in the common emitter mode rather than a FET. The results are shown in Figures 4.11, 4.12a, 4.12b and 4.13.

Figure 4.11: reference set up at 50 m similar to that described in Section 4.2.

Figures 4.12a and 4.12b: laser signal at 500 m under "full sun" conditions

Figure 4.13: laser signal at 500 m under cloudy conditions

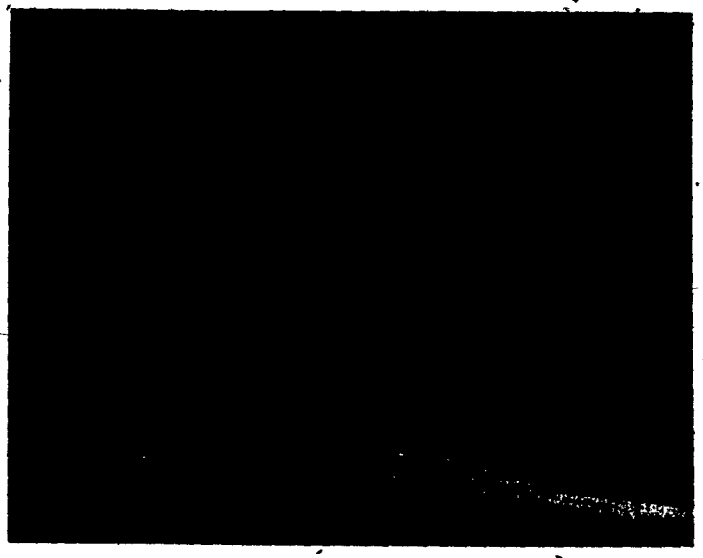

Horizontal Scale
0.2 μs/cm

Vertical Scale
0.5 V/cm

Figure 4.9a Laser signal at 500 m;
sun, haze, wind

Horizontal Scale
0.2 μs/cm

Vertical Scale
0.5 V/cm

Figure 4.9b Laser signal at 500 m;
sun obscured by cloud.
The transition from the scintillation
mode in Figure 4.9a to that in 4.9b
occurred in less than 2s.

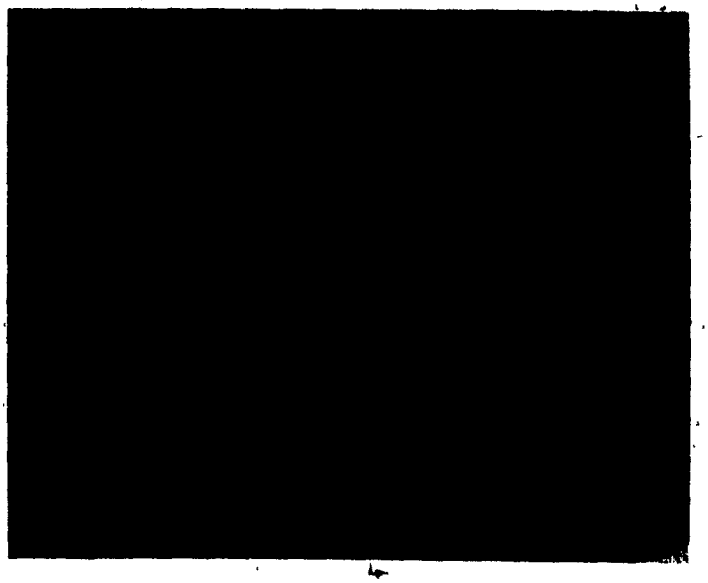

Horizontal Scale
1 μs/cm

Vertical Scale
0.5 V/cm

Figure 4.10a Xenon signal at 400 m; sunny.

Horizontal Scale
1 μs/cm

Vertical Scale
0.5 V/cm

Figure 4.10b Xenon signal at 400 m; sun obscured by cloud. The transition from the scintillation mode in Figure 4.10a to that in Figure 4.10b occurred in less than 2s.

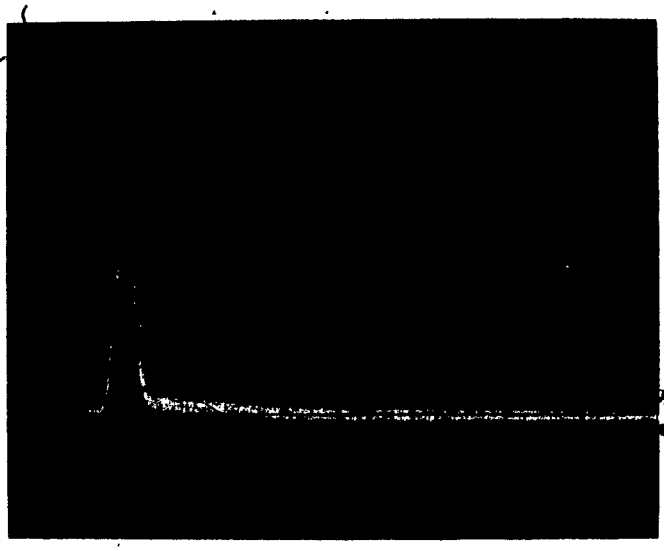

Horizontal Scale
0.2 μs/cm

Vertical Scale
0.2 V/cm

Figure 4.11 Laser signal at 50m; reference setup with 1% transmission neutral density filter.

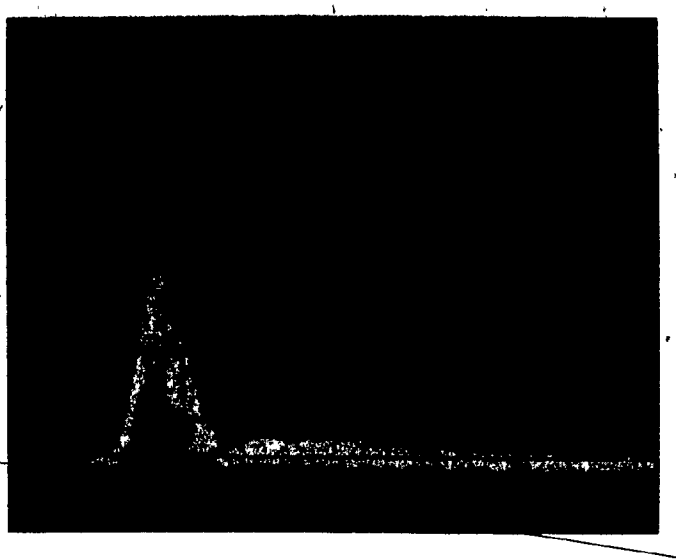

Horizontal Scale
0.1 μs/cm

Vertical Scale
0.2 V/cm

Figure 4.12a Laser signal at 500 m; bright sun, cold.

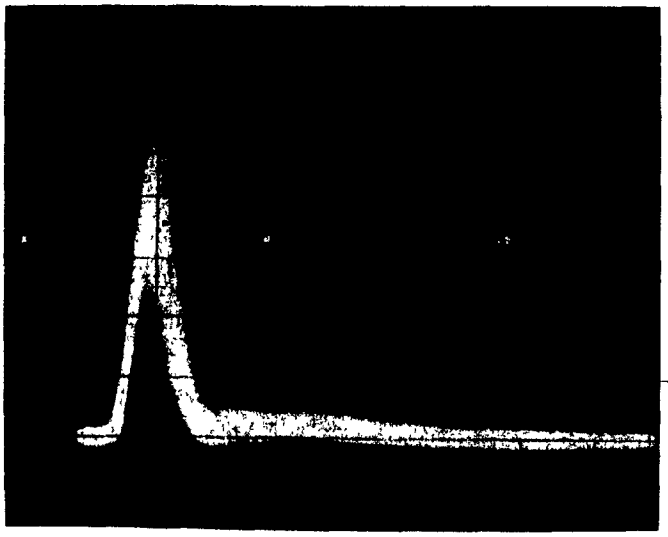

Horizontal Scale
0.1 μs/cm

Vertical Scale
0.2 V/cm

Figure 4.12b Laser signal at 500m; bright sun, cold.

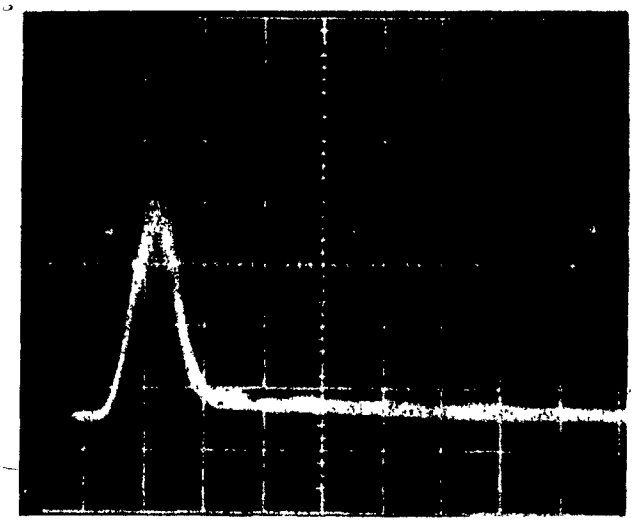

Horizontal Scale
0.1 μs/cm

Vertical Scale
0.2 V/cm

Figure 4.13 Laser signal at 500m; cloudy, cold.

It is apparent from the last three figures that sun radiance also causes a considerable modulation depth of the laser signal at low ambient temperatures.

Following the completion of laser and xenon transmission tests the signal-to-noise ratio on both channels was measured. Background radiance increases the shot noise level in the photodetector circuit by increasing the quiescent current which flows through the sensor. This means that the total estimated noise voltages on the laser and xenon channels should be higher than those calculated in Section 3.4 Consequently the numerical signal-to-noise ratios of 1096 on the laser channel and 17.6 on the xenon channel evaluated in Section 3.4 should have lower values. When the receiver was facing the sky and the terrain a peak-to-peak noise of 100 mV was measured on the laser channel and 200 mV peak-to-peak noise on the xenon channel, in the absence of laser and xenon pulses. When the communication links were operating, the amplitudes of the signal outputs were 2.5 V (laser) and 2.0 V (xenon). Hence the approximate signal-to-noise ratios based on experimental data are 250 and 10, respectively.

4.4 Statistical Analysis of Experimental Results

Following the completion of field tests it was established that providing the effects of atmospheric turbulence are neglected there is fair agreement between the theoretical outputs of the laser and xenon receiver channels, the outputs measured under conditions simulating a transmission distance of 500 m and the outputs measured during field trials over this path length. All results are summarized in Table 4.1.

TABLE 4.1

LASER AND XENON RECEIVER OUTPUT SIGNALS

	Theoretical Output Signals at 500 m (V)	Output Signals Measured Under Conditions Simulating Distance of 500 m (V)	Output Signals Measured at a Distance of 500 m (V)
Laser Receiver	2.47	≈ 3.0	≈ 2.5
Xenon Receiver	2.06	≈ 3.0	≈ 2.0

From the experimental results obtained during the field tests it also became apparent that the effect of air turbulence on the amplitudes of the laser and xenon signals is far greater than that described by Gruss[19]. In order to evaluate the performance of both opto-electronic communication links in the presence of scintillation it was therefore decided to study systematically the amplitude variations as a function of time under different sun radiance conditions and to determine the error rates on both channels. The envelope of amplitude variations observed at the laser channel output were recorded on 56 photographs during variable solar radiance conditions. The same measurements were repeated at the output of the xenon channel and recorded on 13 photographs. Since an opto-electronic scanner was not available, the amplitudes of laser signals were measured at 1 mm intervals and all results were recorded on perforated tape. The amplitudes of the xenon pulses were measured individually and the results recorded in a similar fashion. A computer program whose flow chart is shown in Figure 4.14 was prepared and a sample of the calculated results is shown in Figure

S1 Open file to be studied

S2 Initialize variables and print name of file and titles

S3 Compute average value of samples $\bar{A} = (N)^{-1} \sum_{i=1}^{N} A_i$

S4 Sort out samples in windows of 0.1V to produce HISTOGRAM

S5 Compute probability Z_1 of losing signal

Z_1 = (number of samples with $A_i < V_{ref}$)/(total number of samples)

S6 Compute variance of samples about average value determined in S3

$$V_1 = \sum_{i=1}^{N} (A_i - \bar{A})^2/(N-1)$$

S7 Compute square of modulation index $M_1^2 = V_1/\bar{A}^2$

S8 Compute steps S6 and S7 using a calibration value of $\bar{A}_{ref}$ as the average

S9 Print table of results: number of samples, averages $\bar{A}$ and $\bar{A}_{ref}$, standard deviations V and V_{ref}, squares of modulation indices M_1^2 and M_2^2

S10 Print the histogram computed in step S4

S11 Translate histogram into cumulative distribution function

S12 Print cumulative distribution function for increasing steps of 0.1V

S13 Proceed to step S1 for another file

Figure 4.14 Flow Chart Of Computer Program for the Analysis of Scintillation

4.15. It contains the following information:

1. the number of the analysed photograph
2. the number of samples on the photograph
3. the average value of the output voltage on each photograph (AVER.1),
4. the variance of the measured results with respect to this average (VAR.1),
5. σ^2 with respect to this average (MOD.1).
6. the reference average (REF). During simulation tests described in Section 4.2 laser and xenon radiations were attenuated by a 1% transmittance neutral density filter to simulate at 50 m a decrease in signal level equivalent to a range of 500 m. The laser and xenon signals obtained under these conditions are defined as reference averages.
7. the variance with respect to the reference average (VAR.2),
8. σ^2 with respect to the reference average (MOD.2),
9. the probability that the signal will be less than 250 mV,
10. the histogram of pulse amplitudes,
11. the cumulative distribution function of pulse amplitudes.

The probability that the signal will be less than 250 mV defines the transmission reliability of the opto-electronic communication link. If the amplitude of the received laser or xenon signal exceeds this level it triggers a monostable multivibrator which generates a 3.0 V pulse which lasts 15 µs. The probability of the received signal being less than this value can therefore be deduced from the cumulative distribution function which describes the stochastic process of irradiance variations as a function of air turbulence. This quantity

THE PHOTOGRAPHY ANALYSED IS JF182

SAMPLES	AVER.1	VAR.1	MOD.1	REF	VAR.2	MOD.2
71	.963	.338	.123	.674	.446	.437

THERE IS A 30.7859 % CHANCE OF LOSING THE SIGNAL

********** HISTOGRAM OF JF182 **********

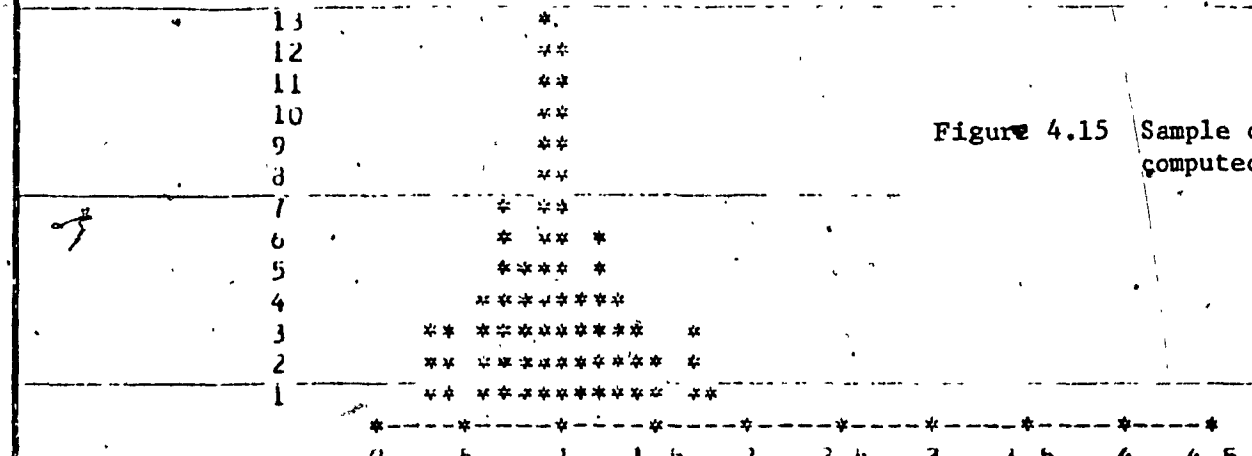

Figure 4.15 Sample of computed results

********** CUMULATIVE DISTRIBUTION FUNCTION **********

WINDOW NO.	UPPER LIMIT (VOLTS)	CUMUL. DISTR. FUNCT. (%)
1	.05	.00
2	.15	.00
3	.25	.00
4	.35	4.23
5	.45	8.45
6	.55	8.45
7	.65	14.08
8	.75	23.94
9	.85	30.99
10	.95	50.70
11	1.05	67.61
12	1.15	73.24
13	1.25	81.69
14	1.35	87.32
15	1.45	91.55
16	1.55	94.37
17	1.65	94.37
18	1.75	98.59
19	1.85	100.00

****

then becomes a measure of the transmission failure. It should be pointed out that although all the computations are based on voltages, the conclusions can be applied to irradiance measurements, because the relationship between the two quantities is linear.

It was mentioned in Section 4.3 that under conditions of intermittent cloudiness, the amplitude variations of the laser and xenon signals were much larger in bright sunlight than under partial cloud cover. In order to correlate these observations with data obtained by means of a digital computer, Tables 4.2 and 4.3 were prepared. They include the following information:

1. photograph number,
2. σ^2 and σ_T^2 evaluated from (2.82)
3. error rate; this quantity was obtained from the computer printouts by dividing the number of sampled amplitudes below 250 mV by the total number of samples,
4. the effective width b of the photodetector in mm; according to the analysis in Section 2.4 image dancing causes no variation of the signal amplitude. To verify this experimentally the effective width of the photodetector was varied during field tests by masking slits of different widths.
5. the ambient sun radiance affecting each photographer is graded as follows:
   - full sun (F.S.)
   - almost full sun (A.F.S) when the solar disc was barely obscured by a few cloud wisps,
   - partial sun (P.S.) when the solar disc was intermittently visible through the cloud cover or when it was completely

obscured by it.

The interpretation of test results summarized in Tables 4.2 and 4.3 is presented in Chapter V and includes a study of transmission error rate as a function of modulation index on the laser and xenon channels, a discussion on the cumulative distribution function of irradiance as well as the effect of solar radiation on the modulation index and the air refractive index.

TABLE 4.2

LASER TRANSMISSION
SUMMARY OF TEST RESULTS

PHOTOGRAPH NO.	σ^2	σ_T^2	ERROR RATE %	b (mm)	AMBIENT SUN IRRADIANCE
2-1	0.094	0.090	0	2.50	P.S.
2-2	0.033	0.032	6.1	2.50	P.S.
2-4	0.069	0.067	0	1.78	P.S.
2-5	0.062	0.060	0	1.78	P.S.
2-6	0.056	0.054	0	1.78	P.S.
2-7	0.498	0.404	26.5	0.46	F.S.
2-8	0.202	0.184	5.5	0.46	P.S.
3-1	0.149	0.139	0	2.50	P.S.
3-2	0.120	0.113	0	2.50	P.S.
3-3	0.091	0.087	0	2.50	P.S.
3-4	0.211	0.191	0	2.50	P.S.
3-5	0.158	0.147	0	2.50	P.S.
3-6	0.227	0.205	0	2.50	P.S.
3-7	0.139	0.130	0	2.50	P.S.
3-8	0.160	0.148	0	2.50	P.S.
4-1	0.495	0.402	14.0	0.46	A.F.S.
4-2	0.072	0.070	0	0.46	P.S.
4-3	0.121	0.114	0	0.46	A.F.S.
4-4	0.143	0.134	0	0.46	F.S.
4-5	0.355	0.304	5.4	0.46	F.S.
4-6	0.307	0.268	1.3	0.46	F.S.
4-7	0.276	0.244	2.7	0.46	P.S.
5-1	0.346	0.297	3.7	0.46	P.S.
5-2	0.234	0.212	4.4	0.46	P.S.
5-3	0.237	0.213	1.4	0.46	A.F.S.
5-4	0.401	0.337	5.6	0.46	P.S.
5-5	0.275	0.243	0	0.46	P.S.
5-6	0.276	0.244	0	0.46	A.F.S.
5-7	0.476	0.389	17.4	0.46	A.F.S.
7-1	0.999	0.693	23.9	2.50	F.S.
7-2	0.656	0.504	15.6	2.50	F.S.
7-3	0.253	0.226	1.6	2.50	F.S.
7-4	0.518	0.417	17.4	2.50	F.S.
7-5	0.353	0.302	3.8	2.50	F.S.
8-1	0.188	0.172	0.0	2.50	P.S.
8-2	0.332	0.287	4.3	2.50	F.S.
8-3	0.659	0.506	16.4	2.50	F.S.

TABLE 4.2 (cont'd)

LASER TRANSMISSION
SUMMARY OF TEST RESULTS

PHOTOGRAPH NO.	σ^2	σ_T^2	ERROR RATE %	b (mm)	AMBIENT SUN IRRADIANCE
9-1	0.806	0.591	28.0	0.46	F.S.
9-2	0.450	0.372	6.4	0.46	F.S.
9-3	0.632	0.490	15.9	0.46	F.S.
9-4	1.686	0.988	88.9	0.46	F.S.
10-1	0.323	0.280	15.1	0.46	F.S.
10-2	1.191	0.784	48.2	0.46	F.S.
10-3	0.653	0.503	28.8	0.46	F.S.
10-4	0.230	0.207	1.5	0.46	F.S.
11-1	0.269	0.238	4.1	0.46	F.S.
11-2	0.338	0.291	10.1	0.46	F.S.
11-3	0.509	0.411	18.1	0.46	F.S.
11-4	0.258	0.230	0	0.46	F.S.
16-1	0.691	0.525	28.3	0.46	F.S.
24-1	0.651	0.501	13.9	0.46	F.S.
24-2	0.722	0.543	12.1	0.46	F.S.
25-1	0.342	0.294	15.3	0.46	F.S.
25-2	0.322	0.279	9.1	0.46	F.S.
25-3	0.503	0.407	6.4	0.46	F.S.
25-4	0.386	0.326	3.3	0.46	F.S.

TABLE 4.3

XENON ARC TRANSMISSION SYSTEM
SUMMARY OF TEST RESULTS

PHOTOGRAPH NO.	σ^2	σ_T^2	ERROR RATE %	b (mm)	AMBIENT SUN IRRADIANCE
12-1	0.869	0.625	24.0	2.50	F.S.
12-2	0.574	0.454	21.3	2.50	F.S.
12-3	0.745	0.557	15.6	2.50	F.S.
12-4	0.654	0.504	18.4	2.50	F.S.
15-1	0.535	0.426	6.0	1.00	F.S.
15-2	0.591	0.464	3.8	1.00	F.S.
15-3	0.575	0.454	5.0	1.00	F.S.
18-2	0.123	0.116	0	1.00	P.S.
18-3	0.180	0.166	2.9	1.00	P.S.
22-1	0.083	0.080	0	1.00	P.S.
22-2	0.070	0.068	0	1.00	P.S.
22-3	0.259	0.230	8.7	1.00	P.S.
23-1	0.058	0.056	0	1.00	P.S.

4.5 Measurement of Background Radiance

Based on the numerical value of background radiance from reference [8] it was established in Section 2.3 that the DC current in the silicon photodiode generated by ambient radiation could not drive this device into saturation and cause large signal amplitude variations on the laser and xenon channels. The purpose of background radiance measurement is to verify the validity of the quantity used in these calculations and to see whether or not it is affected by variations of the air refractive index. Since these variations cause amplitude modulation of laser and xenon signals they should also influence the intensity of background radiance which consists of solar radiation subjected to Rayleigh and Mie scattering, as well as to reflection and refraction caused by air pockets of varying refractive index and reflection from the ground. It is therefore plausible to predict that if a sensitive radiometer were used to measure background radiance it should reveal the existence of a steady state component and a variable component caused by time variations of the air refractive index. Furthermore, the frequency of these variations is expected to be in the same range as that measured on the laser and xenon channels and discussed previously.

To verify this hypothesis a radiometer illustrated in Figure 4.16 was designed and built. It is equipped with a .32 mm diameter lens whose focal length is 100 mm. At its focus is a calibrated photodiode (United Detector Technology type PLIN-10) with a responsivity of 0.4 A/W. The detector operates in the reverse bias mode and the value of the load resistor is 10 kΩ. Two amplifier stages are connected in parallel across the load resistor: an AC coupled operational amplifier with a gain of

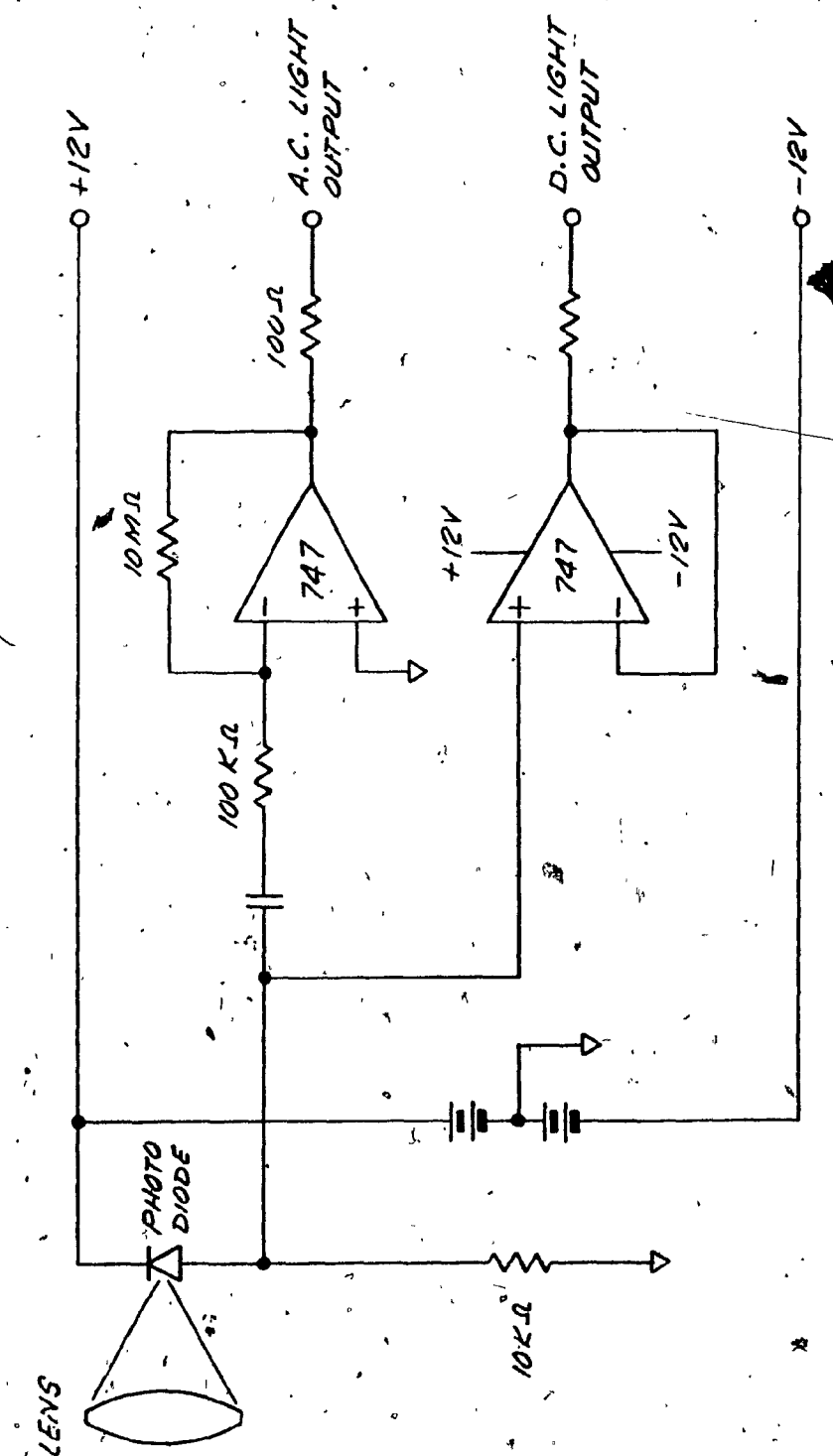

Figure 4.16 Schematic of radiometer

100 and a DC coupled operational amplifier with a gain of 1. Their outputs are connected to a double beam oscilloscope. An infrared filter installed in front of the receiver lens rejects all radiation below 715 nm. The pass-band of the radiometer is approximately 200 nm. Since the area of the calibrated detector is 1 cm^2 and the focal length of the receiver lens equal to 10 cm, the solid angle defined by the optical system is 0.01 sr.

A series of tests has been conducted with the radiometer over terrain used during previous experiments under conditions of intermediate cloudiness and the existence of a steady state and a time-varying component of background radiance was confirmed. The instrument was first calibrated by blocking the radiant flux input to the receiver lens. The DC level was established 4 cm below the top line on the oscilloscope screen as shown in Figure 4.17. The position of the AC level on this photograph is arbitrary. Prior to making radiance measurements it was adjusted to the central reference line on the oscilloscope screen. First a set of measurements was made with the radiometer levelled facing the horizon in the absence of clouds (see Figures 4.18a and 4.18b). The DC output increased by 0.66 V while the AC output, which is the analog of the time-varying component of background radiance, exhibits a peak-to-peak variation of 0.040 V. It is important to note that the calibrated detector has a radius of 5.6 mm and therefore subtends a half angle at the center of the lens of 3.2^{o}. Since the radiometer was mounted 1.5 m above ground it was measuring sky as well as ground radiance when levelled. The steady state and the time-varying components of background radiance were determined as follows:

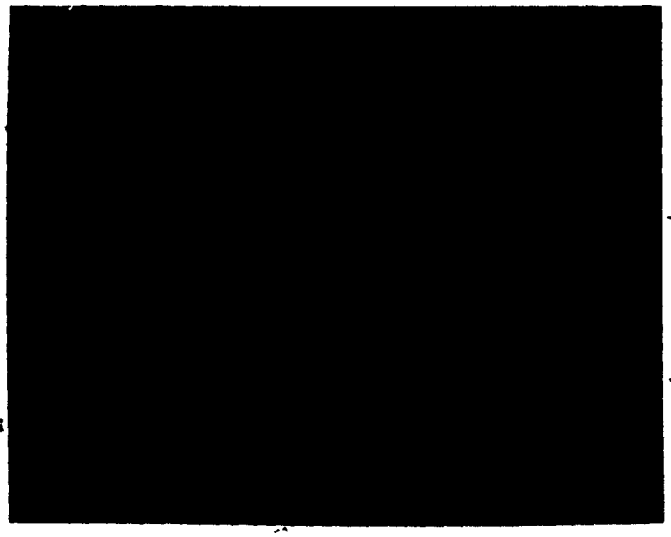

Figure 4.17 Radiometer calibration prior to the measurement of background radiance.

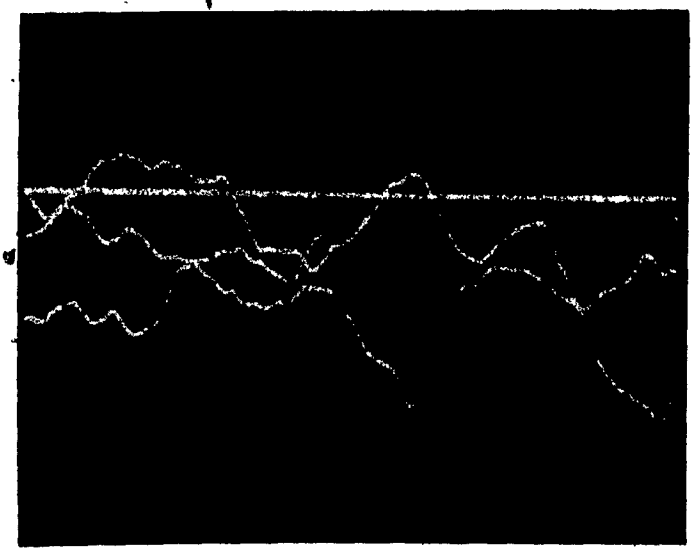

Low frequency component
Horizontal Scale
0.5 s/cm
Vertical Scale
0.2 V/cm

High frequency component
Horizontal Scale
0.5 s/cm
Vertical Scale
0.02 V/cm

Figure 4.18a Background radiance measurement; zenith angle 0°, full sun.

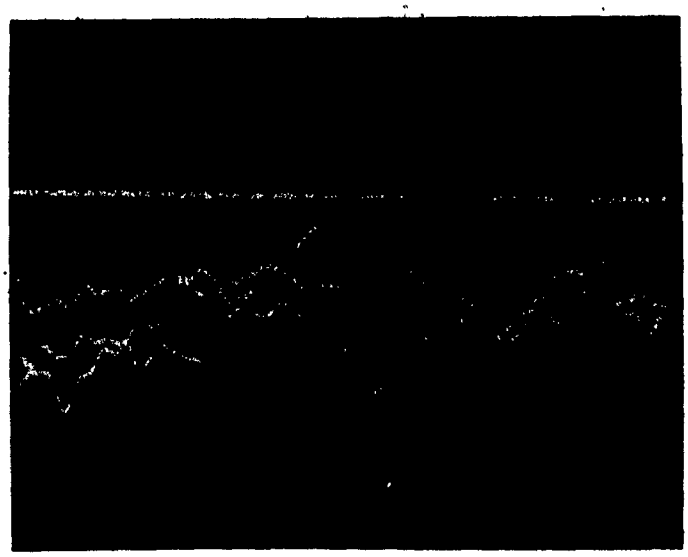

Low frequency component
Horizontal Scale
0.5 s/cm
Vertical Scale
0.2 V/cm

High frequency component
Horizontal Scale
0.5 s/cm
Vertical Scale
0.02 V/cm

Figure 4.18b Background radiance measurement; zenith angle 0°, full sun.

a) Conversion of DC Signal to Steady Component of Background Radiance

With a 10 kΩ load resistor the current through the photodiode is $0.66/10^4 = 6.6 \times 10^{-5}$ A. The responsivity of the photodetector is 0.4 μA/μW hence the total radiant flux input P_{bg} is $6.6 \times 10^{-5}/0.4 =$ 165 μW. The background radiance can be determined from equation

$$N_{bg} = P_{bg}/\Omega_R A_R \Delta\lambda \qquad (4.1)$$

The symbols in this equation were defined in Section 2.3; their numerical values applicable to the radiometer are listed below:

$$\Omega_R = 0.01 \text{ sr}$$

$$A_R = 8.06 \text{ cm}^2$$

$$\Delta\lambda = 200 \text{ nm} = 0.2 \text{ μm}$$

Applied to (4.1) one obtains

$$N_{bg} = 1.0 \times 10^4 \text{ μW sr}^{-1} \text{ cm}^{-2} \text{μm}^{-1} \qquad (4.2)$$

The measured value of background radiance is considerably lower than 2.0×10^4 μW sr^{-1} cm^{-2} μm^{-1} obtained from reference [8] and used in Section 2.3, because the latter value corresponds to a zenith angle of 60°, while the radiometer was adjusted to a zenith angle of 90°, i.e. the horizontal. Since the higher value of background radiance was used in Section 2.3 to prove that the photodiode does not saturate, the same conclusion applies to the lower measured value.

b) Conversion of AC Signal to Time-Varying Component of Background Radiance

Applying the same approach to the peak-to-peak variation of 0.040 V, and bearing in mind that it is amplified by a factor of 100, the amplitude of the time-varying component of radiance was calculated to

be equal to 6.2 $\mu W\ sr^{-1}\ cm^{-2}\ \mu m^{-1}$. Furthermore, a comparison between laser pulse envelopes (such as Figure 4.4b) and the time-varying component of background radiance (Figures 4.18a and 4.18b) reveals that the frequency range in both cases is similar. When the radiometer was raised by 2^{o} with respect to the horizontal, the DC signal decreased to 0.56 V (see Figures 4.19a and 4.19b). This is due to the fact that the radiometer was measuring the sky radiance rather than the sum of ground and sky radiances. At the same time the peak-to-peak value of the AC signal decreased to 12 mV. A further adjustment of the radiometer to 4^{o} above horizon (see Figure 4.20) increased the DC signal to 0.64 V. This was expected because after the radiometer ceases to detect the ground radiance and measures the sky radiance only, the latter quantity will increase as the zenith angle decreases. The AC signal was further reduced to about 4 mV peak-to-peak because air turbulence is most pronounced in horizontal optical transmission paths close to the ground. The larger the elevation angle, the smaller will be the effect of scintillation as the optical transmission path crosses increasingly stable layers of the atmosphere.

Following these experiments the radiometer was relevelled and measurements taken as soon as a cloud obscured the sun (see Figure 4.21). The DC level was 0.64 V compared to 0.66 V measured under a sunny sky. While the AC component reduced from 40 mV (bright sun) to about 10 mV.

The results of these tests can be summarized as follows:

1) The background radiance measured when a radiometer was aimed at the horizon has a steady state and time-varying component. The frequency range of the latter is the same as the one observed on the

Low frequency component
Horizontal Scale
0.5 s/cm
Vertical Scale
0.2 V/cm

High frequency component
Horizontal Scale
0.5 s/cm
Vertical Scale
0.02 V/cm

Figure 4.19a Background radiance measurement; zenith angle + 2°, full sun.

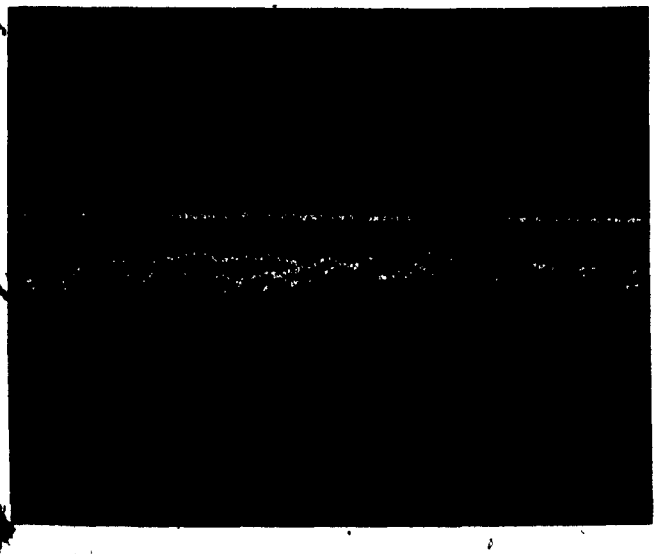

Low frequency component
Horizontal Scale
0.5 s/cm
Vertical Scale
0.2 V/cm

High frequency component
Horizontal Scale
0.5 s/cm
Vertical Scale
0.1 V/cm

Figure 4.19b Background radiance measurement; zenith angle + 2°, full sun.

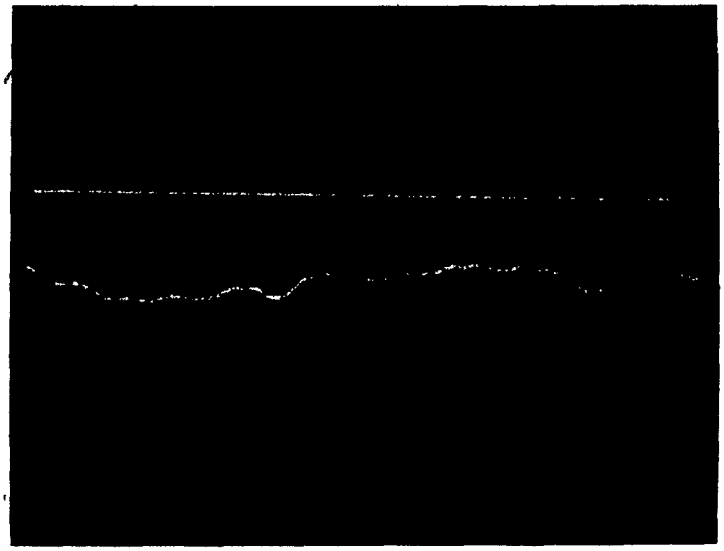

Low frequency component
Horizontal Scale
0.5 s/cm
Vertical Scale
0.2 V/cm

High frequency component
Horizontal Scale
0.5 s/cm
Vertical Scale
0.02 V/cm

Figure 4.20 Background radiance measurement; zenith angle + 4°, full sun.

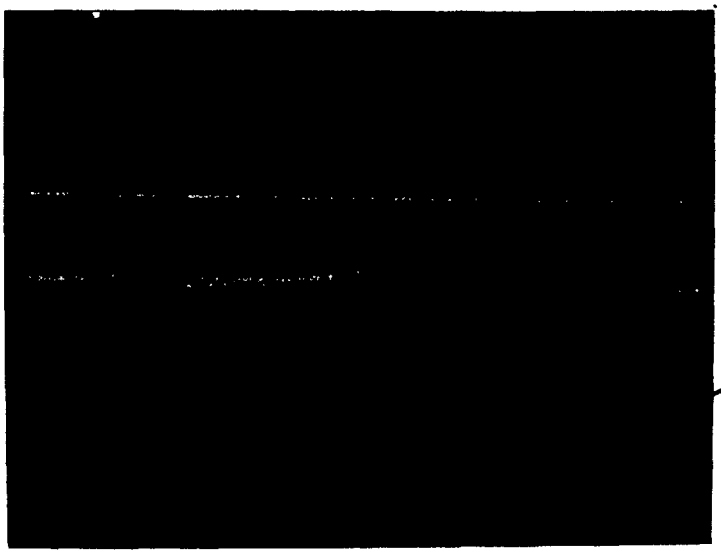

Low frequency component
Horizontal Scale
0.5 s/cm
Vertical Scale
0.2 V/cm

High frequency component
Horizontal Scale
0.5 s/cm
Vertical Scale
0.02 V/cm

Figure 4.21 Background radiance measurement; zenith angle 0°, cloudy.

laser and xenon signals.

2) The amplitude of the time-varying component decreases as the elevation angle increases because air turbulence decreases with altitude.

3) When the radiometer is level, the amplitude of the AC component decreases suddenly when the sun is obscured by a cloud quite similarly to the received amplitude of the laser and xenon signals propagating through the turbulent atmosphere.

CHAPTER V

INTERPRETATION OF TEST RESULTS

5.1 Introduction

In this chapter the experimental results presented in Chapter IV will be related to the theory summarized in Chapter II and to the system design described in Chapter III. The topics discussed include the cumulative distribution function of irradiance introduced by (2.47), the relationship between transmission error rate and modulation index and the effect of the solar radiation on the cumulative distribution function of irradiance as well as on the modulation index. Based on the results of this study the influence of solar radiation on scintillation is discussed and some further investigation of this phenomenon in the field and under laboratory conditions is proposed. From results obtained during field tests criteria for the design of opto-electronic communication links utilizing divergent coherent and incoherent infrared beams are established.

5.2 Cumulative Distribution Function of Irradiance

In Section 2.6 it was mentioned that according to Tatarski [14] the probability density function of ln H is normal. A convenient way of establishing whether or not experimental results verify this theory is to plot the cumulative distribution function of the measured values of H, i.e. P*(H), as a function of ln H on so-called probability graph paper. If the distribution is log-normal then its representation on

the probability graph paper is a straight line. This method has been used by Tatarski [14], Gracheva and Gurvich [21], Hohn [31] as well as Fried et al. [24] and was also applied to the experimental results gathered during field tests in this investigation.

Six typical photographs of oscilloscope traces were selected and P*(H) vs. ln H corresponding to low (Figures 5.1, 5.2), medium (Figures 5.3, 5.4) and high modulation indices (Figures 5.5, 5.6) of the laser and xenon channels were plotted. The data for these graphs were computed from photographs of receiver outputs displayed on an oscilloscope as discussed in Section 4.4. It is apparent from these graphs that linear plots corresponding to a log-normal distribution of irradiance have only been verified for low values of the modulation index. (Figures 5.1, 5.2). In the case of medium and high values of the modulation index (Figures 5.3, 5.4, 5.5, 5.6) the graphs cannot be approximated by a straight line and this implies that the irradiance distribution is not log-normal. Since a high value of modulation index coincides with high solar radiation one can deduce that the irradiance distribution is also affected by the sun. This assumption is substantiated by results published by Gracheva and Gurvich [21] who used an opto-electronic communication link consisting of a mercury arc lamp transmitter modulated at 5 kHz and a photo-multiplier receiver fitted with a 2 mm diameter lens. The length of their transmission path was 500 m and the average height above ground was 2 m. Since their experiment was performed in the summer, the meteorological conditions and the transmission path length were comparable to those prevailing during field trials described in this thesis. The envelope of amplitude variations recorded by Gracheva and Gurvich on a memory

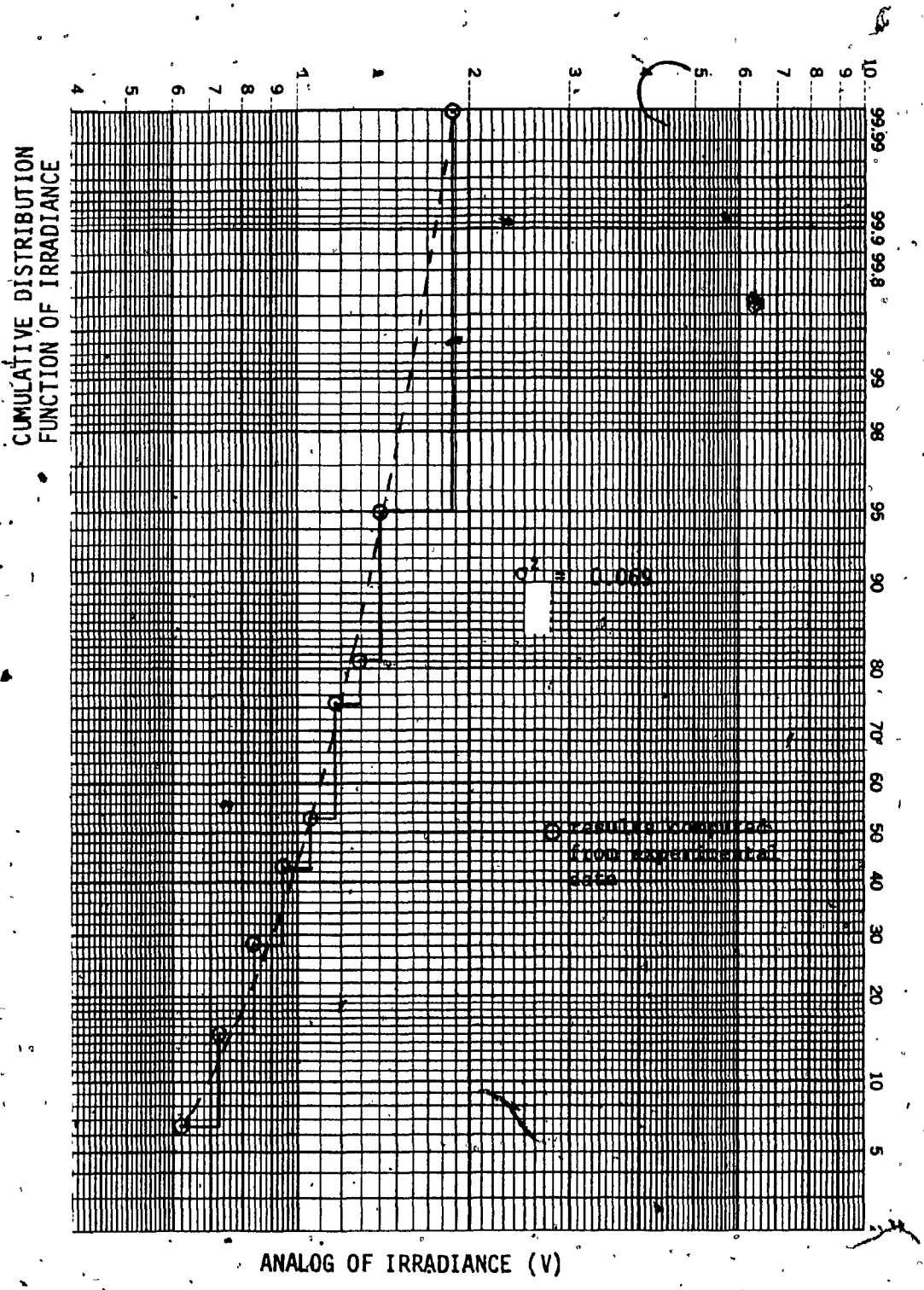

Figure 5.1 Laser channel, cumulative distribution function of irradiance vs. analog of irradiance, Photograph 2-4 (low modulation index)

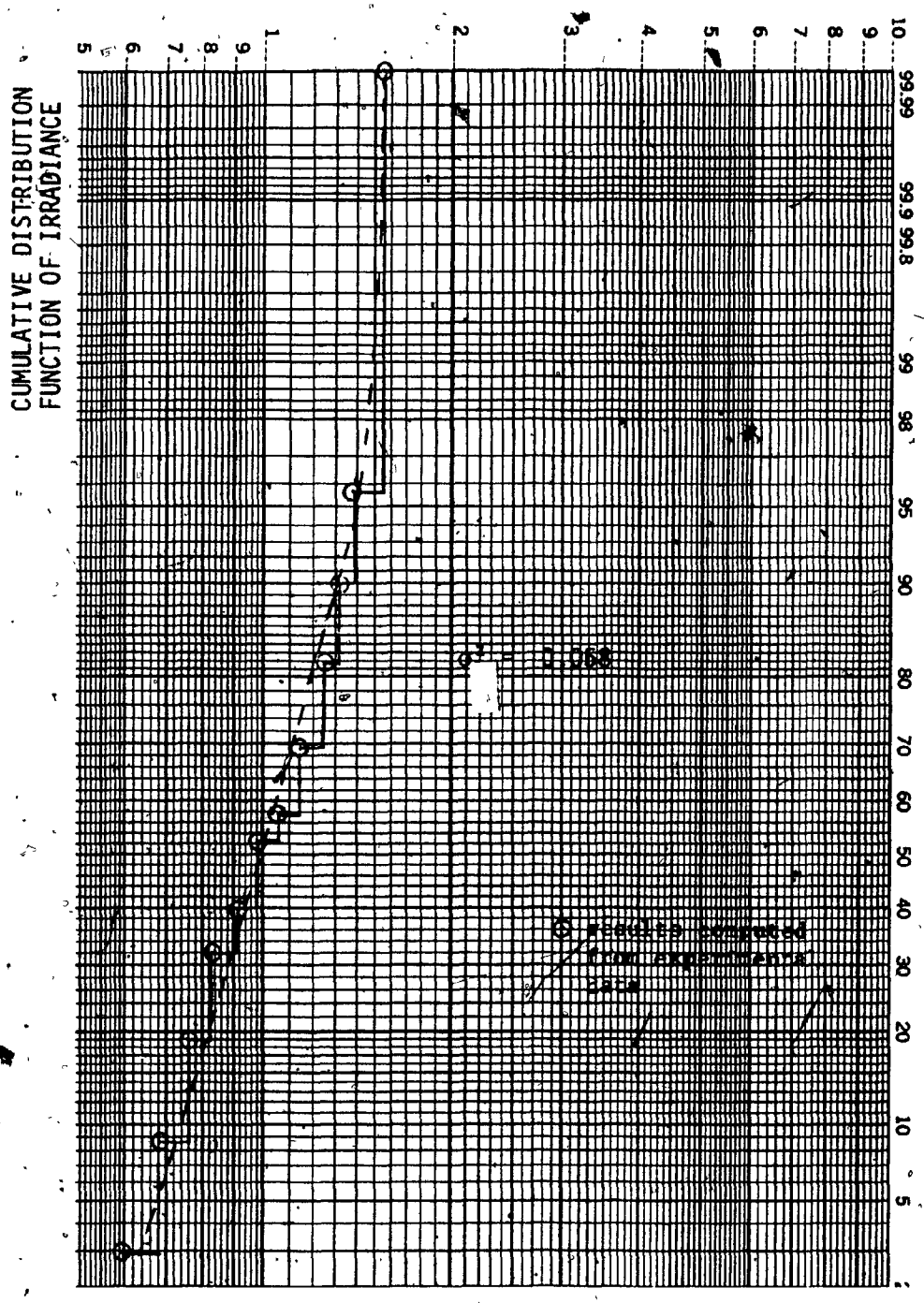

5.2 Xenon channel, cumulative distribution function of irradiance vs. analog of irradiance, photograph 23-1 (low modulation index)

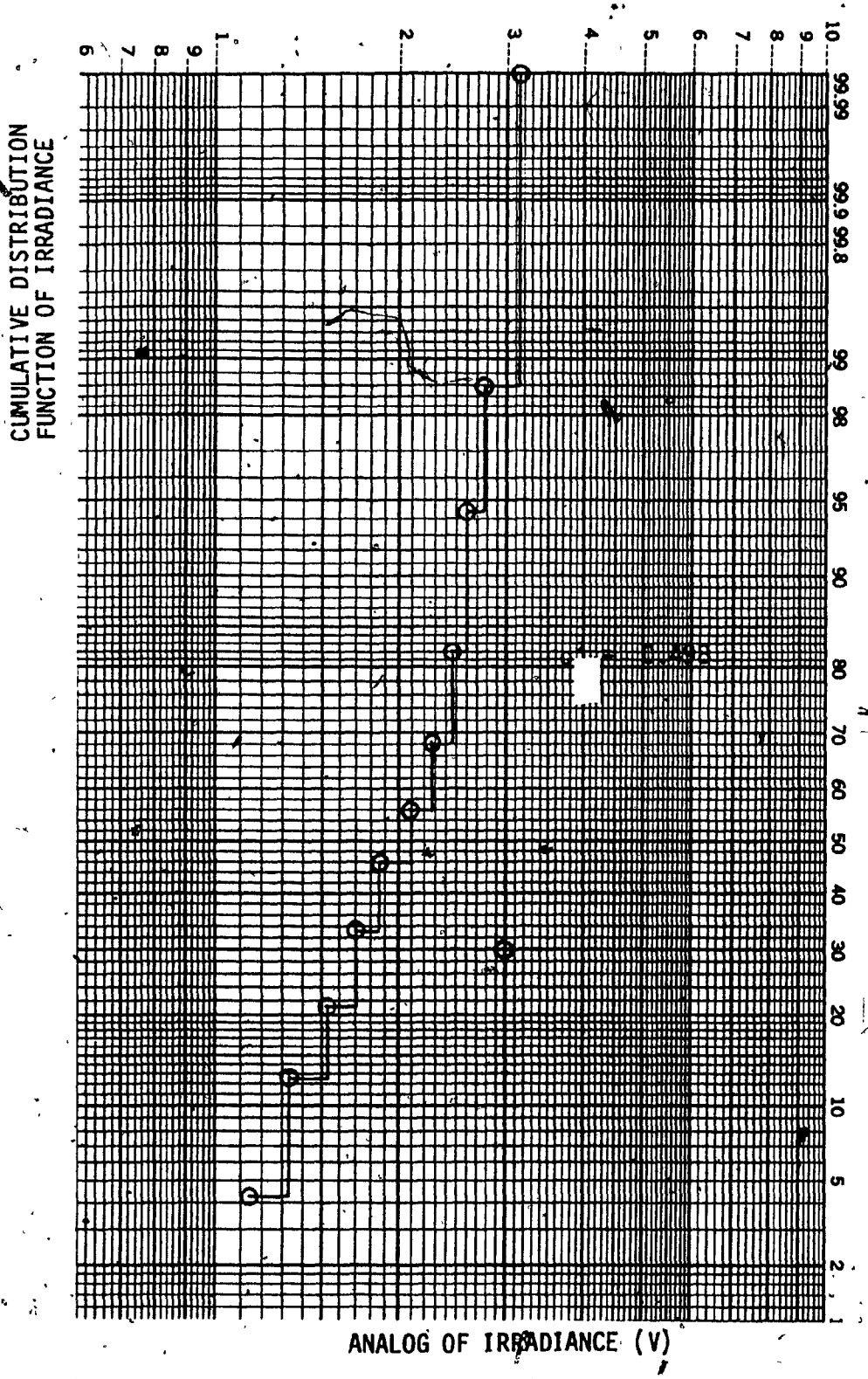

Figure 5.3 Laser channel, cumulative distribution function of irradiance vs. analog of irradiance photograph 2-7 (medium modulation index)

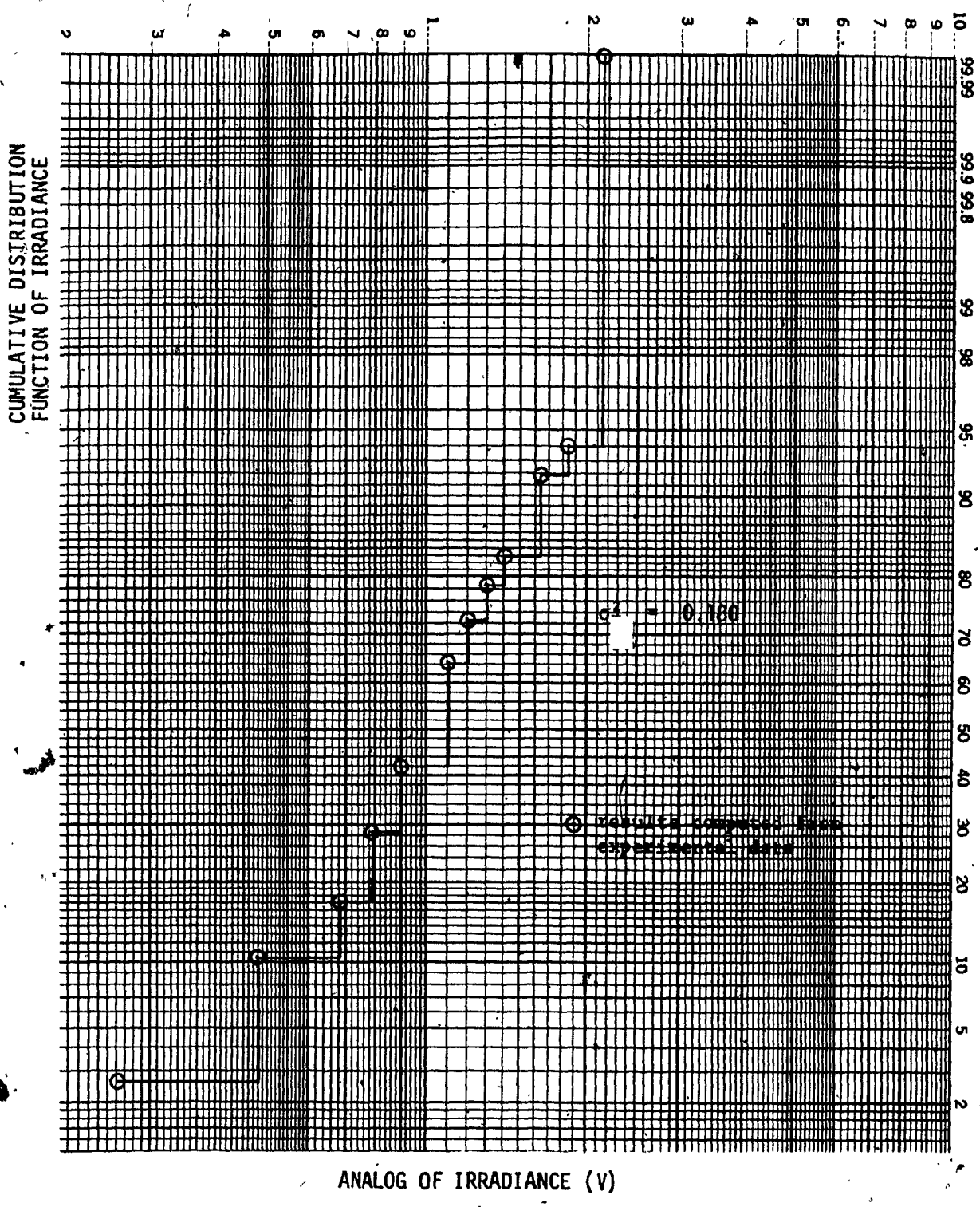

Figure 5.4 Xenon channel, cumulative distribution function or irradiance vs. analog of irradiance, photograph 18-3 (medium modulation index)

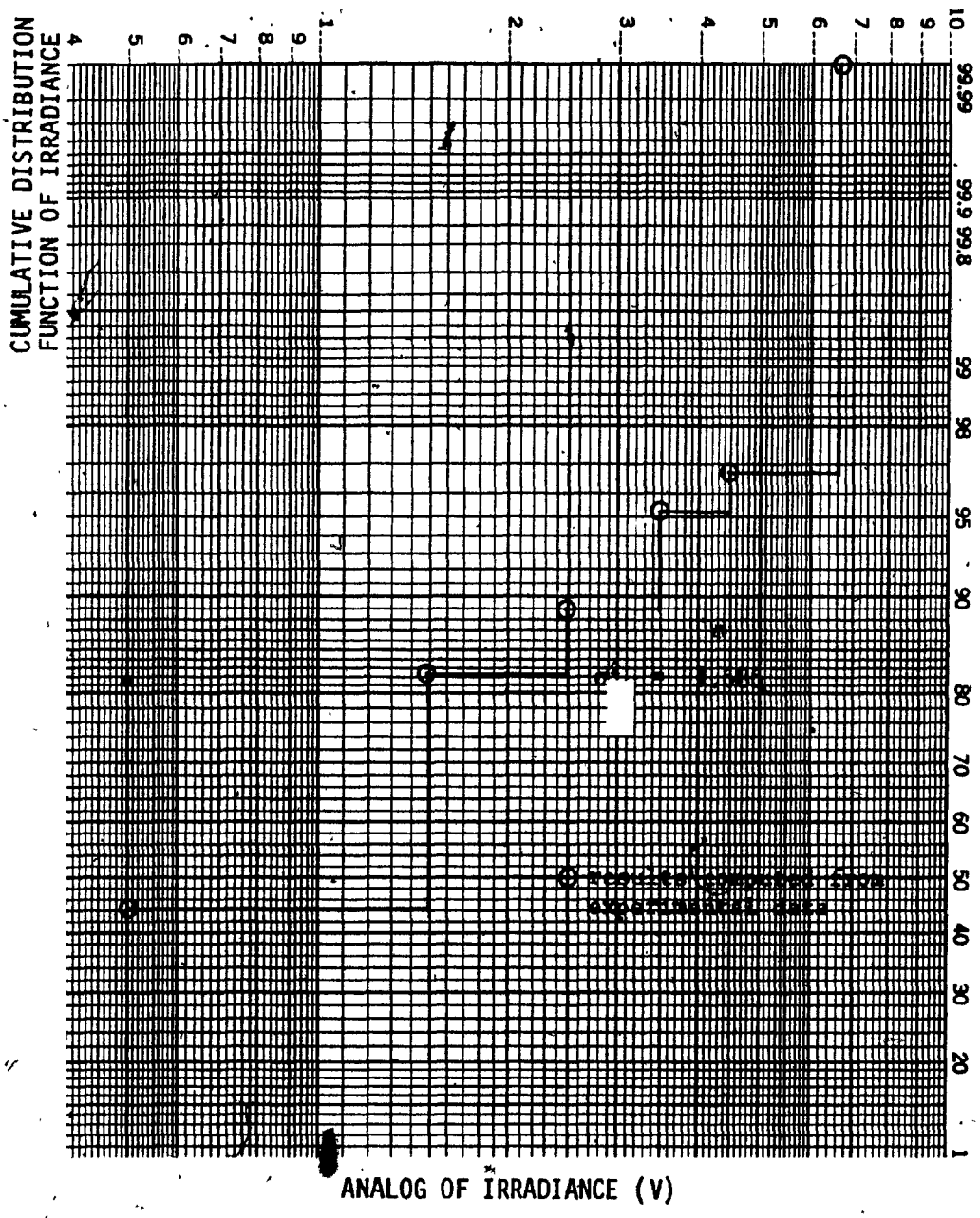

Figure 5.5 Laser channel, cumulative distribution function of irradiance vs. analog of irradiance, photograph 9-4 (high modulation index).

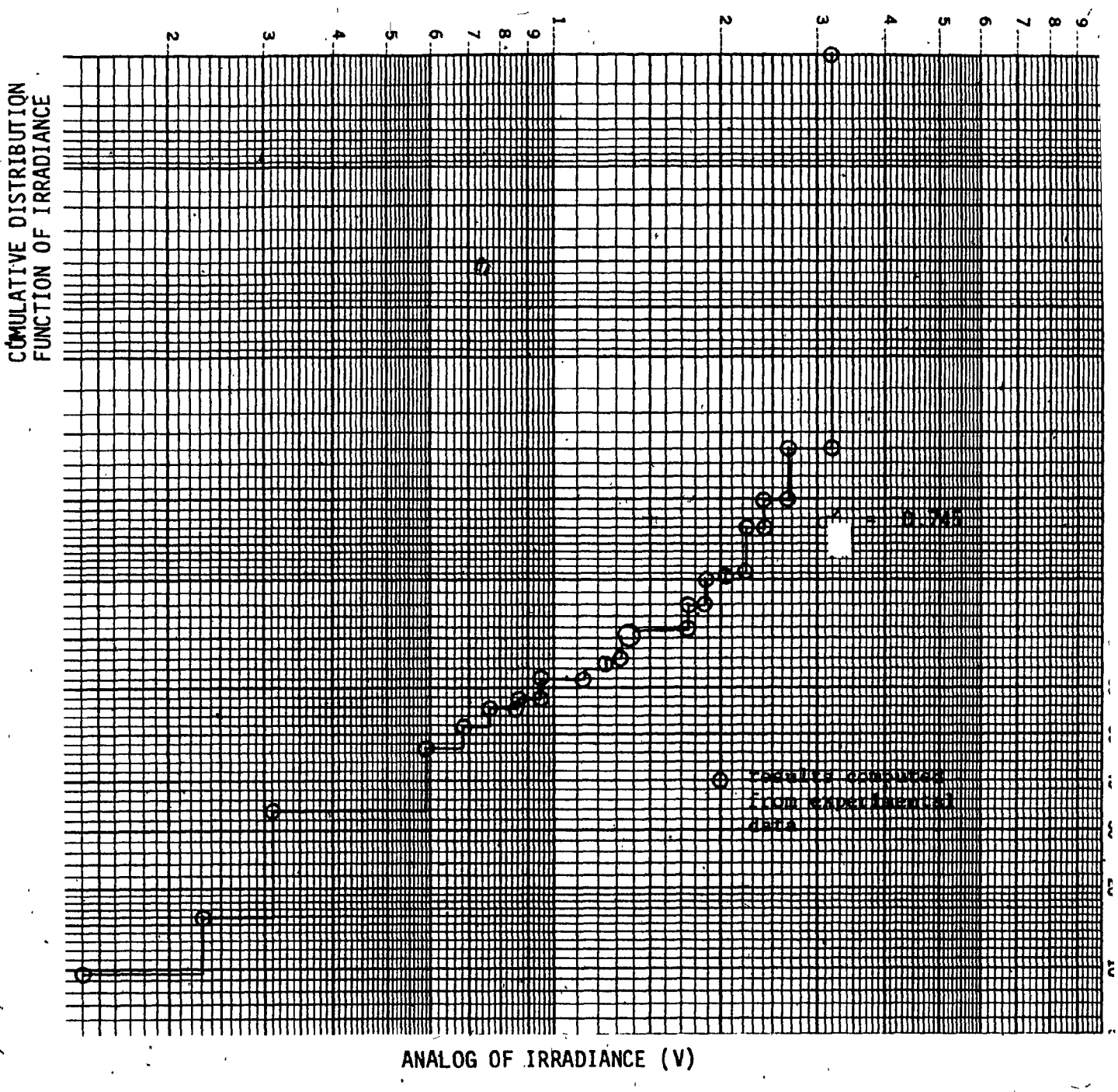

Figure 5.6 Xenon channel, cumulative distribution function of irradiance vs. analog of irradiance, photograph 12-3 (high modulation index)

oscilloscope (see Figure 5.7) is similar to the photographs of laser signal envelopes (see Figure 4.4b), bearing in mind that the time scales are different (125 ms/cm and 5 ms/cm respectively). Data from [21] were analyzed using the method described in Section 4.4 and the resulting cumulative distribution function P*(H) vs. ln H plotted in Figure 5.8 is very similar to Figures 5.5 and 5.6.

5.3 Influence of Solar Irradiance on the Modulation Index

The values of σ^2 determined by the method described in Section 4.4 are listed in Tables 4.2 and 4.3. It can be seen from these tables that σ^2 is an increasing function of sun irradiance. This is apparent from test results shown in Table 4.2 obtained using the laser channel. The modulation index determined from photographs 2-1 to 3-8 under "partial sun" conditions is lower than the modulation index determined from photographs 7-1 to 25-4 under "full sun conditions". The same observations are made with regard to tests using the xenon channel, when comparing the modulation indices evaluated from photographs 18-2 to 23-1 with those obtained from photographs 12-1 to 15-3 (see Table 4.2). These results are summarized in Table 5.1 where the average values of σ^2 measured under three types of solar irradiance conditions defined in Section 4.4 are listed. These average values are designated $\langle\sigma^2\rangle$.

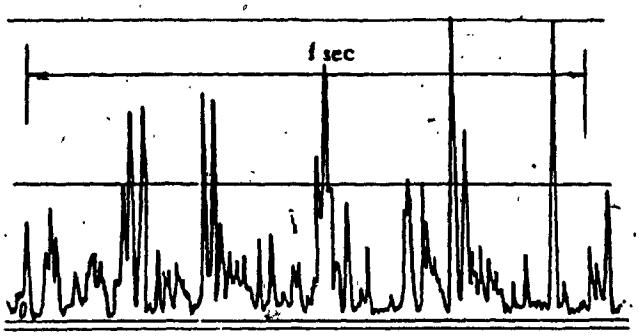

Figure 5.7 Amplitude variations recorded on memory oscilloscope [21]

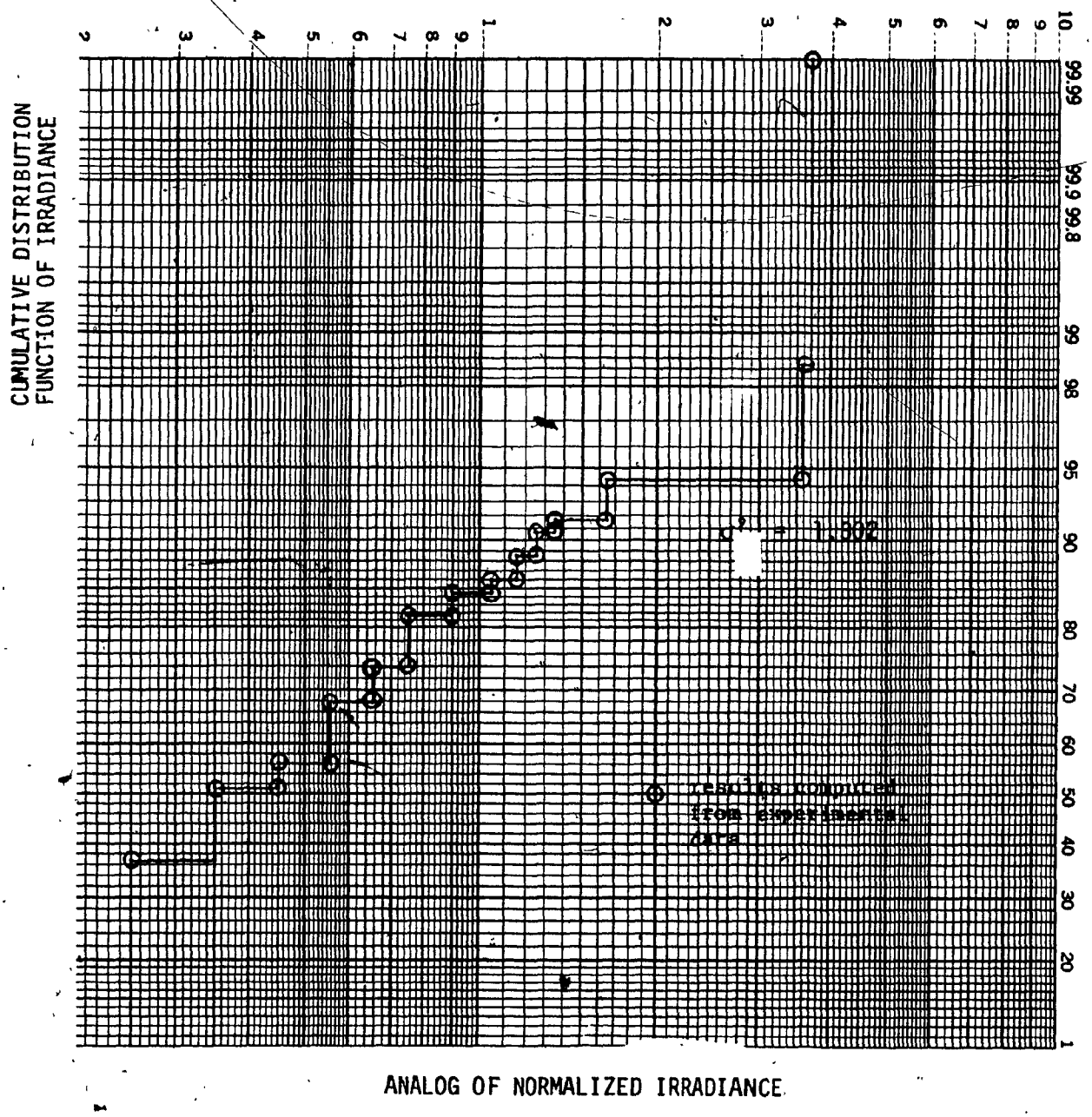

Figure 5.8 Cumulative distribution function of irradiance vs. analog of normalized irradiance [21]

TABLE 5.1

MODULATION INDEX AS A FUNCTION SOLAR IRRADIANCE

	$\langle \sigma^2 \rangle$		
	Partial Sun	Almost Full Sun	Full Sun
Laser Channel	0.170	0.321	0.519
Xenon Channel	0.129	-	0.649

Results in Table 5.1 indicate that the average value of σ^2 increases by a factor of 3 on the laser channel and a factor of 5 on the xenon channel after a transition from a "partial sun" to a "full sun" condition. It is emphasized that these variations of σ^2 take place within seconds and therefore cannot be caused by temperature variations.

It was mentioned in Section 4.4 that a transmission error, i.e. failure to detect a transmitted pulse, occurs whenever a laser or xenon pulse measured at the receiver output is less than 250 mV. The probability of this event, defined as the error rate, can be determined from the cumulative distribution function which was evaluated for each recording of the signal amplitude envelope (see Figure 4.15). With the error rate and σ^2 listed in Tables 4.2 and 4.3, the former quantity as a function of the latter can be plotted and the graphical results are shown in Figures 5.9 and 5.10. On the laser as well as on the xenon

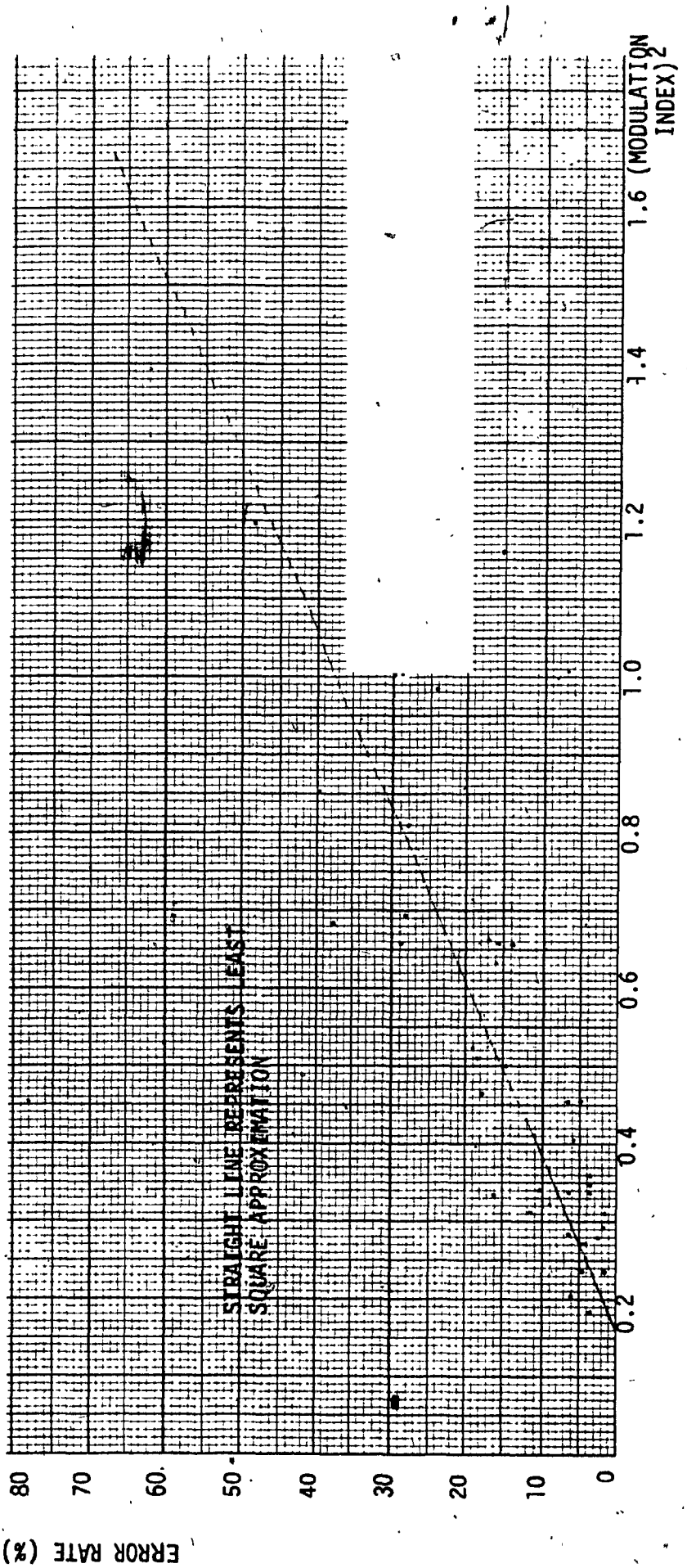

Figure 5.9 Laser channel, error rate as a function of (modulation index)^2

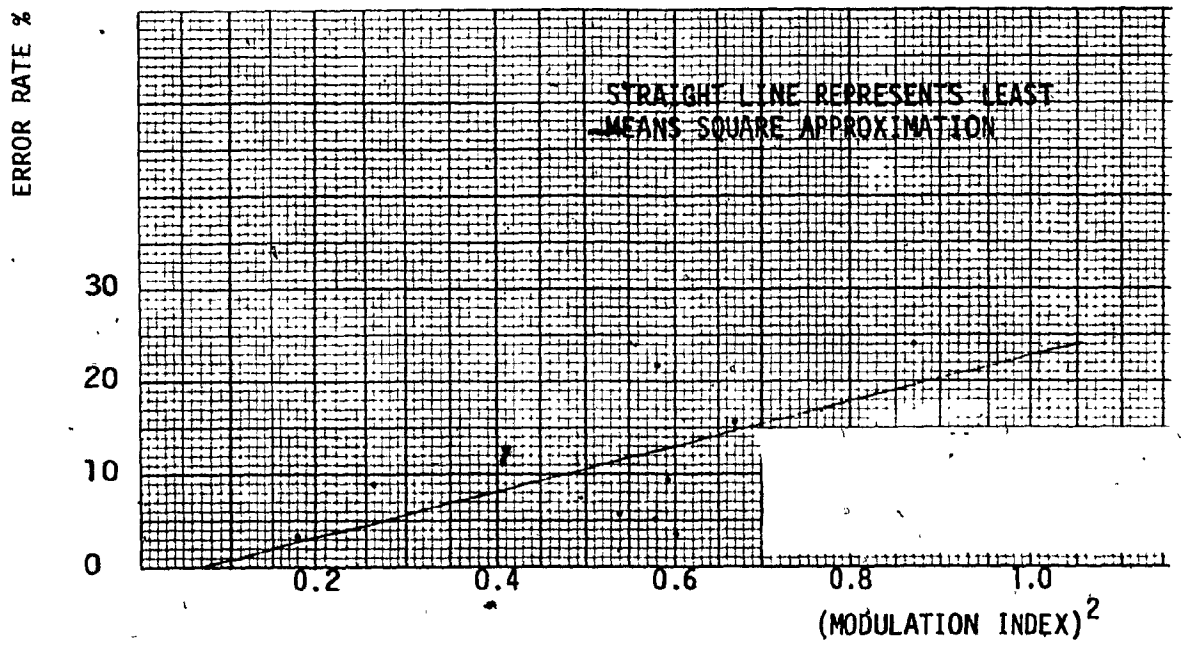

Figure 5.10 Xenon channel, error rate as a function of (modulation index)^2

communication channel the error rate is an increasing function of σ^2. On the average the error rate is higher on the laser channel than on the xenon channel. It appears that the coherent radiation generated by the laser is more prone to changes of the atmospheric refractive index than the incoherent xenon arc radiation. Two reasons can be given for this behaviour:

i) In the case of coherent radiation generated by the laser the interaction between the two portions of the beam illustrated in Figure 2.18b may be such that the irradiances are out of phase and the sum of the amplitudes at the receiver aperture is close to zero.

ii) The effect of the toroidal lens with vertical flutes illustrated in Figure 3.12 is to diffuse the xenon arc radiation. Each vertical flute within the lens creates a line image of the xenon arc so that the irradiance at the receiver aperture is approximately equal to the sum of irradiances generated by four to five images of the xenon arc. Since the radiation is incoherent, no interference can occur and the superposition of radiant input signals may smooth out the effect of turbulence.

In order to verify this hypothesis an experiment would have to be performed in which a laser and a xenon arc beam are simultaneously transmitted through the same portion of the atmosphere while the output signals from two separate receivers are photographically recorded. A comparison of modulation indices would then either confirm or contradict the above hypothesis.

5.4 Proposed Methods for Further Investigations of the Influence of Solar Irradiance on Scintillation

Although experimental results described in Chapter IV show that scintillation depends not only on ambient temperature but also on solar irradiance, additional tests in the field and in the laboratory are required to study this phenomenon under controlled conditions. Figure 5.11 illustrates the equipment which will be used in future field tests.

The transmitter and receiver are aligned and set up approximately 500 m apart. A radiometer and thin-wire thermometer are installed at the receiver location and halfway between the transmitter and the receiver. Their outputs are recorded at the same time as the receiver output which is amplitude-modulated by atmosphere turbulence and solar irradiance. The recorded data are analyzed with a digital computer and the correlation between scintillation, atmospheric temperature and solar radiance is studied quantitatively.

The investigation of scintillation under laboratory conditions should follow the method described by Carnevale et al. [32] and illustrated in Figure 5.12. A turbulent region is produced inside a tube approximately 30 cm in diameter using a grid of heated nichrome wires and a blower. The laser beam is transmitted through this medium and the irradiance variations can be observed with an oscilloscope. In order to simulate the effect of sun irradiance it is proposed to irradiate the laser path through the turbulent region by a collimated beam generated by an arc lamp. The beam would be alternately switched on or off to simulate the effect of variable cloud cover. The same procedure would then be applied to the xenon radiation.

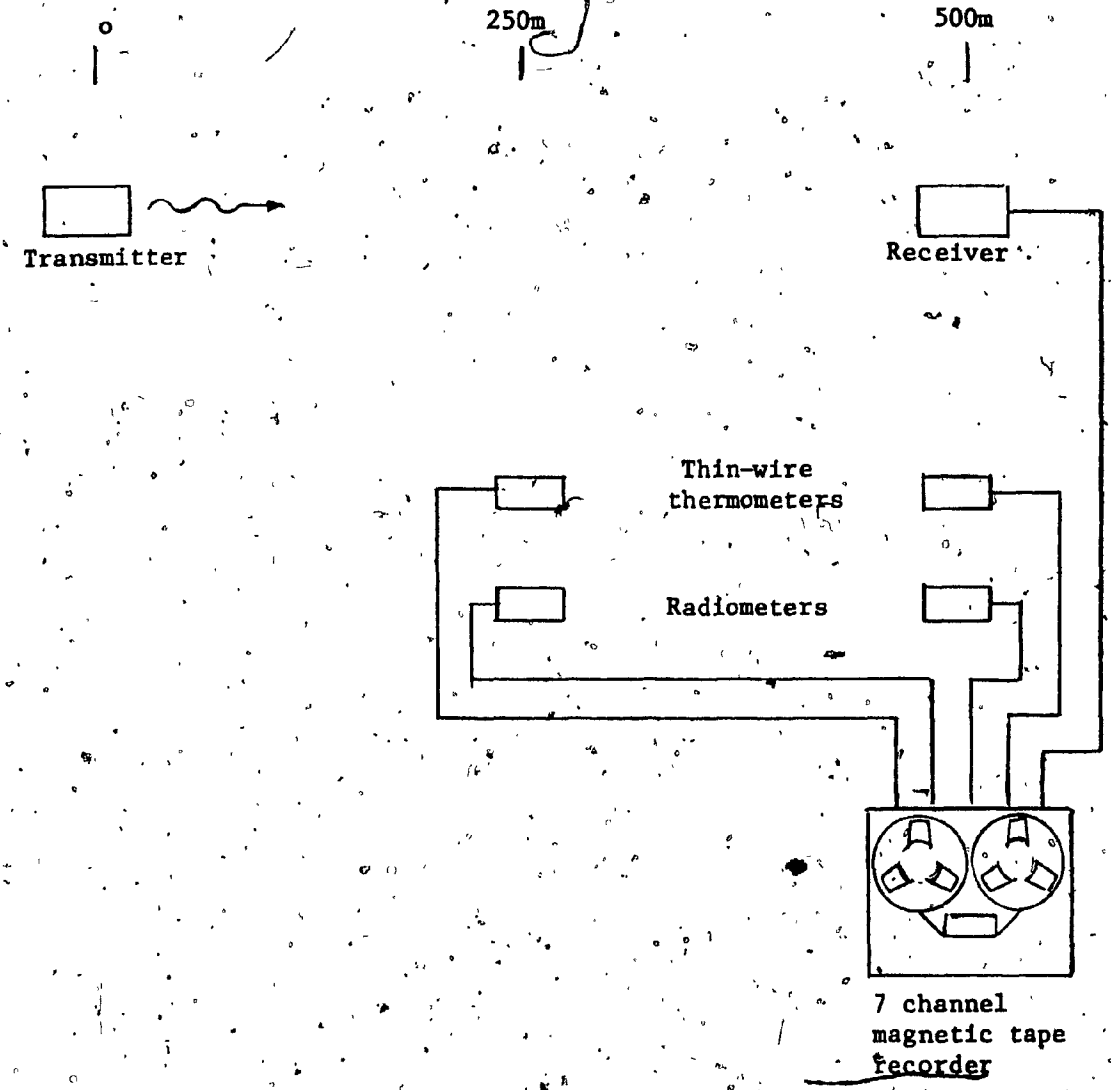

Figure 5.11 Optical link and equipment for the study of scintillation due to air turbulence and solar radiation.

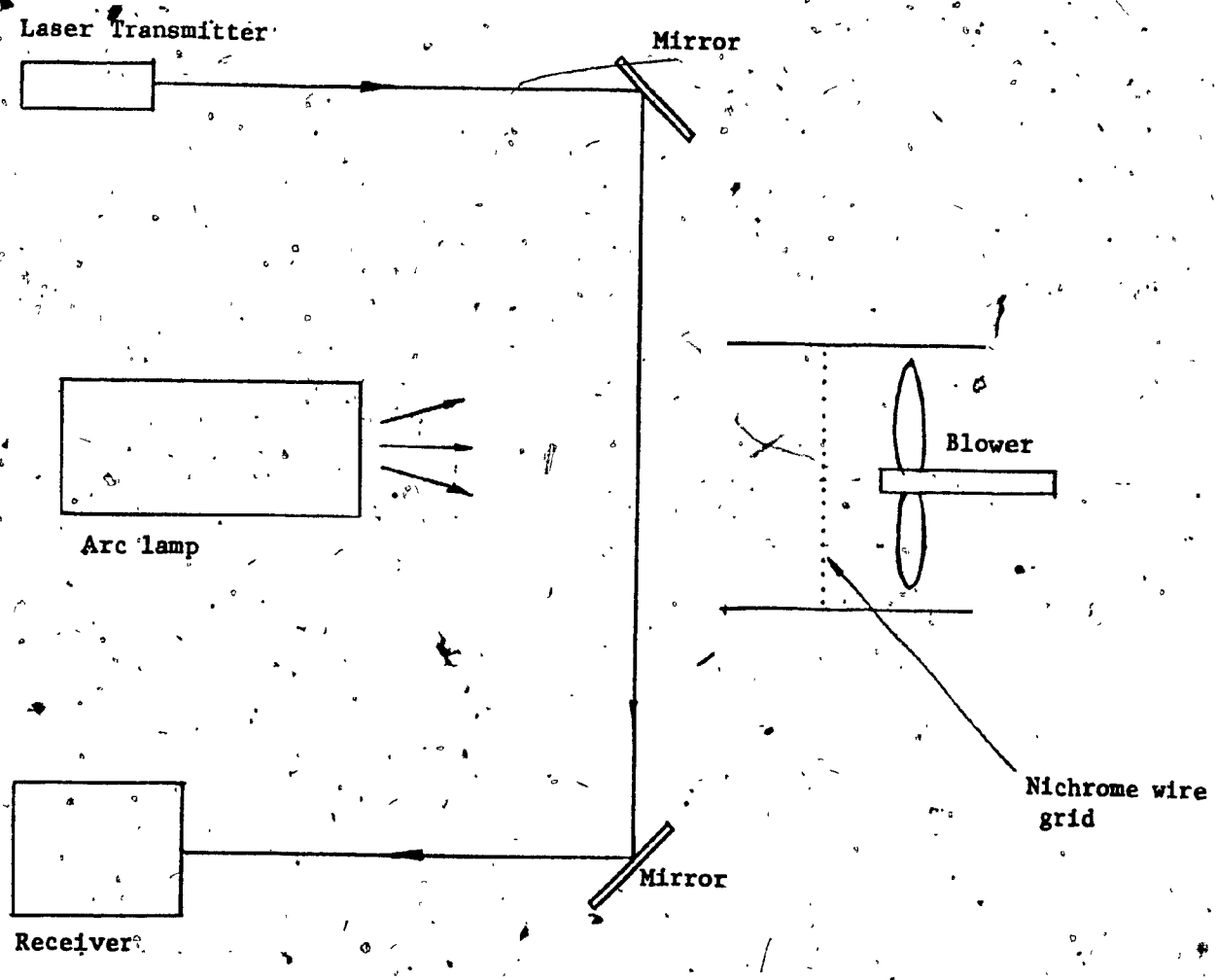

Figure 5.12 Diagram of apparatus for studying in the laboratory infrared transmission through turbulent air irradiated by an arc lamp

5.5 Guidelines for the Design of Communication Links Consisting of Divergent Coherent and Incoherent Infrared Beams

The field trials described in Section 4.2 show that the high transmission error rate caused by air turbulence in the presence of sun irradiance renders information transmission by divergent laser or xenon beams over a distance of 500 m unreliable. However, the reliability of information transmission can be considerably improved for distances shorter than 500 m. According to (2.81) the variance of the logarithm of irradiance σ_T is an increasing function of distance x. It was shown in Section 5.3 that the transmission error rate is an increasing function of σ_T. Therefore, the transmission error rate can be decreased by reducing the transmission distance x. From Tables 4.1 and 4.2 it is apparent that the error rate of laser and xenon transmission is negligible, i.e. the transmission is reliable, for $\sigma_T^2 \leq 0.1$. According to the tables the maximum measured value of σ_T^2 is 1.69 and (2.81) can be used to determine the corresponding value of C_n^2. By adopting $\sigma_T^2 = 2.0$ a more stringent system design criterion is set and for $k = 2\pi/\lambda = 6.95 \times 10^6\ m^{-1}$, $x = 500$ m, (2.81) yields $C_n^2 = 1.91 \times 10^{-12}\ m^{-2/3}$. Substituting the above values into (2.81) and assuming that $\sigma_T^2 = 0.09$ will insure reliable transmission the maximum distance for error free transmission is 109 m.

Reliability can also be improved to some extent by raising the radiant power output of the transmitter thereby increasing the probability of above-threshold detection. However, this approach has practical limitations inasmuch as the radiant power output of the laser diode can increase by 7 dB at most and that of the xenon flash tube no

more than 5 dB. In contrast, air turbulence may diminish the receiver output level by as much as 150 dB.

Substantial improvement in transmission reliability is achieved by increasing the area of the receiver lens. This design approach tends to integrate irradiance and angle of incidence fluctuations and is known in the literature as aperture smoothing. Its effect is to decrease the modulation index as a consequence (see Figures 5.9 and 5.10) reduce the error rate. Edwards and Steen [33] studied the relationship between the modulation index σ of the receiver signal and the diameter D of the aperture and derived the empirical formula

$$\sigma^2 = \frac{\text{constant}}{D^{\alpha}} \qquad (5.2)$$

where $\alpha \simeq 1$. A graph of this function reproduced from [33] appears in Figure 5.13. An examination of this graph leads to the conclusion that the previously mentioned criteria for reliable transmission, namely $\sigma^2 < 0.1$ is achieved if the lens diameter is larger than 8 cm. However, it must be emphasized that this result may not be directly applicable to the laser and xenon communication links examined in this thesis because in the experiment described by Edwards and Steen [33] a zirconium arc lamp transmitter of unspecified divergence was used. Since the length of a zirconium arc is approximately 2.5 mm, and knowing that it was located at the focus of a lens with a focal distance of 150 mm, the divergence of the beam is estimated to be 15 mrad. On the other hand the vertical divergence of the laser and xenon beams is 300 mrad and therefore the decrease in modulation index brought about by an increase in receiver aperture is expected to be lower than that

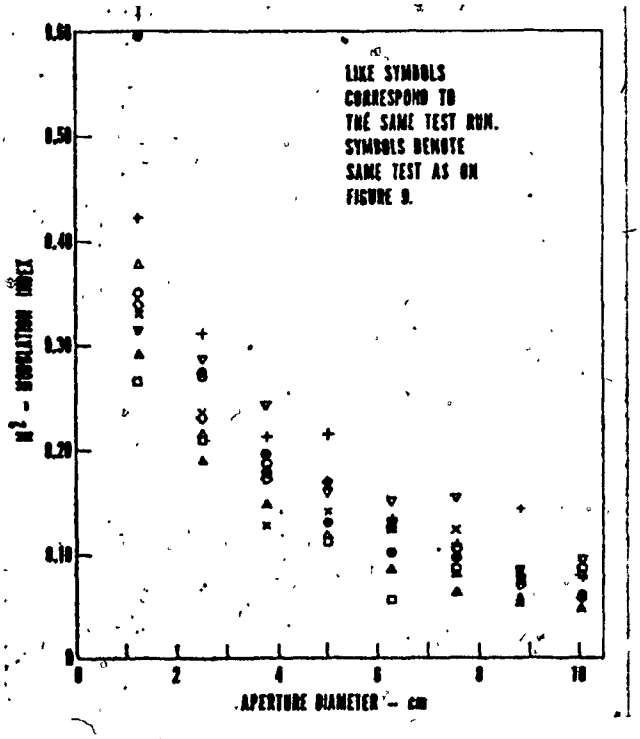

Figure 5.13 (Modulation index)^2 vs. receiver aperture [33]

achieved by Edwards and Steen [33]. Additional experimental work correlating modulation index to receiver lens diameter in the laser and xenon communication links is required.

For highest reliability in information transmission well collimated beams must be used and the receiver aperture must be larger than the cross-sectional area of the beam. When this optical configuration is adopted all the fluctuations of irradiance caused by air turbulence are integrated by the receiver and the anticipated amplitude variations will be of the order of only ± 1 dB. However, it should be borne in mind that such an opto-electronic communication link requires an accurate transmitter-receiver alignment in the horizontal as well as the vertical plane, a requirement which goes counter the design objective of easy system alignment as spelled out in the introduction.

CHAPTER VI

CONCLUSION

The conclusions of this study on the transmission characteristics of infrared beams using either a gallium-arsenide laser transmitter or a xenon arc transmitter can be summarized as follows:

a) The energy density within an infrared beam propagating through the atmosphere is affected by random air refractive index variations which cause random amplitude variations or scintillation in the receiver output signal. The statistics of this phenomena is described by the modulation index.

b) In the past variations of the air refractive index induced by temperature gradients have been assumed to be the only cause of scintillation. Experiments described in this study indicate that under conditions of variable cloudiness scintillation increases with an increasing exposure of the transmission path to direct sun light. Modulation index increases by a factor of 3 on the average were recorded within two seconds when open sun light replaced cloudy skies. Since the rise of ambient temperature caused by convective heat transfer from an irradiated soil to turbulent air is a relatively slow process, the time constant associated with this phenomenon is much longer than two seconds. On the other hand the radiative heat transfer to the atmosphere is negligible and it is therefore concluded that the sudden

increase in the modulation index is caused by solar irradiance.

c) Amplitude variations observed in the receiver output signal suggest that the background radiance i.e. the solar radiation scattered by air molecules and aerosol particles and reflected by the ground, should have a high-frequency component superimposed on a slowly varying component. This hypothesis has been verified by means of radiometer measurements.

d) The increase in scintillation caused by solar irradiance suggests a polarization of air molecules which attenuates the infrared signal transmitted through the atmosphere. Additional laboratory and field experiements required to investigate this hypothesis have been described.

e) The error rate of data transmission has been found to be an increasing function of modulation index. Since the modulation index is also an increasing function of distance, error-free data transmission by means of divergent coherent and incoherent infrared beams can only be achieved over relatively short distances. The latter were calculated to be approximately 100 m. Higher transmission reliability over greater distances requires a collimated beam and a receiver aperture which is larger than the cross-sectional area of the beam.

APPENDIX

ANALYSIS OF PHOTODIODE OUTPUT VOLTAGE AS A FUNCTION OF LOAD RESISTANCE

The equivalent circuit of the biased photodiode is shown in Figure 3.14b. Assuming that the radiant power input is a square pulse of duration τ, which in turn generates a square current pulse of the same duration, the output voltage is given by

$$e_o(t) = Zi(t) \tag{A.1}$$

where:

$$Z^{-1} = R^{-1} + j\omega C_d$$

$$i(t) = I_m[u(t)-u(t-\tau)]$$

I_m is the current pulse amplitude, $u(t)$ is the unit step function and $u(t-\tau)$ is the unit step function delayed by τ. The Laplace transform of (A.1) is

$$E_o(s) = RI_m/(1+RC_d s) \cdot [1/s-\exp(-\tau s)/s]$$

$$= RI_m[1/s(1+RC_d s)-\exp(-\tau s)/s(1+RC_d s)] \tag{A.2}$$

Inverse Laplace transformation of (A.2) yields

$$e_o(t) = RI_m\{u(t)[1-\exp(-t/RC_d)] - u(t-\tau)[1-\exp(-(t-\tau)/RC_d)]\} \tag{A.3}$$

a) Laser photodiode circuit

In this case $\tau = \tau_L = 40$ ns and $I_m = 1.17$ mA. The value of I_m was determined from

$$I_m = 0.1\, H_L A_L \beta_r \tag{A.4}$$

where $H_L = 349\ W/m^2$ is the irradiance at a distance of 5.20 m

calculated from (3.4), $A_L = 5.61 \times 10^{-5}$ m^2 is the cross-sectional area of the laser beam intercepted by the 3.0 cm diameter receiver lens, $\beta_r = 0.60$ A/W is the responsivity of the photodiode and the factor 0.1 takes into account the 10% transmittance of the neutral density filter which was used during the photodiode output voltage as a function of load resistance measurements. The theoretical variation of the laser photodiode output voltage as a function of load resistance was determined by plotting (A.3) after substituting $I_m = 1.17$ mA and $\tau \approx \tau_L = 40$ ns into this equation. The theoretical results are shown by a dotted line while the experimental results are shown by a solid line in Figure 3.15.

b) Xenon photodiode circuit

In this case $\tau = \tau_X = 1.7$ μs and $I_m = 2.04 \times 10^{-4}$ A. The value of I_m was determined from

$$I_m = 0.1 H_X A_R \beta_r \qquad (A.5)$$

where $H_X = 4.80 \times 10^{-1}$ W/m^2 is the irradiance measured at 2.54 m (see paragraph 3.4), $A_R = 7.07 \times 10^{-4}$ m^2 is the area of the receiver lens, $\beta_r = 0.60$ A/W is the responsivity of the photodiode and the factor 0.1 is the transmittance of the neutral density filter mentioned above. The theoretical variation of the laser photodiode output voltage as a function of load resistance was determined by plotting (A.3) after substituting $I_m = 2.04 \times 10^{-4}$ A and $\tau = \tau_X = 1.7$ μs into this equation. The theoretical results are shown by a dotted line while the experimental results are shown by a solid line in Figure 3.16.

LIST OF REFERENCES

[1] A. E. Siegman: "An Introduction to Lasers and Masers", McGraw-Hill Book Company, New York, 1971.

[2] V. Ye. Zuyev: "Propagation of Visible and Infrared Waves in the Atmosphere", Sovetskoye Radio Press, Moscow, NASA Technical Translation TT F-707, July 1972.

[3] E. Hecht and Z. Zajac: "Optics", Addison-Wesley, Reading, 1975.

[4] Lord Rayleigh: "The Light Scattered by Gases, its Polarisation and Intensity", Proc. Roy. Soc., v.95, pp. 155-176, 1919.

[5] R. Penndorf: "Tables of Refractive Index of Standard Air and the Rayleigh Scattering Coefficient for the Spectral Region between 0.2 and 20.0μ and their Application to Atmospheric Optics", J. Opt. Soc. Amer., v.47, pp. 176-182, February 1975.

[6] G. Mie: "Beiträge zur Optik trüber Medien, speziell kolloidaller Metallösungen, Ann. Phys., v. 25, pp. 375-379, 1908.

[7] R. Penndorf: "New Tables of Total Mie Scattering Coefficients for Spherical Particles of Real Refractive Indexes ($1.33<n<1.50$)", J. Opt. Soc. Amer., v. 47, pp. 1010-1015, November 1957.

[8] "Handbook of Military Infrared Technology", Office of Naval Research Washington, 1965.

[9] "The U.S. Standard Atmosphere", U.S. Government Printing Office, Washington, 1962.

[10] G. R. Ochs and R. S. Lawrence: "Measurements of Laser Beam Spread and Curvature Over Near-Horizontal Atmospheric Paths", U. S. Government Printing Office, Washington, D.C., ESSA Tech. Rept. ERL 106 - WPL 6, 1969.

[11] M. Schwartz: "Information Transmission, Modulation and Noise", McGraw-Hill Book Company, New York, 1959.

[12] B. P. Lathi: "An Introduction to Random Signals and Communication Theory", International Textbook Co., Scranton, 1968.

[13] A. N. Kolmogorov: "Dissipation of Energy in Locally Isotropic Turbulence", Doklady Akad. Nauk SSSR, v.32, pp. 16-18, 1941.

[14] V. I. Tatarski: "Wave Propagation in a Turbulent Medium", Dover Publications Inc., New York. 1961.

[15] D. A. Gray and A. T. Waterman, Jr.: "Measurement of Fine-Scale Atmosphere Structure Using an Optical Propagation Technique", J. Geophys. Res., v.75, pp. 1077-1083, 1970.

[16] R. S. Lawrence and J. W. Strohbehn: "A Survey of Clear-Air Propagation Effects Relevant to the Optical Communications", Proc. IEEE, v.58, pp. 1523-1545, October 1970.

[17] A. M. Obukhov: "On the Energy Distribution in the Spectrum of Turbulent Flow", Doklady Akad. Nauk SSSR, v.39, pp. 19-21, 1941.

[18] T. Chiba and Y. Sugiura: "Spot Dancing of Laser Beam in Atmospheric Propagation", Electronics and Communications in Japan, v.54-B, pp. 89-96, 1971.

[19] R. Gruss: "Die Ubertragung von Laserstrahlung durch die Atmosphäre", Nachrichtentechnische Zeitschrift, v.3, pp. 184-192, March 1969.

[20] M. Subramanian and J. A. Collinson: "Modulation of Laser Beams By Atmospheric Turbulence - Depth of Modulation", B.S.T.J., v.46, pp. 623-647 March 1967.

[21] M. E. Gracheva and A. S. Gurvich: "Strong Fluctuations in the Intensity of Light Propagated through the Atmosphere close to the Earth", Izv. Vyssh Ucheb. Zaved Radiofiz, v. 8, no. 4, pp. 717-724, 1965.

[22] G. R. Ochs: "Measurements of 0.63μ Laser Beam Scintillation in Strong Atmospheric Turbulence", U. S. Government Printing Office, Washington, D. C. ESSA Technical Report ERL 154 - WPL 10, 1970.

[23] R. J. Kerr: "Experiments on Turbulence Characteristics and Multi-Wave-Length Scintillation Phenomena", J. Opt. Soc. Amer., v. 62, pp. 1040-1049, Sept. 1967.

[24] D. L. Fried, G. E. Mevers, and M.P. Keister: "Measurement of Laser Beam Scintillation in the Atmosphere", J. Opt. Soc. Amer. v.57, pp. 787-797, June 1967.

[25] B. R. Bean: "Meteorological Factors Affecting the Fine-Scale Structure of the Radio and Optical Refractive Index", IEEE Conference on Tropospheric Wave Propagation, London, Sept. 30-Oct. 2, 1968, Conf. Publ. 48.

[26] P. H.Deitz and N. J. Wright: "Saturation of Scintillation Magnitude in Near-Earth Optical Propagation", pp. 527-537., J. Opt. Soc. Amer., v.59, May 1969.

[27] M. Chomat and F. Hoff: "Statistical Distribution of the Envelope of an Amplitude Modulated Laser Signal after Passage through the Atmosphere", El. Lett., v.2, pp. 409-410, November 1966.

[28] G. R. Ochs and C. E. Little: "Studies of Atmospheric Propagation of Laser Beams on 5.5, 15, 45 and 145 km Paths", IEEE Conference on Tropospheric Wave Propagation, pp. 199-206, London, Sept. 30-Oct. 2, 1968.

[29] "Electro-Optics Handbook", RCA Commercial Engineering, Harrison, 1968.

[30] H. Hodara: "Laser Wave Propagation through the Atmosphere", Proc. IEEE, v. 54, pp. 368 - 375, March 1966.

[31] D. H. Hohn: "Effects of Atmospheric Turbulence on the Transmission of a Laser Beam at 6 328 Å - I. Distribution of Intensity", Appl. Opt. v.5, pp. 1427-1431, Sept. 1967.

[32] M. Carnevale, B. Crosigniani and P. di Porto: "Influence of Laboratory Generated Turbulence on Phase Fluctuations of a Laser Beam", Appl. Opt. v.7, pp. 1121-1123, June 1968.

[33] B. N. Edwards and R. R. Steen: "Effects of Atmospheric Turbulence on the Transmission of Visible and Near Infrared Radiation", Appl. Opt., v.4, pp. 311-316, March 1965.

[34] A. S. Gurvich, V.I. Tatarski and L.P. Tsvang: "Experimental Investigation of the Statistical Character of the Twinkle of Light Originating at the Earth's Surface," Doklady Akad. Nauk SSSR, V. 123, pp. 656-660, 1958.